THREE-DIMENSIONAL CHARACTERIZATION OF MORPHOLOGY AND CRYSTALLOGRAPHY OF LATH MARTENSITE IN MARTENSITIC STAINLESS STEELS

THREE-DIMENSIONAL CHARACTERIZATION OF MORPHOLOGY AND CRYSTALLOGRAPHY OF LATH MARTENSITE IN MARTENSITIC STAINLESS STEELS

BY

MEHDI MOSAYEBI, B.Sc., M.Sc.

A THESIS

SUBMITTED TO THE DEPARTMENT OF MATERIAL SCIENCE AND ENGINEERING

AND THE SCHOOL OF GRADUATE STUDIES

OF MCMASTER UNIVERSITY

IN PARTIAL FULFILMENT OF THE REQUIREMENTS

FOR THE DEGREE OF

DOCTOR OF PHILOSOPHY

McMaster University

Doctor of Philosophy (2025) McMaster University

(Material Science & Engineering) Hamilton, Ontario, Canada

TITLE:	THREE-DIMENSIONAL CHARACTERIZATION OF MORPHOLOGY AND CRYSTALLOGRAPHY OF LATH MARTENSITE IN MARTENSITIC STAINLESS STEELS
AUTHOR:	Mehdi Mosayebi, B.Sc., M.Sc. (University of Tehran)
SUPERVISOR:	Prof. Nabil Bassim
NUMBER OF PAGES	xix, 135

To my mom and dad

Anything good that has come to my life has been because of your love

Abstract

Lath martensite, a key microstructural feature in low-carbon martensitic stainless steels, plays a crucial role in determining the mechanical performance of these materials. Despite extensive research, the three-dimensional (3D) morphology, crystallographic characteristics, and hierarchical organization of lath martensite remain inadequately understood due to the limitations of conventional two-dimensional (2D) imaging techniques. This study employs a large-volume 3D electron backscatter diffraction (3D EBSD) approach combined with plasma-focused ion beam (PFIB) serial sectioning tomography to provide a comprehensive investigation of lath martensite in a 13Cr-4Ni martensitic stainless steel. The research presents novel insights into the morphology, habit plane variations, and boundary networks of lath martensite, contributing to a refined understanding of its formation mechanisms and mechanical implications.

The microstructural analysis reveals the hierarchical subdivision of martensite into prior austenite grains (PAGs), packets, blocks, and sub-blocks. Using 3D EBSD and Kurdjumov-Sachs (K-S) orientation relationship analysis, intervariant boundary networks were identified and classified, allowing a quantitative assessment of their role in the microstructure. The study highlights the presence of delta-ferrite particles and non-metallic inclusions, reconstructed in 3D to determine their spatial distributions and interactions with the martensitic matrix. Two distinct delta-ferrite morphologies were observed: elongated particles at PAG boundaries and smaller, spherical particles within PAG interiors. Furthermore, block and packet interactions were analyzed, revealing three primary types: hard impingement, mutual intersection, and interpenetration. These findings illustrate how the hierarchical arrangement of laths, blocks, and packets influences the overall boundary network complexity of the steel.

A detailed investigation into habit planes was conducted using 3D morphological and crystallographic reconstructions. The dominant habit plane, derived from the normal directions of high-angle block boundaries, was identified between $\{111\}\gamma$ and $\{557\}\gamma$, with an orientation of $(0.51,0.52,0.66)\gamma$. However, local habit plane deviations were detected in specific regions, primarily due to block bending and interactions between adjacent growing blocks. Spatial interference and growth competition within a single packet and hard impingement mechanisms

were found to affect growth paths, leading to macroscopic deflections in interface planes. These observations highlight the importance of considering local habit plane variations in martensitic transformation studies to avoid oversimplified interpretations.

Further analysis of the 3D spatial arrangement of packets within PAGs established a tetrahedral pattern governing their distribution. Through geometrical calculations, a direct correlation between this pattern and the dominant habit plane ({557}γ) was demonstrated, providing new insights into the 3D organization of lath martensite. The study also compared 3D-EBSD results with traditional 2D characterizations, revealing potential misinterpretations in habit plane orientation and block morphology when relying solely on 2D analyses. These findings emphasize the necessity of 3D approaches to accurately capture the complex nature of martensitic structures.

Overall, this research advances the understanding of lath martensite by integrating large-scale 3D reconstructions with crystallographic and morphological analyses. The results have significant implications for improving predictive models of microstructural evolution and mechanical behavior, aiding in the optimization of martensitic stainless steels for industrial applications such as hydroelectric turbine components and structural engineering materials. By correlating habit plane characteristics with the 3D morphology of martensitic structures, this study provides a foundation for future efforts in refining the processing and performance of these alloys.

Keywords: 3D electron backscatter diffraction, plasma focused ion beam (PFIB), lath martensite, 3D defect characterization, 3D boundary network, habit plane,

Acknowledgements

I would like to express my sincere gratitude to my supervisor Dr. Nabil Bassim for his guidance, encouragement, and support. His wide knowledge of microscopy and sharp vision of future trends formed the basis of this thesis. Furthermore, I would like to extend my appreciation to Dr. Hatem Zurob and Dr. Mukesh K. Jain for their participation as committee members during my Ph.D. Their invaluable insights, constructive feedback, and excellent suggestions have greatly contributed to the development of my research. I would like to thank my collaborators Dr. Daniel Paquet, Dr. Pierre-Antony Deschênes, Dr. Laurent Tôn-Thât and Carlo Baillargeonfor from Hydro-Québec Research Institute (IREQ) for many useful interactions and discussions. My gratitude also goes to my friends Dr. Alaleh Esfandiari, Dr. Aidin Barabi, Dr. Bita Pourbahari, Dr. Pardis Mohamadpour, Dr. Bhavesh Kamaliya, Caleb Whittier, Morvarid Ghorbani, Alyssa Williams, Bavley Guerguis and Betty Huang for generously sharing their thoughts and knowledge. Their help and friendship have made my Ph.D. journey an unforgettable experience. I also like to express my gratitude to Dr. Brian Langelier, Chris Butcher, Jhoynner Martinez, Travis Casagrande, and Sabaa Rashid from the Canadian Centre of Electron Microscopy (CCEM) for their invaluable assistance in microscopic trainings. Their generosity in sharing their insights and knowledge has been immensely helpful in my research journey. I would also like to thank the Natural Sciences and Engineering Research Council of Canada (grant RTI-2021-00699), Mitacs organization (grant IT38828) and Canada Foundation for Innovation (John Evans Leadership Fund) for financial support of this work. Finally, I would like to thank my family from the bottom of my heart. Their love, support, and understanding have been the foundation of my journey. They have made countless sacrifices and provided endless encouragement. Their presence has been a constant source of strength and motivation. I am truly grateful for their unwavering support. Thank you for being there for me every step of the way.

Table of Contents

List of Figures

List of Tables

Notation, Definitions, and Abbreviations

Abbreviations

BB	Block boundary
BC	Band contrast
BCC	Body-centered cubic
BCT	Body-centered tetragonal
CA6NM	Cast 13cr-4ni martensitic stainless steel
CCEM	Canadian centre of electron microscopy
CP	Close packed plane
CSL	Coincidence site lattice
EBSD	Electron backscatter diffraction
EDS	Energy-dispersive spectroscopy
FCC	Face-centered cubic
FIB	Focused ion beam
FSD	Forward scatter diode
HAB	High-angle boundary
HP	Habit plane
HSLA	High-strength low-alloy steel
IPF	Inverse pole figure
IREQ	Hydro-Québec Research Institute
K-S	Kurdjumov-Sachs
KAM	Kernel average misorientation
LAB	Low-angle boundary
N-W	Nishiyama-Wasserman
OR	Orientation relationship
PAG	Prior austenite grain
PAGB	Prior austenite grain boundary
PB	Packet boundary

PFIB	Plasma focused ion beam
ROI	Region of interest
SE	Secondary electron
SEM	Scanning electron microscopy
TEM	Transmission electron microscopy
XRD	X-ray diffraction
2D	Two-dimensional
3D	Three-dimensional
415	Wrought 13Cr-4Ni martensitic stainless steel

Notation

A	Surface area
Ac_1	Temperature where austenite formation begins during heating
Ac_3	Temperature where transformation to full austenite is complete during heating
A_f	Austenite finish temperature upon heating
A_s	Austenite start temperature upon heating
α	Ferrite phase
ED	Equivalent diameter
g	Transformation matrix
M_f	Martensite finish temperature
M_s	Martensitic start temperature
V	Volume
Σ	Coincidence site lattice (CSL) notation
Ψ	Sphericity factor
γ	Austenite phase
δ	Delta-ferrite phase
θ	Misorientation angle
$\Delta\Theta_{CP}^{\{111\}\gamma}$	Deviation of a habit plane from the theoretical $\{111\}\gamma$ habit plane

Declaration of Academic Achievement

This thesis was prepared in partial fulfillment of the requirements for the degree of Doctor of Philosophy at McMaster University. The research was conducted from May 2021 to April 2025 and focused on three-dimensional morphological and crystallographic characteristics of lath martensite in low-carbon martensitic stainless steels. The author carried out the experiments, performed data analysis, and prepared all manuscripts under the supervision of Professor Nabil Bassim. The major findings of this research have been published or are currently under review in peer-reviewed journals including "*Scripta Materialia"* and "*Materialia"*, with an additional manuscript in preparation for submission to "*Materials Characterization"*. It is acknowledged that *Elsevier Ltd.*, the publisher of "*Scripta Materialia"* and "*Materialia"*, allows authors to reuse their published articles in their theses or dissertations.

The following publications and manuscripts have resulted from this research:

1. Mehdi Mosayebi, Daniel Paquet, Pierre-Antony Deschênes, Laurent Tôn-Thât, Betty Huang, and Nabil Bassim. "On the correlation between the habit plane and 3D morphology of lath martensite: A direct 3D observation using serial sectioning tomography of a low-carbon stainless steel." Scripta Materialia**,** 255 (2025): 116367. https://doi.org/10.1016/j.scriptamat.2024.116367.
2. Mehdi Mosayebi, Pierre-Antony Deschênes, Daniel Paquet, Laurent Tôn-Thât, and Nabil Bassim. "Three-dimensional analysis of local and dominant habit planes in a lath martensitic stainless steel." Under review by Materialia. http://dx.doi.org/10.2139/ssrn.5193961.
3. Mehdi Mosayebi, Pierre-Antony Deschênes, Daniel Paquet, Laurent Tôn-Thât, and Nabil Bassim. "New insights into the morphology and crystallography of lath martensite using 3D EBSD characterization of a low-carbon stainless steel."
   In preparation for submission to Materials Characterization.

Chapter 1

Introduction

1.1 Background

1.1.1 Low-carbon 13Cr-4Ni martensitic stainless steels

Martensitic stainless steels are essentially alloys of iron, carbon, chromium, and nickel that transform into a body-centered tetragonal (BCT) crystal structure with rapid cooling to low temperatures [1,2]. The low-carbon 13Cr-4Ni martensitic alloys were developed as part of a research project aimed at creating stainless steels with enhanced mechanical properties and corrosion resistance, specifically for use in hydroelectric turbine runners. Its combination of high strength, toughness, and improved weldability made it an ideal choice for the demanding environments of hydroelectric applications, where materials are subjected to severe loading and corrosive conditions [3–6]. Conventional martensitic stainless steels were previously favored for this application, but their high susceptibility to hot cracking required careful adherence to extensive precautions during turbine repair welding procedures [7,8]. To minimize this risk, low-carbon martensitic stainless steels were developed, incorporating nickel to stabilize the austenite structure, resulting in a steel alloy with 13% Cr and 4% Ni. This composition provides a balanced combination of corrosion resistance, strength, fatigue resistance, and toughness, making it particularly suitable for hydroelectric turbine applications. The chromium content forms a protective passive oxide layer, enhancing corrosion resistance in water environments, while nickel improves toughness and reduces the risk of brittle fracture. Additionally, the low-carbon content minimizes hot cracking during welding, facilitating easier repairs and maintenance [3–6]. The

chemical composition range of 13Cr-4Ni steel is presented in Table 1.1, with its common specifications across various standards outlined in Table 1.2. This steel is available in both cast (CA6NM) and wrought (415) forms, making it a popular choice for manufacturing pipes, valves, and hydroelectric turbine runners. Wrought 415 stainless steel undergoes a series of thermomechanical processes, including hot working and heat treatment, which refine the grain structure, reduce porosity, and improve mechanical properties. This distinguishes it from its cast counterpart, CA6NM, which solidifies directly from the melt with minimal deformation. Both conditions offer an optimal balance of corrosion resistance and mechanical strength, making them well-suited for turbine runners operating in aqueous environments under high mechanical stress [4,5,9–13].

Table 1.1: Chemical composition ranges of 13Cr-4Ni steel adapted from ASTM A743 [5].

C	Cr	Ni	Mo	Mn	Si	P	S	Fe
0.06 max	11.5-14	3.5-4.5	0.4-1.0	0-1.0	0-1.0	0-0.03	0-0.04	Bal.

Table 1.2: Various standards and corresponding specifications for 13Cr-4Ni steel [5].

Standard	**Specification**	**Cast or Wrought**
EURONORM	1.4313-X4 Cr Ni Mo 13-4	Wrought
AFNOR	Z4CN13.4	Wrought
DIN	X5 Cr Ni 13-4,W.Nr. 1.4313	Wrought
AISI	Type 415	Wrought
UNS	S41500	Wrought-Electrode
ASTM	CA6NM	Cast
AISI-AWS	Type 410NiMo	Wrought-Electrode
UNS	J91540	Cast

The alloying elements in 13Cr-4Ni steel can be classified into two categories based on their influence on phase stability. Chromium and other elements known as "alpha stabilizers" promote the formation and stabilization of the ferrite phase (α, alpha). On the other hand, elements like carbon, manganese, and nickel act as "gamma stabilizers," enhancing the stability of the austenite phase (γ, gamma) by expanding its stability region in the steel's phase diagram. This increased austenite stability is particularly evident in iron-chromium alloying systems at lower temperatures. However, in martensitic steels, maintaining a relatively low concentration of gamma-stabilizing elements is crucial to ensure the austenite phase remains unstable and transforms into martensite at lower temperatures. Excessive gamma stabilizers may lead to the retention of austenite after the martensitic transformation, impacting the material's mechanical properties. A brief overview of the major alloying elements in this steel is provided below.

- **Effects of Chromium on Microstructure**

Chromium, a key alloying element in martensitic stainless steels, significantly affects their microstructure and mechanical properties, enhancing both strength and corrosion resistance. It promotes the formation of stable chromium carbides like $Cr_{23}C_6$ and Cr_7C_3, which contribute to the steel's hardness. Additionally, Chromium forms a protective oxide layer on the surface, preventing further oxidation and ensuring long-term corrosion resistance. To maintain this protective layer, over 12 wt% Cr must remain in the matrix, as excessive carbide formation can reduce corrosion resistance [14–18]. Chromium also influences the phase transformation behavior and can lead to the formation of δ-ferrite, a high-temperature body-centered cubic (BCC) phase that may persist after solidification [15,19]. While δ-ferrite can reduce the risk of hot cracking during manufacturing, excessive δ-ferrite formation can weaken the material's performance due to its lower strength and inferior corrosion resistance compared to martensite [5,15,17,20].

Therefore, careful control of chromium content is necessary to ensure the desired balance between strength, toughness, and corrosion resistance for industrial applications.

- **Effects of Nickel on Microstructure**

Nickel, as an austenite-stabilizing element, promotes the formation of the face-centered cubic (FCC) austenite phase, which is essential for enhancing stainless steel's corrosion resistance. This stabilization allows the steel to retain its austenitic structure during cooling, influencing further martensitic transformation. Additionally, by preventing the formation of ferrite, which typically reduces both corrosion resistance and toughness, nickel ensures the stability of the austenitic matrix . Austenite also offers a higher diffusion coefficient for elements like chromium compared to ferrite, which has a BCC structure. This increased diffusion promotes a greater concentration of chromium in the austenite phase, further improving the steel's ability to form a protective chromium oxide (Cr_2O_3) layer, which resists corrosion [21,22]. While nickel lowers the martensitic transformation temperature (M_s) by stabilizing austenite, it also reduces carbon solubility in the ferritic matrix. As a result, carbon is more likely to combine with chromium to form chromium carbides like $Cr_{23}C_6$, especially along grain boundaries [6]. This carbide formation causes localized chromium depletion, weakening the protective oxide layer and making the steel susceptible to intergranular corrosion. Therefore, careful control of nickel content is essential to maintain a proper balance between stabilizing austenite and preventing excessive carbide formation. By optimizing nickel levels, stainless steels can achieve an ideal combination of corrosion resistance, strength, and structural integrity, ensuring reliable performance in demanding environments [5,21,22].

- **Effects of Carbon on Microstructure**

Carbon is a gamma-stabilizer element, meaning it promotes the formation and stability of the austenite phase in stainless steels. Its effect on the microstructure is comparable to that of nickel, as both elements increase austenite stability and lower the martensitic transformation temperature (M_s) [6,23]. However, carbon has a more pronounced impact on the hardness and strength of martensitic stainless steels. The hardness of martensite is directly proportional to its carbon content, making carbon a critical factor in determining the steel's mechanical properties. While higher carbon levels enhance hardness and strength, they also come with certain drawbacks. Excessive carbon content can compromise the toughness and weldability of the steel, making it more susceptible to brittle fracture and weld cracking [7,8]. Additionally, carbon promotes the formation of chromium carbides, leading to chromium depletion in the surrounding matrix and thereby reducing the availability of chromium to form a protective Cr_2O_3 layer. To mitigate these issues, maintaining a low carbon content is essential, especially in applications requiring good corrosion resistance and mechanical performance. Instead of relying heavily on carbon for strength, alternative gamma-stabilizer elements like nickel or nitrogen can be used. These elements stabilize the austenite phase without causing extensive carbide precipitation, thereby preserving the corrosion resistance of the steel [5,23].

- **Effects of Molybdenum on Microstructure**

Molybdenum, like chromium, is an alpha-stabilizer element that promotes the formation of ferrite. It reduces the stability of the austenite phase by shrinking the gamma loop, thereby raising the critical temperatures (Ac_1 and Ac_3) required for austenite formation during heating. One of molybdenum's most notable effects is its ability to significantly enhance corrosion resistance, particularly against pitting and crevice corrosion. By strengthening the passive oxide film on the

steel's surface, molybdenum prevents localized corrosion, making it especially valuable in aggressive environments such as chloride-containing solutions and seawater [24–26]. This corrosion resistance makes molybdenum a key alloying element in marine, chemical, and desalination applications. Additionally, it enhances the high-temperature strength and creep resistance of stainless steels by forming stable Mo-rich carbides. These carbides contribute to improved mechanical performance, ensuring the steel's durability in demanding environments. Studies suggest that adding approximately 0.5–1.5% molybdenum can effectively increase the hardness, strength, and creep resistance of steels, particularly in high-temperature applications [26,27].

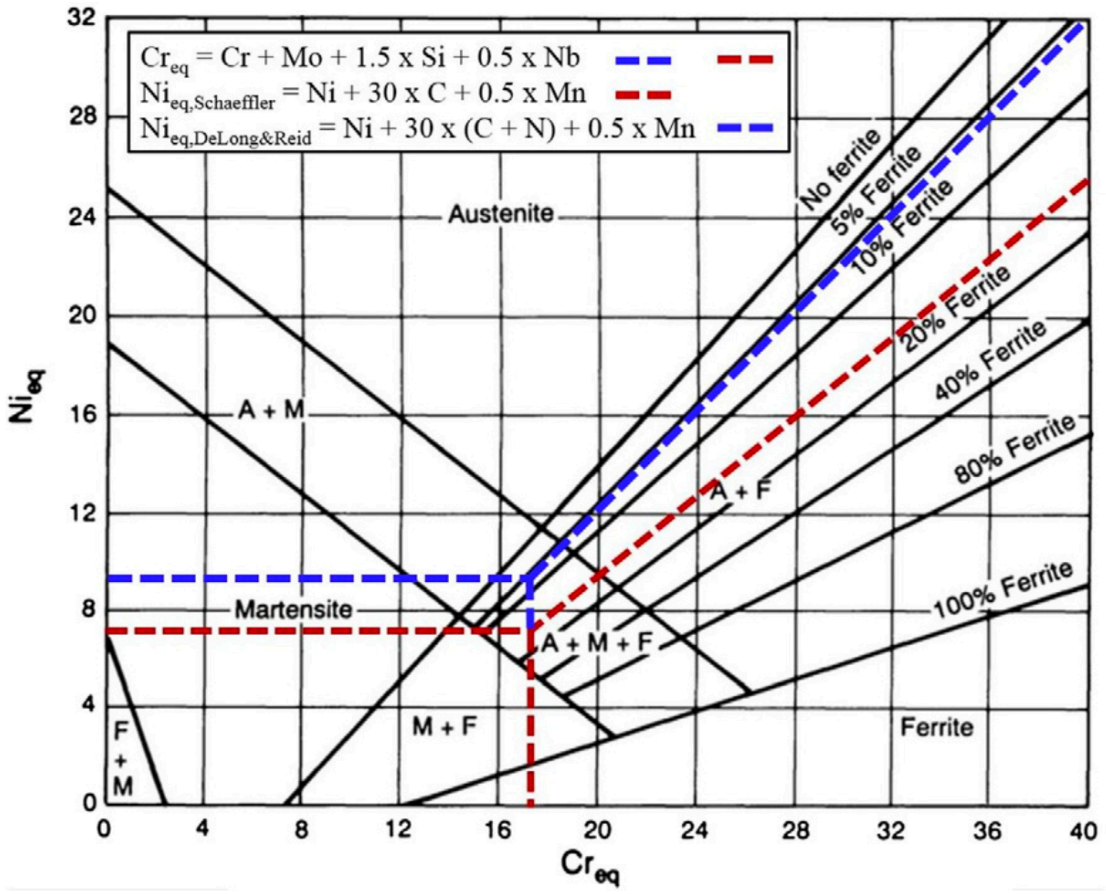

Figure 1.1: Schaeffler diagram illustrating the composition ranges of stainless steels [8,28].

steel microstructure formation during solidification is offered in the next following section.

Diagrams like the Schaeffler diagram (Figure 1.1) are often used to illustrate the influence of alloying elements on steel microstructures after solidification or welding. However, these diagrams have been found to lack accuracy when applied to low-carbon martensitic stainless steels [5,8]. While 13Cr-4Ni steel is typically considered to have a fully martensitic microstructure, the actual manufacturing process may result in a more complex microstructure that includes martensite, δ-ferrite, and retained austenite. Studies have shown that the final microstructure is influenced by factors such as the alloy composition, solidification process, and subsequent heat treatment history of the steel [3,5,6,22]. To better understand the formation of this complex microstructure, the following section provides a concise review of the solidification and phase transformation mechanisms in 13Cr-4Ni steel.

1.1.2 Solidification and martensitic transformation in 13Cr-4Ni stainless steels

The solidification process of 13Cr-4Ni martensitic stainless steel begins with the formation of δ-ferrite at approximately 1500 °C. δ-ferrite, characterized by its body-centered cubic (BCC) crystal structure, typically grows in the <001> crystallographic directions, aligning with the heat flow along the solidification front. As the temperature decreases, the δ-ferrite undergoes a transformation into austenite, usually occurring between 1300 °C and 1400 °C, depending on the steel's specific composition. Research indicates that this phase transformation follows a distinct orientation relationship, with the {110} planes of the δ-ferrite aligning parallel to the {111} planes of the austenite. The completion of the ferrite-to-austenite transformation takes place at high temperatures, generally below 1400 °C, resulting in a fully austenitic phase [1,2,5]. Figure 1.2 presents the Fe-Cr-Ni phase diagram, illustrating the equilibrium transformation temperatures and

phases of 13Cr-4Ni steel. According to the diagram, the steel begins solidification as δ-ferrite at around 1470 °C, achieving a completely δ-ferrite structure by approximately 1450 °C under equilibrium conditions. The subsequent transformation to austenite occurs at about 1300 °C, completing the phase change to a fully austenitic structure below 1230 °C. At lower temperatures, specifically below 720 °C, austenite can further transform into ferrite. However, this transformation is notably sluggish, making the formation of ferrite unlikely under typical cooling rates. This phase evolution during cooling is a key factor influencing the final microstructure and mechanical properties of 13Cr-4Ni stainless steel.

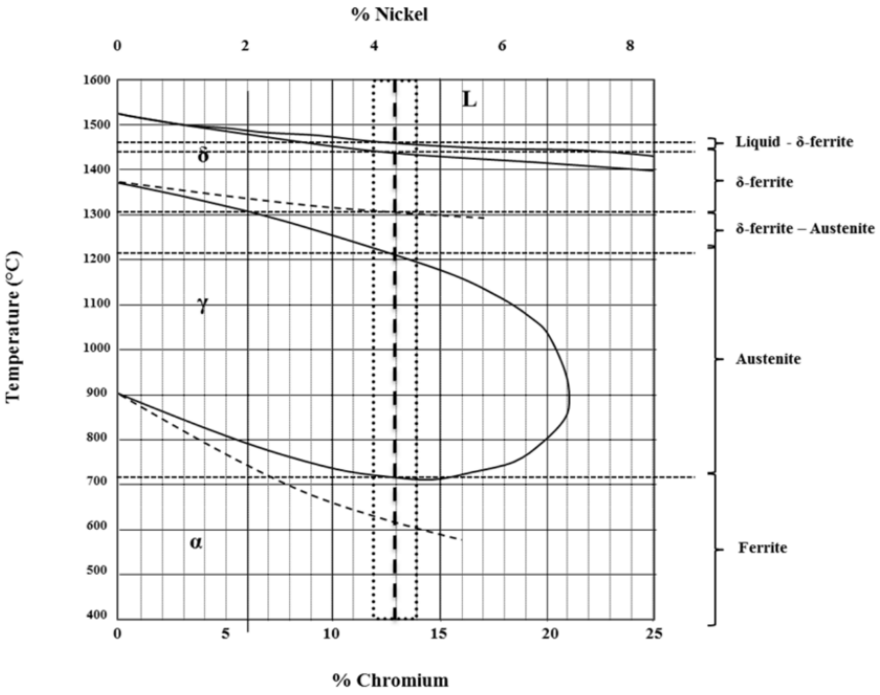

Figure 1.2: Phase diagram of 13Cr-4Ni stainless steel depicting equilibrium phase transformations. The dotted curves above and below the austenite region represent transformation temperatures during heating, providing insights into phase changes during heat treatments [5,7].

Figure 1.3 shows the continuous cooling transformation (CCT) diagram of 13Cr-4Ni steel. The diagram indicates that no α-ferrite transformation occurs under common cooling rates, even if the steel is held at temperatures close to A_{C1} for extended periods. Upon cooling, the martensitic

transformation proceeds rapidly, overtaking any other possible phase transformations once the temperature falls below the martensite start (M_s) temperature. This transformation is characterized by the absence of long-range atomic diffusion. Instead, it involves a homogeneous and coordinated movement of atoms, resulting in a structural change from the FCC austenite to BCT martensitic phase. Since the displacement of atoms occurs over interatomic distances with atoms retaining their relative positions, it is classified as a diffusionless transformation [1,2].

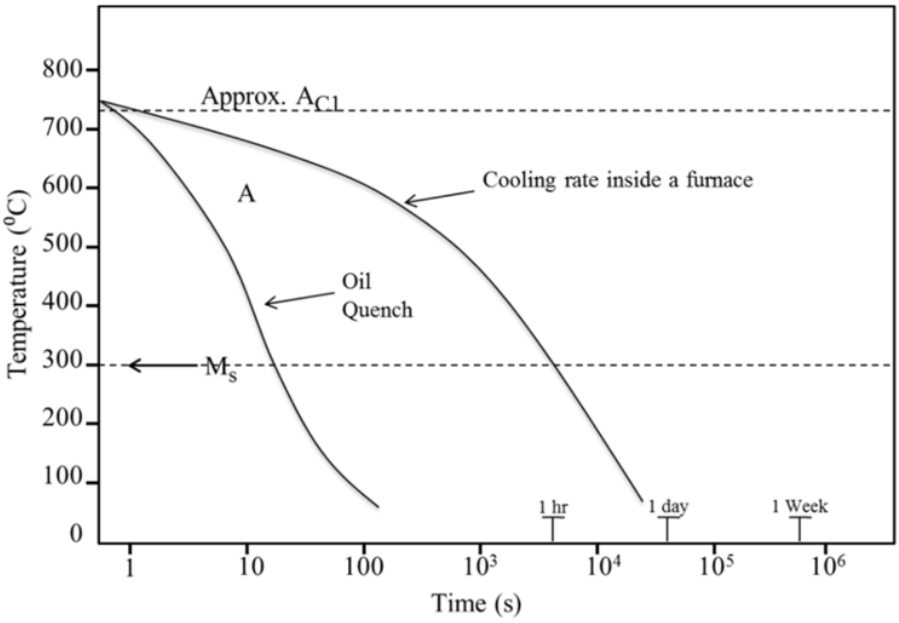

Figure 1.3: Schematic representation of the approximate isothermal transformation diagram for 13Cr-4Ni stainless steel. Curves representing common cooling rates, including quenching in oil and furnace cooling, are also illustrated [5,8].

Most alloying elements, with a few exceptions such as cobalt, generally reduce the martensite start temperature (M_s) in stainless steels. Among these, carbon has the most significant effect. Due to its strong austenite-stabilizing properties, even small amounts of carbon can drastically lower the M_s temperature. To estimate the M_s temperature, several empirical equations have been developed based on the composition of the steel. For martensitic stainless steels, the following

equation (Equation 1.1) is commonly used, providing a reliable prediction by incorporating the weight percentages of key alloying elements [2,5]:

$$M_S\ (°C) = 540\ (°C) - (497C + 6.3Mn + 36.3Ni + 10.8Cr + 46.6Mo)\ (°C) \quad (1.1)$$

This formula indicates that carbon has the strongest effect on decreasing the martensite start (M_s) temperature, followed by elements like Ni, Mo, Cr, and Mn. Martensitic stainless steels with low carbon content (typically less than 0.25 wt%) tend to have relatively high M_s temperatures, often ranging between 200 and 400 °C, depending on the exact alloy composition. Thibault et al. [3] calculated the M_s temperature of 13Cr-4Ni stainless steel to be approximately 300 °C. Since the martensite finish (M_f) temperature usually falls about 100 °C below the M_s, the transformation is expected to be completed at room temperature. However, in steels with nickel content above 4%, the M_f temperature may drop below room temperature, resulting in retained austenite within the microstructure [6,16,21].

The microstructure of 13Cr-4Ni stainless steel is therefore predominantly shaped by its martensitic transformation. Depending on the carbon content, martensite can adopt two primary morphologies: lath-shaped or plate-shaped. In Fe-C alloys, lath martensite forms in steels with carbon concentrations ranging from 0 to 0.6 wt.%, while plate martensite becomes the dominant form in steels with carbon contents above 1.0 wt.%. In the intermediate range of 0.6 to 1.0 wt.%, both morphologies may coexist, with the fraction of plate martensite increasing as carbon content rises. Since the carbon content of 13Cr-4Ni stainless steel is below 0.06%, its microstructure consists exclusively of lath martensite. This lath structure, characterized by a high density of dislocations and substructures, provides the steel with excellent strength, toughness, and fatigue

resistance, making it ideal for demanding applications like hydroelectric turbine runners [3–6,23,29].

Martensitic transformations are also defined by specific orientation relationships (ORs) between the parent austenite phase and the resulting martensite. These transformations introduce lattice distortions and surface reliefs due to the shear strain generated during the phase change. Several theoretical OR models describe the crystallographic relationships governing this transformation, including the Kurdjumov–Sachs (K–S), Nishiyama–Wassermann (N–W), Greninger–Troiano (G–T), and Pitch models (Table 1.3) [30]. The Bain OR, while fundamental in understanding the concept of martensitic transformation, is rarely observed in practice. In practice, however, the OR between the parent austenite and the transformed martensite often deviates from the theoretical models. Unlike the idealized parallel alignment of close-packed planes and directions, the transformed products typically retain a lattice invariant line. The actual OR is influenced by the differences in lattice parameters between the parent austenite and the martensite, which are further dependent on the steel's composition [30,31]. Moreover, the formation of martensitic laths induces shear strain in the adjacent austenite, generating local stresses. These stresses can cause gradual deviations in the austenite orientation, with variations of up to 5–6° within a single prior austenite grain [32]. This localized distortion adds complexity to the phase transformation process, leading to slight inconsistencies in the observed ORs of lath martensite and adjacent austenite. Such deviations also explain the variation in ORs reported for different low-alloy steels. While the Kurdjumov–Sachs (K–S) and Nishiyama–Wassermann (N–W) ORs are the most commonly observed, studies have shown discrepancies, with reported ORs ranging between these two models. Since K–S and N–W ORs differ by only 5.26°, minor shifts in local strain or compositional variations can account for these differences [30,33,34]. Additionally,

variations in reported ORs for low-carbon martensitic steels may be attributed to differences in characterization techniques. Transmission electron microscopy (TEM) has traditionally been used to investigate ORs, but its limited field of view and time-intensive analysis can result in small, localized observations. In contrast, electron backscatter diffraction (EBSD) provides a broader, statistically significant representation of orientation relationships by analyzing a large number of grains. Recent studies leveraging EBSD and computational advances have enabled more comprehensive and reliable conclusions on the ORs of martensitic steels, contributing to a deeper understanding of their transformation mechanisms [30,35].

Table 1.3: Ideal orientation relationships (ORs) between lath martensite (α) and parent austenite (γ) [30].

Orientation relationship	Parallelism	Number of variants
Bain (B)	$\{1\,0\,0\}_\gamma \| \{1\,0\,0\}_\alpha \langle 1\,0\,0\rangle_\gamma \| \langle 1\,1\,0\rangle_\alpha$	3
Kurdjumov–Sachs (K–S)	$\{1\,1\,1\}_\gamma \| \{1\,1\,0\}_\alpha \langle 1\,1\,0\rangle_\gamma \| \langle 1\,1\,1\rangle_\alpha$	24
Greninger–Troiano (G–T)	$\{1\,1\,1\}_\gamma \| \{1\,1\,0\}_\alpha \langle 1\,2\,3\rangle_\gamma \| \langle 1\,3\,3\rangle_\alpha$	24
Pitsch (P)	$\{1\,0\,0\}_\gamma \| \{1\,1\,0\}_\alpha \langle 1\,1\,0\rangle_\gamma \| \langle 1\,1\,1\rangle_\alpha$	12
Nishiyama–Wasserman (N–W)	$\{1\,1\,1\}_\gamma \| \{1\,1\,0\}_\alpha \langle 1\,1\,2\rangle_\gamma \| \langle 1\,1\,0\rangle_\alpha$	12

Given the low-carbon content of 13Cr-4Ni steel (less than 0.06%), its martensitic microstructure is closely associated with the K-S OR. In this relationship, the habit planes {111}γ in austenite are parallel to {011}α in martensite, with the orientation relationship expressed as {111}γ//{110}α and <101>γ//<111>α (Figure 1.4). During the martensitic phase transformation, the microstructure undergoes a three-level hierarchical subdivision: packet, block, and lath (Figure 1.5). Specifically, a single γ-phase crystal can evolve into 24 crystallographically distinct variants

(V1-V24), dictated by the symmetry of cubic system. These variants are grouped into four distinct crystallographic packets, as γ contains four close-packed (CP) {111} planes, with six variants corresponding to each {111} plane (Figure 1.4 and Table 1.4). Within a given packet, the variants share the same habit plane and are organized into variant pairs to form blocks, which are further subdivided into low-misorientation sub-blocks [1,2].

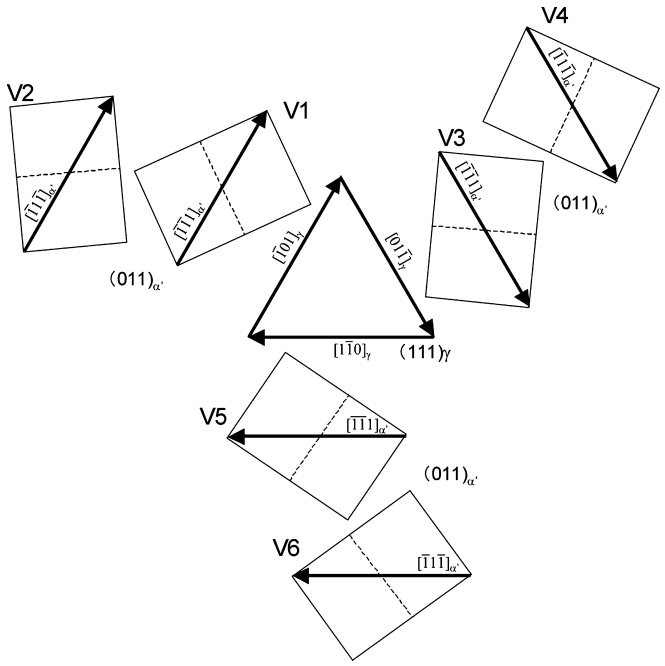

Figure 1.4: Representation of six crystallographic variants (V1–V6) based on the Kurdjumov–Sachs (K–S) orientation relationship, formed on a (111) austenite plane. The triangle represents the (111) plane of austenite (γ: face-centered cubic), while the rectangles indicate the corresponding (011) planes of martensite (α: body-centered cubic) [37].

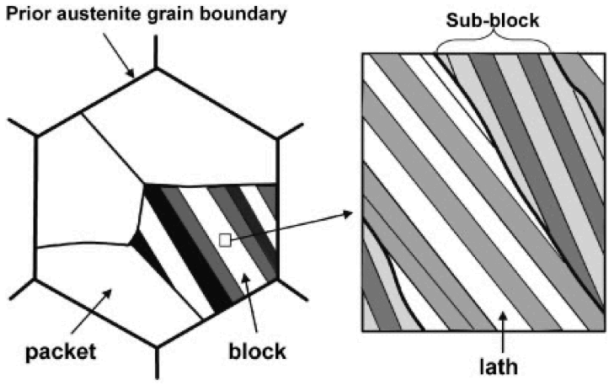

Figure 1.5: Schematic illustration depicting the hierarchical microstructure of martensitic stainless steels, showing the arrangement of packets, blocks, sub-blocks, and laths [35].

Table 1.4: Possible 24 variants generated through phase transformation having a K–S orientation relationship [30].

Variant	Plane parallel	Direction parallel	Rotation angle/axis from V1
V1	$(1\,1\,1)_\gamma \| (0\,1\,1)_\alpha$	$[-1\,0\,1]_\gamma \| [-1\,-1\,1]_\alpha$	–
V2		$[-1\,0\,1]_\gamma \| [-1\,1\,-1]_\alpha$	60°/[1 1 −1]
V3		$[0\,1\,-1]_\gamma \| [-1\,-1\,1]_\alpha$	60°/[0 1 1]
V4		$[0\,1\,-1]_\gamma \| [-1\,1\,-1]_\alpha$	10.53°/[0 −1 −1]
V5		$[1\,-1\,0]_\gamma \| [-1\,-1\,1]_\alpha$	60°/[0 −1 −1]
V6		$[1\,-1\,0]_\gamma \| [-1\,1\,-1]_\alpha$	49.47°/[0 1 1]
V7	$(1\,-1\,1)_\gamma \| (0\,1\,1)_\alpha$	$[1\,0\,-1]_\gamma \| [-1\,-1\,1]_\alpha$	49.47°/[−1 −1 1]
V8		$[1\,0\,-1]_\gamma \| [-1\,1\,-1]_\alpha$	10.53°/[1 1 −1]
V9		$[-1\,-1\,0]_\gamma \| [-1\,-1\,1]_\alpha$	50.51°/[−10 3 −13]
V10		$[-1\,-1\,0]_\gamma \| [-1\,1\,-1]_\alpha$	50.51°/[−7 −5 5]
V11		$[0\,1\,1]_\gamma \| [-1\,-1\,1]_\alpha$	14.88°/[13 5 1]
V12		$[0\,1\,1]_\gamma \| [-1\,1\,-1]_\alpha$	57.21°/[−3 5 6]
V13	$(-1\,1\,1)_\gamma \| (0\,1\,1)_\alpha$	$[0\,-1\,1]_\gamma \| [-1\,-1\,1]_\alpha$	14.88°/[5 −13 −1]
V14		$[0\,-1\,1]_\gamma \| [-1\,1\,-1]_\alpha$	50.51°/[−5 5 −7]
V15		$[-1\,0\,-1]_\gamma \| [-1\,-1\,1]_\alpha$	57.21°/[−6 −2 5]
V16		$[-1\,0\,-1]_\gamma \| [-1\,1\,-1]_\alpha$	20.61°/[11 −11 −6]
V17		$[1\,1\,0]_\gamma \| [-1\,-1\,1]_\alpha$	51.73°/[−11 6 −11]
V18		$[1\,1\,0]_\gamma \| [-1\,1\,-1]_\alpha$	47.11°/[−24 −10 21
V19	$(1\,1\,-1)_\gamma \| (0\,1\,1)_\alpha$	$[-1\,1\,0]_\gamma \| [-1\,-1\,1]_\alpha$	50.51°/[−3 13 10]
V20		$[-1\,1\,0]_\gamma \| [-1\,1\,-1]_\alpha$	57.21°/[3 6 −5]
V21		$[0\,-1\,-1]_\gamma \| [-1\,-1\,1]_\alpha$	20.61°/[3 0 −1]
V22		$[0\,-1\,-1]_\gamma \| [-1\,1\,-1]_\alpha$	47.11°/[−10 21 24]
V23		$[1\,0\,1]_\gamma \| [-1\,-1\,1]_\alpha$	57.21°/[−2 −5 −6]
V24		$[1\,0\,1]_\gamma \| [-1\,1\,-1]_\alpha$	21.06°/[9 −4 0]

The intricate interplay between this hierarchical morphology and the diverse K-S OR variants, creates an abundance of internal boundaries with varying misorientations and morphologies. Unlike diffusional transformations, such as ferrite formation, the boundary network in lath martensite emerges from the constraints imposed by the martensitic shear transformation, leading to highly intricate boundary morphologies [3–6]. This network, governed largely by crystallographic relationships [7,8], plays a pivotal role in dictating the extent of microstructural refinement and, consequently, the mechanical behavior of the material. By comparing all 24 K-S OR variants, 23 misorientation angle/axis sets can be computed. Some of these intervariant interfaces are identical because of crystal symmetry (e.g., V1-V3 and V1-V5 being identical), as reported earlier by others [30]. Therefore, the comparison of all 24 variants in the case of K–S OR reduces to only 16 independent misorientations (Table 1.4). As shown in Figure 1.6, these 16 misorientations cluster into two distinct ranges, forming a bimodal misorientation angle distribution. Consequently, each individual parent austenite grain can be partitioned by these 16 specific boundaries, which can serve as a basis for identifying microstructural constituents such as packets and blocks.

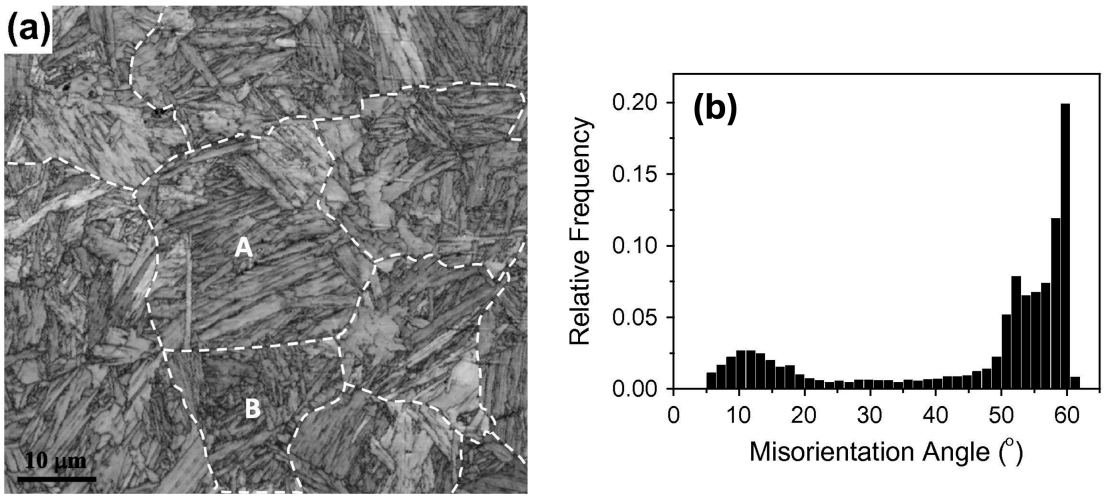

Figure 1.6: EBSD band contrast map and the corresponding misorientation angle distribution of a lath martensitic steel, as studied by Beladi et al. [30]

1.1.3 Focused ion beam (FIB) serial section tomography

Serial sectioning has been the most widely used method to acquire three-dimensional data for different materials at the meso- and micro-scales [9]. Application of this technique for the evaluation of metallic microstructures was first proposed by DeHoff in 1983 [46]. In the serial sectioning technique, the third dimension of the microstructure is revealed by a series of closely spaced parallel sections. The usual method for serial sectioning involves the sequential removal of parallel layers of the sample, interrupted by imaging (e.g., by EBSD technique) of the planar sections [47].

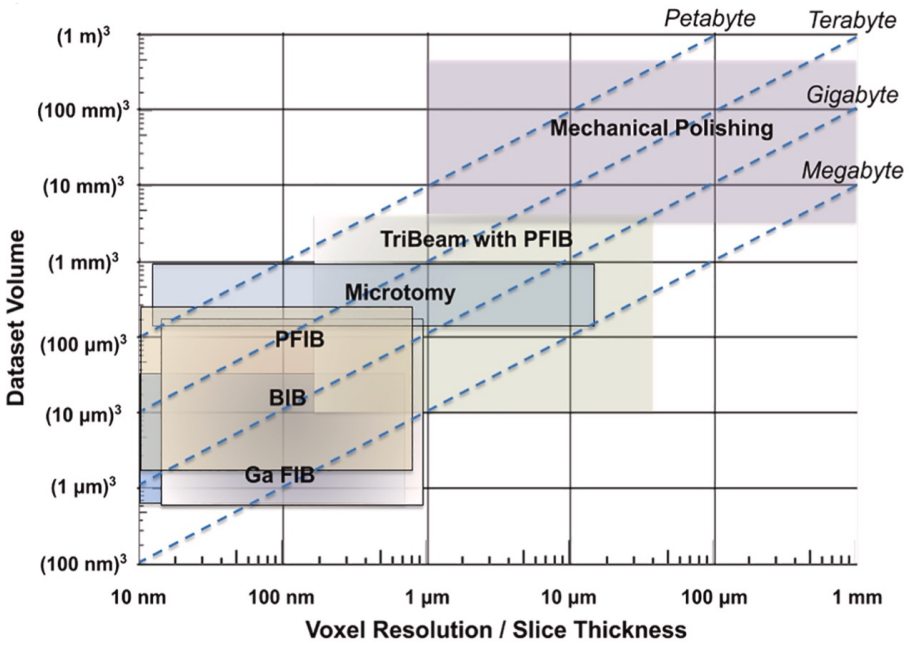

Figure 1.7: SEM-based serial sectioning techniques [47].

The removal of the material for serial sectioning can be performed with different methods: e.g., mechanical polishing, chemical polishing, Focused Ion Beam (FIB) milling, and laser or electrical discharge ablation (Figure 1.7). Among these methods, FIB tomography is one the most frequently used techniques, since it offers the best balance between high resolution and high field

width, due to the capability of the FIB column to focus highly energetic ions to small spot sizes (5-20 nm) and to perform cuts with a precise distance of approximately 10-15 nm. This technique is in fact a combination of serial sectioning with a focused ion beam (FIB) and orientation microscopy in a Dual-Beam system, which includes both an electron column and a Ga^+ ion column. These two independent beams can be focused on one coincident point in space and the sample's surface of interest is positioned at this point. The impact of the ion beam which usually consists of 30 kV ions with the surface of the sample leads to localized sputtering of the target material and can be used to mill into the surface and to remove the atoms by energy and momentum transfer of the ion to the substrate material [47–49].

Serial sectioning by conventional Ga^+ FIB tomography is, however, known as a time-consuming operation. For example, serial sectioning of a 20 × 20 × 20 μm³ volume of material using a 0.5 μm EBSD step size with a pattern solution rate of 50 frames per second and a 0.5 μm slice thickness (200 slices) requires at least 100 hours of acquisition time [45]. Even with modern EBSD cameras capable of achieving significantly higher speeds, with some cameras reaching up to 4500 frames per second depending on detector technology and experimental conditions, the limited material removal rate by Ga^+ FIB milling has restricted the role of serial sectioning by FIB tomography to the study of nano- and micrometer-scale features in volumes that have dimensions on the order of micrometers. Recently, Xe^+ plasma FIB (PFIB) has addressed the issue of volumetric coverage by offering a significantly higher beam current compared to Ga^+ FIB. Although the sputtering yield of Xe^+ PFIB is approximately 25% higher than that of Ga^+ FIB, its true advantage comes from its capability to operate at 30 to 40 times higher beam currents. This results in a substantial increase in material removal rates, making Xe^+ PFIB particularly effective for large-volume serial sectioning (Figure 1.8(a)) [50]. Moreover, Xe^+ PFIB introduces

significantly less ion implantation and amorphization into crystalline materials compared to Ga^+ FIB, minimizing sample damage. This characteristic is particularly advantageous for surface-sensitive techniques like EBSD, where maintaining crystal integrity is crucial. Despite the 30 to 40 times higher beam current, several studies have shown that the EBSD pattern quality remains superior with Xe^+ PFIB (Figure 1.8(b, c)) due to its reduced damage effects [50,51].

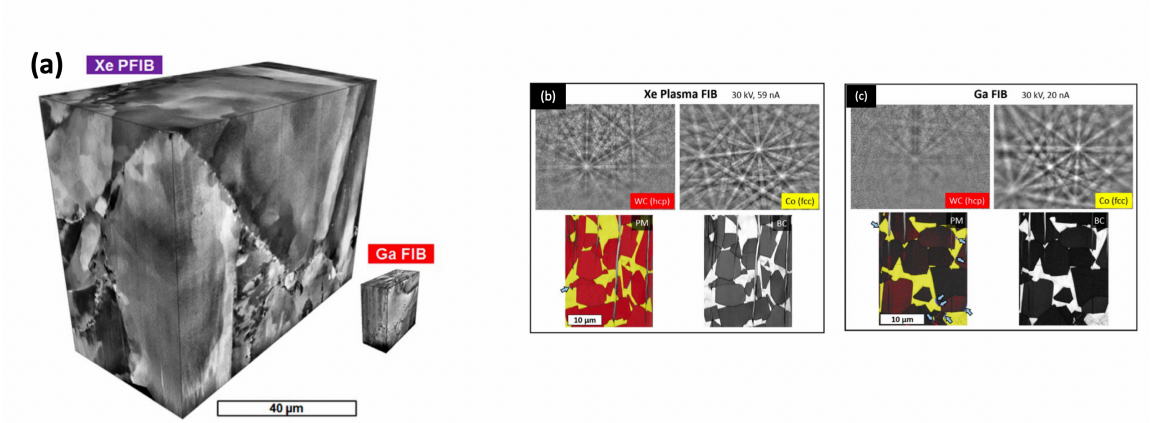

Figure 1.8: (a) 3D serial section volumes of a stainless steel collected using the PFIB-SEM (59nA at 30 kV, 100 nm slice thickness) and a FIB-SEM (1nA at 30 kV, 25 nm slice thickness) in similar times. EBSD results acquired under the same conditions showing representative phase maps, band contrast maps and raw patterns for WC-11wt.% Co for surfaces prepared by (b) Xe-PFIB and (c) Ga-FIB [50].

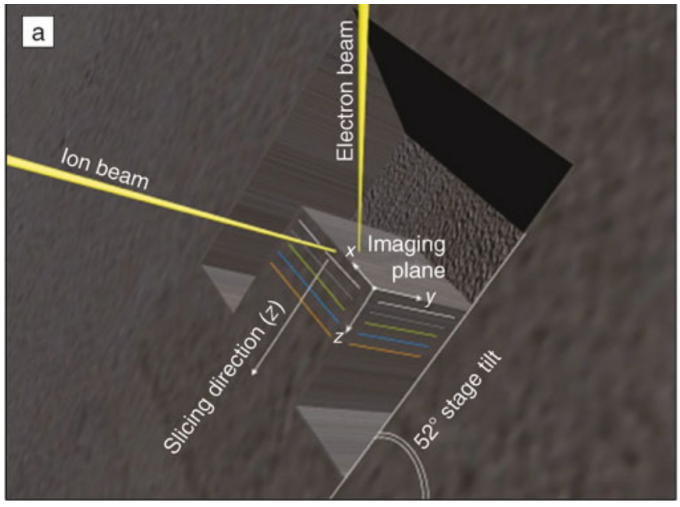

Figure 1.9: Illustration of serial slicing and imaging application of dual-beam platforms. Ion beam is used for creating cross sections, while electron beam allows for monitoring and imaging of the sliced regions [52].

To obtain a successful 3D tomogram using FIB, careful setups of sample geometry and software are needed. In a typical FIB-SEM instrument, the sample is mounted at the eucentric point, where the converging angle is usually achieved by a pre-tilt holder and adjusted tilting angle. Figure 1.9 shows the geometrical relationships between the sample, the electron, and the ion beams in a Dual-Beam microscope. The ion beam is used to prepare the imaging planes (X–Y sections) and the images are collected with the scanning electron beam in an alternating process. In some cases (depending on equipment setup), a sample rotation of 180 ° to an EBSD detector is needed when EBSD is being collected as well [45,49,51,52]. Schematic representation of this procedure is depicted in Figure 1.10 and Figure 1.11. The repetitive movement of the sample between FIB and EBSD positions during serial sectioning, can be set automatically using the appropriate software control scripts, where suitable parameters need to be determined in advance. Usually, the ion beam parameters are selected to optimize a relevant viewing width (x-y-parameter) and depth (z-parameter). The z-distance is dictated by how much of the sample is required to be milled and the thickness of each slice. Then, the dimensions of the image are selected in order to have a reasonable resolution relative to the features of importance within the serial-sectioned volume. The resolution of the data is extremely important in producing accurate statistics. A rule of thumb for 'quality' reconstructions and by association statistics is that a minimum of 10-20 sections is needed through a feature to accurately represent its size and shape [53]. Moreover, the obtained image series may appear to have artifacts like curtaining effects, which needs specific image processing algorithms to do some corrections before reliable results are achieved. After that, 3D reconstruction and segmentation can be performed to extract useful qualitative and quantitative information related to microstructure.

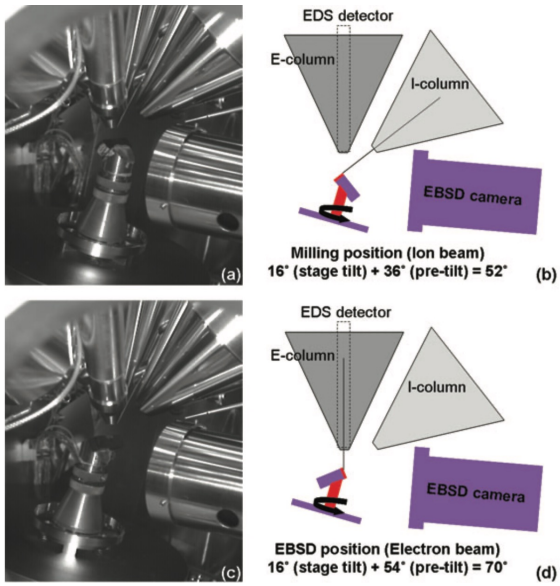

Figure 1.10: Photographs and schematic drawings of the sample setup in the EBSD-FIB tomography configuration with respect to the FIB/SEM beam directions and EBSD camera. (a and b) milling position (c and d) EBSD position [54].

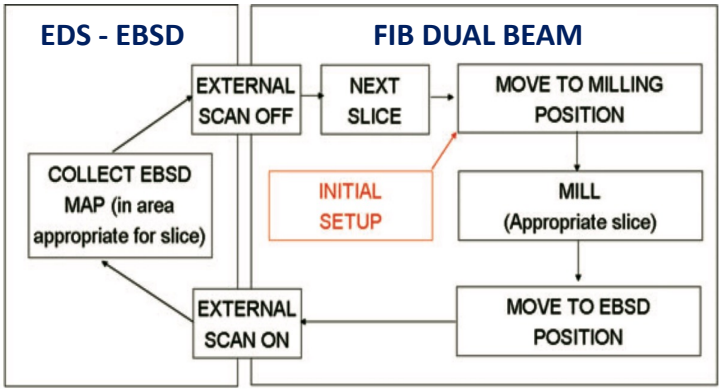

Figure 1.11: The automated data collection cycle for 3D EBSD acquisition [54].

Focused Ion Beam (FIB) tomography has become a pivotal technique for visualizing and characterizing three-dimensional (3D) microstructures, particularly due to its ability to capture grain-level details and crystallographic orientations (Figure 1.12 (a)) [49]. This method excels in analyzing small-scale features such as sub-grains, precipitates, and multiphase microstructures with dimensions around 10 μm or smaller (Figure 1.12 (b)) [55]. Recent advancements have extended FIB tomography to investigate complex phenomena like fatigue crack propagation. For

instance, Nishikawa et al. [56] utilized Plasma FIB (PFIB) combined with Electron Backscatter Diffraction (EBSD) to study microstructurally small fatigue cracks in a Ni-Co-based superalloy (Figure 1.13). Their work provided insights into the 3D crystallographic orientation of fatigue crack growth paths, revealing that major portions of the crack surfaces aligned closely with the {111} slip plane.

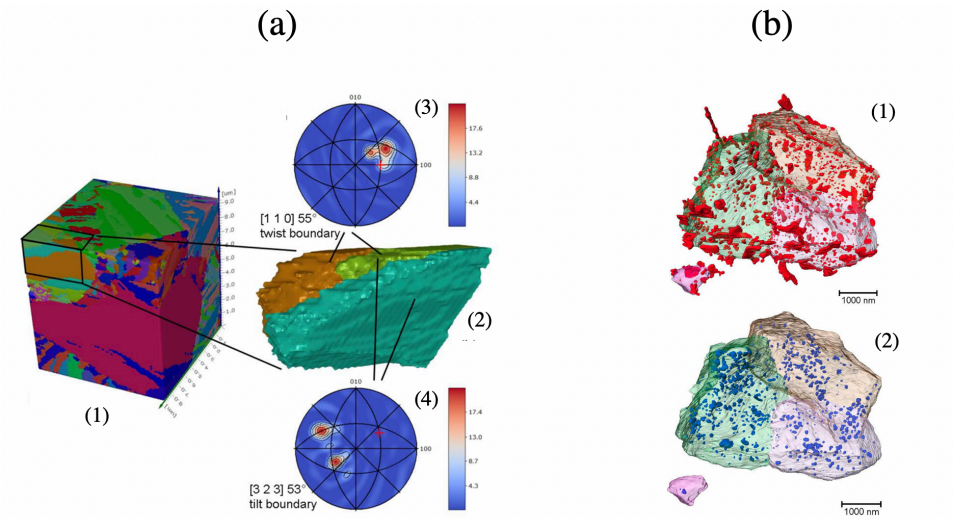

Figure 1.12: (a) 3D microstructure of an Fe-28%Ni alloy observed by FIB tomography [49]**:** (a1) 3D IPF map, (a2) three martensite plates taken from (a1), (a3) and (a4) twist-tilt pole figures of the interfaces between 2 grains, respectively, from (a2). **(b):** 3D FIB tomography of an AA7075-T651 alloy [55]**:** (b1) grain boundary precipitates, and (b2) precipitates inside the grains.

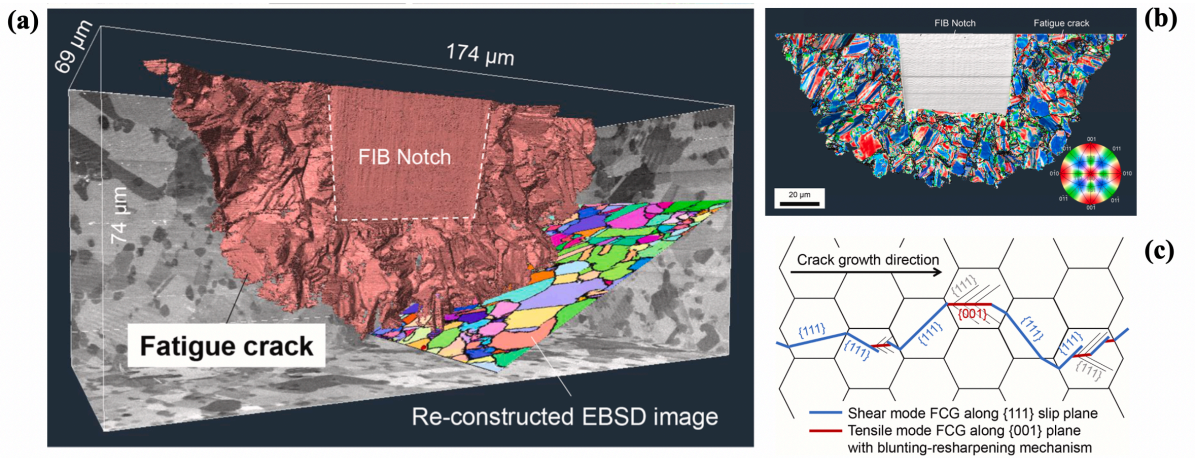

Figure 1.13: (a) Reconstructed 3D morphology of a microstructurally small fatigue crack in a Ni-Co-based superalloy. (b) MSFC morphologies represented as "crystal orientation of the crack surface". (c) Schematic of fatigue crack growth path [56].

In steel alloys, FIB tomography has elucidated the intricate 3D arrangements of microstructural features. Mangan et al. [57] demonstrated the 3D intersections of Widmanstätten plates, showing how they either impede or permit each other's growth. Similarly, Kral et al. [58] updated classical precipitate morphology classifications by incorporating 3D morphological data, enhancing the understanding of precipitate behaviors. Pioneering serial sectioning experiments have significantly advanced the comprehension of pearlite and martensitic structures. Hillert's work [59] revealed that pearlite colonies consist of single crystals of ferrite and cementite intertwined in a complex 3D pattern. This finding has deepened the understanding of pearlite formation mechanisms, including branching through morphological instability and ledge-wise growth. Notably, Hillert's original micrographs have been digitized to reconstruct the 3D architecture of pearlite colonies [59].

In lath martensitic steels, Morito et al. [40,60–62] employed EBSD combined with serial sectioning to analyze the morphology of lath martensite in high and low-carbon steels (Figure 1.14). Their studies revealed the hierarchical organization of prior austenite grains into packets, blocks, and sub-blocks, and clarified how these structural units form and evolve during martensitic transformation. In Fe–18Ni maraging steel [61], step-quenched specimens showed that packet nucleation predominantly initiates at prior austenite grain boundaries, with four packets forming along the boundary and a fifth growing inward from a triple junction. These packets initially form as single blocks, with selection influenced by Kurdjumov–Sachs (K–S) orientation relationships and shear directions parallel to austenite grain boundaries. In both ultra-low and high-carbon steels [62], coarse packets with volume fractions exceeding 10% dominate the prior austenite grains. Ultra-low carbon steels typically exhibit flat, plate-like packets with three block types, while high-carbon steels present sponge-like morphologies containing up to six block types. Small packets,

though more numerous in high-carbon steels, occupy significantly less volume. Additionally, their 3D reconstructions provided critical insight into the role of low-angle boundaries—namely, sub-block and fine packet boundaries—in morphological development [40]. Sub-blocks within a block often exhibit porous morphology and are frequently bounded by fine packets that share close-packed directions with neighboring regions. In interstitial-free steels, further classification of sub-blocks revealed dominant and minor variants based on volume fraction. Minor sub-blocks exhibited a plate-like morphology, were oriented with growth directions near ⟨101⟩, and were commonly aligned along habit planes close to {111}. The crystallographic relationship between dominant and minor sub-blocks showed a characteristic [011] misorientation of approximately 10.5°, adding to the understanding of internal structural organization within blocks. Similarly, Rowenhorst et al. [63] used this technique to investigate the 3D morphology of coarse martensite crystals in a commercial High-Strength Low-Alloy (HSLA) steel. Few other studies [40,64–66] utilized FIB tomography to examine the morphology and crystallography of single laths, block boundaries, and sub-block boundaries at higher resolutions. Despite significant progress, most previous studies, except for those reported by Morito et al [60–62], have primarily focused on small to mid-sized structural units, leaving gaps in understanding the larger-scale architecture of lath martensite, an aspect critical for accurate virtual mechanical testing and digital twin development of these steels. This limitation is mainly due to the challenging nature of 3D characterization in lath martensitic steels, which possess a highly hierarchical microstructure. With features ranging from nanometer-scale laths to PAGs exceeding hundreds of microns, capturing the complete microstructural landscape requires both high resolution and large-volume analysis. However, achieving both simultaneously has historically been difficult. Conventional Ga^+ FIB tomography offers exceptional resolution, making it ideal for investigating fine-scale features like

laths and sub-blocks. Yet, its low material removal rates restrict its ability to analyze larger volumes, preventing the capture of higher-level structural units such as blocks, packets, and PAGs. On the other hand, large-volume techniques such as mechanical polishing provide the necessary scale to examine PAG-level features but lack the resolution required to resolve finer details [45,52]. As a result, previous works have often been limited to small to medium-sized volumes using Ga^+ FIB for high-resolution imaging or, like some studies by Morito et al. [60–62], conducted at a larger scale using mechanical polishing but without the ability to observe smaller-scale features.

With the advent of Xe^+ PFIB and laser FIB systems, these challenges are now being addressed. Xe^+ PFIB provides significantly higher sputtering rates than Ga^+ FIB, enabling the simultaneous acquisition of large-volume and high-resolution 3D data. This capability makes it possible to investigate the entire microstructural hierarchy of lath martensite, from individual laths to the connectivity of blocks and packets within PAGs. Such comprehensive insights are essential for developing accurate models that capture the true behavior of these steels under real-world conditions. A detailed understanding of the 3D morphology and crystallography is essential for accurately predicting the behavior of lath martensitic steels under real-world conditions. Structural features such as block boundaries, packet interfaces, and prior austenite grain boundaries (PAGBs) significantly influence the steel's mechanical performance. The connectivity of these boundaries can determine the material's susceptibility to hydrogen embrittlement [38,67], resistance to fracture, fatigue, and stress corrosion cracking [64,68–70]. Without accurate 3D data, computational models may oversimplify these interactions, leading to discrepancies between predicted and actual performance. Capturing the true complexity of the material through 3D analysis allows researchers to build more reliable models that reflect the material's behavior under

operational conditions. This knowledge is particularly important for the development of virtual mechanical testing and digital twins. Virtual mechanical testing uses computational simulations to predict how a material will respond to applied stresses, strains, and environmental conditions, by applying techniques such as finite element analysis (FEA) or crystal plasticity modeling. These simulations, informed by accurate 3D microstructural data, enable the prediction of localized stress distributions, deformation mechanisms, and failure modes. In lath martensitic steels, virtual testing helps to identify weak points, evaluate fracture resistance, and optimize material design for improved durability [53,71–74]. Digital twins, on the other hand, serve as virtual representations of physical materials, continuously updated with data from sensors and simulations. For critical components such as hydroelectric turbine runners, digital twins can provide real-time insights into the material's performance. By incorporating 3D data from techniques like PFIB-EBSD and integrating it with operational data, digital twins enable predictive maintenance, identify potential failure risks, and optimize system performance. In addition, they allow manufacturers to simulate and test design modifications virtually, reducing the need for physical prototyping.

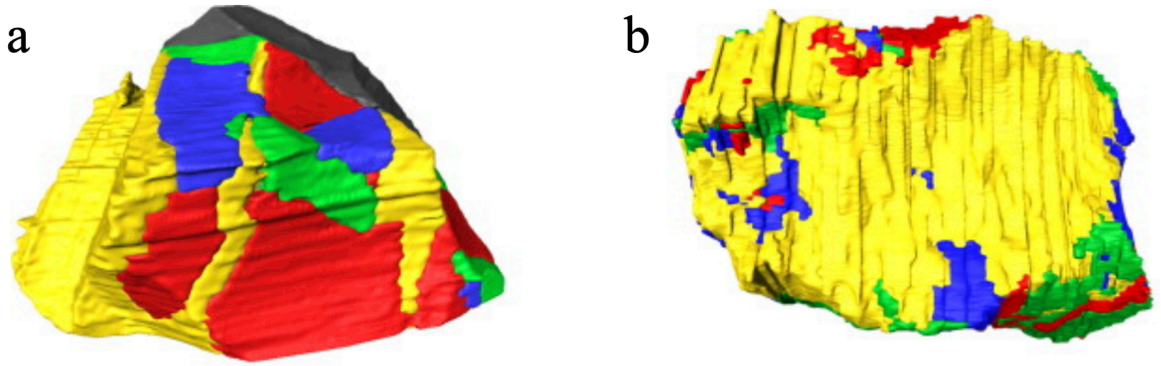

Figure 1.14: 3D visualization of martensite packets in two prior austenite grains: (a) a low carbon steel and (b) a high-carbon steel, with packets distinguished by different colors [62].

1.2 Motivations

Hydropower remains one of the most widely used renewable energy sources for electricity generation. With hydropower systems often operating for over five decades, ensuring proper design and manufacturing is essential to maintain high performance while minimizing operational and maintenance costs. Central to these systems is the hydraulic turbine, which consists of key components such as runner blades, crowns, and bands (Figure 1.15) [11–13]. Among the materials used for these critical components, low-carbon 13Cr-4Ni martensitic stainless steel is particularly preferred due to its balanced combination of corrosion resistance and mechanical strength, making it well-suited for turbine runners operating in aqueous environments under high mechanical stress [3–6]. Despite these advantages, the microstructure of low-carbon 13Cr-4Ni stainless steel presents significant challenges. Its martensitic structure exhibits a hierarchical arrangement of packets, blocks, sub-blocks, and laths [34,75–77]. This multiscale, complex structure has a considerable influence on the steel's mechanical behavior and corrosion resistance. Although extensive research has been conducted on hydroelectric turbine alloys, understanding the 3D crystallography and morphology of lath martensite remains limited. The primary challenge lies in accurately characterizing such intricate and spatially varying microstructures, which are essential for predicting the material's long-term performance. In recent years, advancements in 3D characterization techniques have provided valuable insights into the microstructures of various metallic materials, including steels, aluminum, nickel, and titanium alloys [55,56,78–81]. However, applying these methods to lath martensitic steels remains challenging. Several large-volume tomography techniques, including X-ray Computed Tomography (XCT) and mechanical polishing serial sectioning, have been widely used for the 3D characterization of millimeter-sized polycrystalline specimens. While effective for simpler microstructures, these methods have

inherent limitations when applied to lath martensite. For instance, X-ray Diffraction Contrast Tomography (DCT) can rapidly acquire crystallographic orientation, morphology, and phase information in large specimens [82–85]. However, due to the complex and highly diverse crystallographic orientations within lath martensite, DCT becomes ineffective for analyzing these microstructures. On the other hand, mechanical polishing serial sectioning tomography, an alternative for capturing larger volumes compared to traditional FIB tomography, is inherently slow, prone to section misalignment, and struggles to resolve nanoscale features. The manual nature of mechanical polishing introduces variability in data quality, limiting the accuracy of 3D reconstructions [45,47]. These limitations result in incomplete 3D datasets, hindering efforts to comprehensively understand the microstructural characteristics of lath martensitic steels. This lack of accurate data also impacts computational modeling. Consequently, predictions of mechanical behavior, failure mechanisms, and damage progression in martensitic steels remain uncertain, limiting the effectiveness of virtual mechanical testing and digital twin models. Advanced techniques like Xe^+ PFIB combined with EBSD provide a powerful solution to these challenges. Xe^+ PFIB offers higher material removal rates, enabling large-volume 3D data acquisition with nanometer-scale resolution. Additionally, EBSD provides accurate crystallographic orientation data, capturing the essential details of lath martensite's hierarchical structure [50,51]. This comprehensive 3D characterization is critical for developing reliable simulations and predictive models. A thorough understanding of the 3D microstructure of low-carbon martensitic stainless steels will significantly enhance the accuracy of computational models used in virtual mechanical testing and digital twin applications. This will enable more precise predictions of long-term performance, improve damage assessment capabilities, and support the development of optimized

maintenance schedules. Ultimately, advancing 3D characterization methods will contribute to safer, more efficient, and longer-lasting hydropower systems.

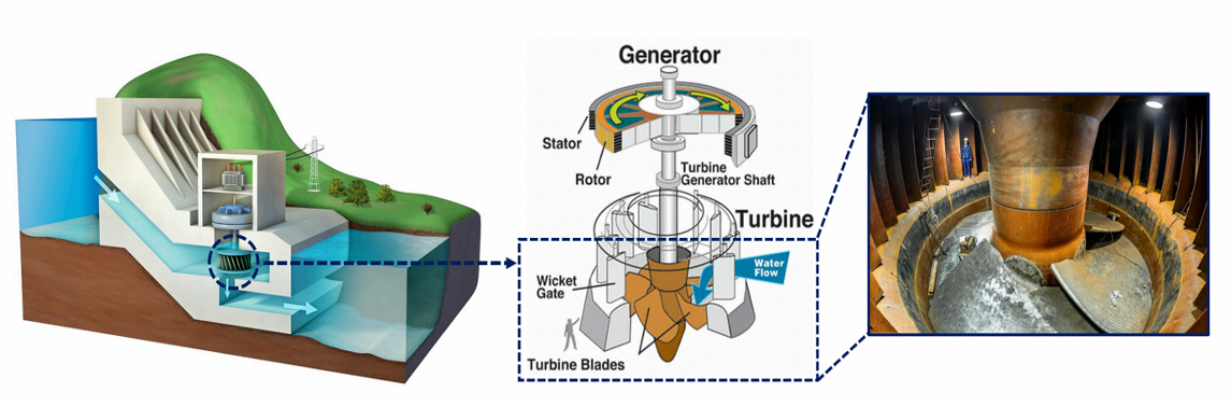

Figure 1.15: Schematic illustration of a hydropower system including generator, turbine, and turbine blade runners [11-13].

1.3 Research Objectives

Based on the literature review and the needs of our industrial partner, Hydro-Quebec, for a deeper understanding of the microstructure of hydro-turbine alloys, this thesis aims to develop a comprehensive 3D characterization of the crystallography and morphology of CA6NM alloy, the cast version of low-carbon 13Cr-4Ni martensitic stainless steel. The specific objectives of this research are:

1. Comprehensive 3D characterization of lath martensite and its hierarchical microstructure using high-precision, large field-of-view Xe^+ PFIB serial sectioning tomography combined with EBSD analysis. This approach enables the systematic identification, quantification, and classification of key microstructural constituents at different scales—from prior PAGs in the range of hundreds of microns to sub-blocks with widths of a few microns—providing critical insight into the martensitic structure of a real hydro-turbine alloy.

2. Correlated 3D PFIB-EBSD reconstruction of other critical microstructural components, including δ-ferrite particles, non-metallic inclusions, and casting defects. Simultaneous EBSD and SEM data acquisition will allow for a detailed investigation of their morphologies, spatial distributions, and interactions within the martensitic matrix.
3. Crystallographic and morphological characterization of internal boundary networks in 3D, focusing on the interfaces formed during the austenite-to-martensite transformation. To date, no comprehensive 3D analysis has been conducted on these interface structures, which play a crucial role in determining the mechanical properties of the alloy.
4. Integration of 3D EBSD findings into the broader theories of martensitic transformation, including martensite variant identification, habit plane determination, and interface analysis, to enhance the fundamental understanding of transformation mechanisms in low-carbon martensitic steels.

This research will provide valuable insights into the 3D microstructural evolution of CA6NM hydro-turbine alloys, supporting both academic advancements and industrial applications.

1.4 Thesis outline

This thesis comprises the following chapters which presents the findings of the research through three journal papers.

Chapter 1 – This chapter briefly presents the background of low-carbon 13Cr-4Ni martensitic stainless steels and FIB serial section tomography. It also discusses the motivation behind this research and outlines the research objectives.

Chapter 2 – This chapter presents a draft manuscript of a journal paper entitled "New insights into the morphology and crystallography of lath martensite using 3D EBSD characterization of a

low-carbon stainless steel". The paper provides a comprehensive 3D analysis of lath martensite in CA6NM martensitic stainless steel**,** focusing on the systematic identification, classification, and quantification of its key microstructural components.

Chapter 3 – This chapter presents a journal paper entitled "3D analysis of local and dominant habit planes in a lath martensitic stainless steel", which is currently submitted to *Materialia* journal. The paper demonstrates the application of large-volume 3D EBSD for reconstructing the 3D morphology of lath martensite and analyzing both dominant and local HPs in a lath martensitic stainless steel.

Chapter 4 – This chapter presents a journal paper entitled " On the correlation between the habit plane and 3D morphology of lath martensite: A direct 3D observation using serial sectioning tomography of a low-carbon stainless steel " published in the *Scripta Materialia* journal. This paper highlights the importance of 3D characterizations in understanding the lath martensite morphology and crystallography, and provides new insights into 3D architecture of lath martensite through establishing a direct link between the dominant habit plane and the spatial arrangement of the packets in 3D.

Chapter 5 – This chapter summarizes the main findings of this thesis and presents suggestions for future works, and highlights the contributions of this thesis to the literature.

References

[1] Porter DA, Easterling KE, Sherif MY. Phase Transformations in Metals and Alloys. Boca Raton: CRC Press; 2021. https://doi.org/10.1201/9781003011804.

[2] Nishiyama Z. Martensitic transformation. Elsevier; 2012.

[3] Thibault D, Bocher P, Thomas M, Gharghouri M, Côté M. Residual stress characterization in low transformation temperature 13%Cr–4%Ni stainless steel weld by neutron diffraction and the contour method. Materials Science and Engineering: A 2010;527:6205–10. https://doi.org/10.1016/j.msea.2010.06.035.

[4] Casas WJP, Henke SL, Novicki N. Fracture toughness of CA6NM alloy, quenched and tempered, and of its welded joint without PWHT. Welding International 2009;23:166–72. https://doi.org/10.1080/09507110802543344.

[5] Mokhtabad Amrei M. Characterization of microstructure and texture of 13Cr4Ni martensitic stainless steel weld before and after tempering, Doctoral dissertation, École de technologie supérieure, 2016.

[6] Zheng H, Ye XN, Li JD, Jiang LZ, Liu ZY, Wang GD, et al. Effect of carbon content on microstructure and mechanical properties of hot-rolled low carbon 12Cr–Ni stainless steel. Materials Science and Engineering: A 2010;527:7407–12. https://doi.org/10.1016/j.msea.2010.08.023.

[7] Folkhard E. Welding Metallurgy of Stainless Steels. . Berlin: Springer-Verlag; 1988.

[8] Lippold JC, Kotecki DJ. Welding Metallurgy and Weldability of Stainless Steels. John Wiley & Sons; 2005.

[9] Liu X, Luo Y, Wang Z. A review on fatigue damage mechanism in hydro turbines. Renewable and Sustainable Energy Reviews 2016;54:1–14. https://doi.org/10.1016/j.rser.2015.09.025.

[10] Trudel A, Lévesque M, Brochu M. Microstructural effects on the fatigue crack growth resistance of a stainless steel CA6NM weld. Eng Fract Mech 2014;115:60–72. https://doi.org/10.1016/j.engfracmech.2013.11.013.

[11] Liu X, Luo Y, Wang Z. A review on fatigue damage mechanism in hydro turbines. Renewable and Sustainable Energy Reviews 2016;54:1–14. https://doi.org/10.1016/j.rser.2015.09.025.

[12] Gagnon M, Tahan A, Bocher P, Thibault D. On the Fatigue Reliability of Hydroelectric Francis Runners. Procedia Eng 2013;66:565–74. https://doi.org/10.1016/j.proeng.2013.12.108.

[13] Sabourin M, Thibault D, Bouffard DA, Lévesque M. New parameters influencing hydraulic runner lifetime. IOP Conf Ser Earth Environ Sci 2010;12:012050. https://doi.org/10.1088/1755-1315/12/1/012050.

[14] Brooks AR, Clayton CR, Doss K, Lu YC. On the Role of Cr in the Passivity of Stainless Steel. J Electrochem Soc 1986;133:2459–64. https://doi.org/10.1149/1.2108450.

[15] Ofner N, Bodner SC, Kunnas P, Asci A, Kutleša K, Stark A, et al. Influence of increasing chromium content on additively manufactured tool steels: Microstructural and mechanical evolution before and after heat treatment. Journal of Materials Research and Technology 2025;34:2715–27. https://doi.org/10.1016/j.jmrt.2024.12.169.

[16] Wu W, Hwu LY, Lin DY, Lee JL. The relationship between alloying elements and retained austenite in martensitic stainless steel welds. Scr Mater 2000;42:1071–6. https://doi.org/10.1016/S1359-6462(00)00339-0.

[17] Yu Y, Shironita S, Souma K, Umeda M. Effect of chromium content on the corrosion resistance of ferritic stainless steels in sulfuric acid solution. Heliyon 2018;4:e00958. https://doi.org/10.1016/j.heliyon.2018.e00958.
[18] Chi H, Pian L, Gu J, Sun Y, Pang X, Xin Z, et al. Effect of Cr on the Microstructure and Strength-Toughness of High-Strength and Heat-Resistant Stainless Steel. Steel Res Int 2024;95. https://doi.org/10.1002/srin.202400412.
[19] Silva Filho JF da, Oliveira CAS de, Fonstein N, Girina O, Miranda FJF, Drumond J, et al. Effect of Cr Additions on Ferrite Recrystallization and Austenite Formation in Dual-Phase Steels Heat Treated in the Intercritical Temperature Range. Materials Research 2016;19:258–66. https://doi.org/10.1590/1980-5373-MR-2015-0641.
[20] Wang P, Lu SP, Xiao NM, Li DZ, Li YY. Effect of delta ferrite on impact properties of low carbon 13Cr-4Ni martensitic stainless steel. Materials Science and Engineering: A 2010;527:3210–6. https://doi.org/10.1016/j.msea.2010.01.085.
[21] Mohrbacher H, Kern A. Nickel Alloying in Carbon Steel: Fundamentals and Applications. Alloys 2023;2:1–28. https://doi.org/10.3390/alloys2010001.
[22] Pratomo SB, Oktadinata H, Widodo TW. Effect of nickel additions on microstructure evolution and mechanical properties of low-alloy Cr-Mo cast steel. IOP Conf Ser Mater Sci Eng 2019;541:012050. https://doi.org/10.1088/1757-899X/541/1/012050.
[23] Trillo EA, Murr LE. Effects of carbon content, deformation, and interfacial energetics on carbide precipitation and corrosion sensitization in 304 stainless steel. Acta Mater 1998;47:235–45. https://doi.org/10.1016/S1359-6454(98)00322-X.
[24] Ostovan F, Shafiei E, Toozandehjani M, Mohamed IF, Soltani M. On the role of molybdenum on the microstructural, mechanical and corrosion properties of the GTAW AISI 316 stainless steel welds. Journal of Materials Research and Technology 2021;13:2115–25. https://doi.org/10.1016/j.jmrt.2021.05.095.
[25] Bhole SD, Nemade JB, Collins L, Liu C. Effect of nickel and molybdenum additions on weld metal toughness in a submerged arc welded HSLA line-pipe steel. J Mater Process Technol 2006;173:92–100. https://doi.org/10.1016/j.jmatprotec.2005.10.028.
[26] Akashi M, Kawamoto T. The Effect of Molybdenum Addition on SCC Susceptibility of Stainless Steels in Oxygenated High Temperature Water. CORROSION ENGINEERING 1978;27:165–71. https://doi.org/10.3323/jcorr1974.27.4_165.
[27] Pardo A, Merino MC, Coy AE, Viejo F, Arrabal R, Matykina E. Effect of Mo and Mn additions on the corrosion behaviour of AISI 304 and 316 stainless steels in H2SO4. Corros Sci 2008;50:780–94. https://doi.org/10.1016/j.corsci.2007.11.004.
[28] Niessen F, Tiedje NS, Hald J. Kinetics modeling of delta-ferrite formation and retainment during casting of supermartensitic stainless steel. Mater Des 2017;118:138–45. https://doi.org/10.1016/j.matdes.2017.01.026.
[29] Stormvinter A, Miyamoto G, Furuhara T, Hedström P, Borgenstam A. Effect of carbon content on variant pairing of martensite in Fe-C alloys. Acta Mater 2012;60:7265–74. https://doi.org/10.1016/j.actamat.2012.09.046.
[30] Beladi H, Nuhfer NT, Rohrer GS. The five-parameter grain boundary character and energy distributions of a fully austenitic high-manganese steel using three dimensional data. Acta Mater 2014;70:281–9. https://doi.org/10.1016/j.actamat.2014.02.038.
[31] Christian JW. Simple geometry and crystallography applied to ferrous bainites. Metallurgical Transactions A 1990;21:799–803. https://doi.org/10.1007/BF02656562.

[32] Kelly PM. The martensite transformation in steels with low stacking fault energy. Acta Metallurgica 1965;13:635–46. https://doi.org/10.1016/0001-6160(65)90126-4.
[33] Hutchinson B, Hagström J, Karlsson O, Lindell D, Tornberg M, Lindberg F, et al. Microstructures and hardness of as-quenched martensites (0.1–0.5%C). Acta Mater 2011;59:5845–58. https://doi.org/10.1016/j.actamat.2011.05.061.
[34] Kelly PM, Jostsons A, Blake RG. The orientation relationship between lath martensite and austenite in low carbon, low alloy steels. Acta Metallurgica et Materialia 1990;38:1075–81. https://doi.org/10.1016/0956-7151(90)90180-O.
[35] Morito S, Adachi Y, Ohba T. Morphology and crystallography of Sub-blocks in ultra-low carbon lath martensite steel. Mater Trans 2009;50:1919–23. https://doi.org/10.2320/matertrans.MRA2008409.
[36] Morito S, Huang X, Furuhara T, Maki T, Hansen N. The morphology and crystallography of lath martensite in alloy steels. Acta Mater 2006;54:5323–31. https://doi.org/10.1016/j.actamat.2006.07.009.
[37] Kitahara H, Ueji R, Tsuji N, Minamino Y. Crystallographic features of lath martensite in low-carbon steel. Acta Mater 2006;54:1279–88. https://doi.org/10.1016/j.actamat.2005.11.001.
[38] Mirzaei A, Barrett CD, Ma X, Hodgson PD, Beladi H. On the propensity of lath martensite intervariant boundaries to hydrogen absorption using molecular statics simulation. Materialia (Oxf) 2022;25. https://doi.org/10.1016/j.mtla.2022.101539.
[39] Beladi H, Rohrer GS, Rollett AD, Tari V, Hodgson PD. The distribution of intervariant crystallographic planes in a lath martensite using five macroscopic parameters. Acta Mater 2014;63:86–98. https://doi.org/10.1016/j.actamat.2013.10.010.
[40] Morito S, Pham AH, Ohba T, Hayashi T, Furuhara T, Miyamoto G. Three-dimensional observations of morphology of low-angle boundaries in ultra-low carbon lath martensite. Microscopy 2017;66:380–7. https://doi.org/10.1093/jmicro/dfx027.
[41] Morito S, Hayashi T, Ohba T, Adachi Y. The relationship between microstructural units and their boundary natures in ultra-low carbon lath martensite. n.d.
[42] Beladi H, Tari V, Rohrer GS. On Σ9 grain boundary plane orientation. Materialia (Oxf) 2022;25. https://doi.org/10.1016/j.mtla.2022.101540.
[43] Mirzaei A, Ghaderi R, Hodgson PD, Ma X, Rohrer GS, Beladi H. The influence of parent austenite characteristics on the intervariant boundary network in a lath martensitic steel. J Mater Sci 2022;57:8904–23. https://doi.org/10.1007/s10853-022-07204-w.
[44] Pirgazi H. On the alignment of 3D EBSD data collected by serial sectioning technique. Mater Charact 2019;152:223–9. https://doi.org/10.1016/j.matchar.2019.04.026.
[45] Pirgazi H. Wide Field 3D Orientation Contrast Microscopy. Doctoral dissertation, Ghent University, 2015.
[46] Polonsky AT, Echlin MP, Lenthe WC, Dehoff RR, Kirka MM, Pollock TM. Defects and 3D structural inhomogeneity in electron beam additively manufactured Inconel 718. Mater Charact 2018;143:171–81. https://doi.org/10.1016/j.matchar.2018.02.020.
[47] Echlin MP, Burnett TL, Polonsky AT, Pollock TM, Withers PJ. Serial sectioning in the SEM for three dimensional materials science. Curr Opin Solid State Mater Sci 2020;24. https://doi.org/10.1016/j.cossms.2020.100817.
[48] Schaffer M, Wagner J, Schaffer B, Schmied M, Mulders H. Automated three-dimensional X-ray analysis using a dual-beam FIB. Ultramicroscopy 2007;107:587–97. https://doi.org/10.1016/j.ultramic.2006.11.007.

[49] Zaefferer S, Konijnenberg P. Advanced analysis of 3D EBSD data obtained from FIB-EBSD tomography. Microscopy and Microanalysis 2012;18:520–1. https://doi.org/10.1017/S143192761200445X.
[50] Burnett TL, Kelley R, Winiarski B, Contreras L, Daly M, Gholinia A, et al. Large volume serial section tomography by Xe Plasma FIB dual beam microscopy. Ultramicroscopy 2016;161:119–29. https://doi.org/10.1016/j.ultramic.2015.11.001.
[51] Zhong X, Burke MG, Withers PJ, Zhang X, Zhou X, Burnett TL, et al. Multi-modal plasma focused ion beam serial section tomography of an organic paint coating. Ultramicroscopy 2019;197:1–10. https://doi.org/10.1016/j.ultramic.2018.10.003.
[52] Uchic MD, Holzer L, Inkson BJ, Principe EL, Munroe P. Three-Dimensional Microstructural Characterization Using Focused Ion Beam Tomography. MRS Bull 2007;32:408–16. https://doi.org/10.1557/mrs2007.64.
[53] Groeber M. A framework for automated analysis and simulation of 3D polycrystalline microstructures.Part 1: Statistical characterization. Acta Mater 2008;56:1257–73. https://doi.org/10.1016/j.actamat.2007.11.041.
[54] West Gd, Thomson Rc. Combined EBSD/EDS tomography in a dual-beam FIB/FEG–SEM. J Microsc 2009;233:442–50. https://doi.org/10.1111/j.1365-2818.2009.03138.x.
[55] Singh SS, Loza JJ, Merkle AP, Chawla N. Three dimensional microstructural characterization of nanoscale precipitates in AA7075-T651 by focused ion beam (FIB) tomography. Mater Charact 2016;118:102–11. https://doi.org/10.1016/j.matchar.2016.05.009.
[56] Nishikawa H, Furuya Y, Osada T, Kawagishi K, Hara T. Three-dimensional high-resolution crystallographic observation of the entire volume of microstructurally small fatigue cracks in Ni-Co based superalloy. Scr Mater 2023;222. https://doi.org/10.1016/j.scriptamat.2022.115026.
[57] Mangan Ma, Lauren Pd, Shiflet Gj. Three-dimensional reconstruction of Widmanstätten plates in Fe–12.3Mn–0.8C. J Microsc 1997;188:36–41. https://doi.org/10.1046/j.1365-2818.1997.2380799.x.
[58] Kral M V., Spanos G. Three-dimensional analysis and classification of grain-boundary-nucleated proeutectoid ferrite precipitates. Metallurgical and Materials Transactions A 2005;36:1199–207. https://doi.org/10.1007/s11661-005-0212-2.
[59] De Graef M, Kral M V., Hillert M. A modern 3-D view of an “old” pearlite colony. JOM 2006;58:25–8. https://doi.org/10.1007/BF02748491.
[60] Morito S, Pham AH, Hayashi T, Miyamoto G, Furuhara T. Three-dimensional Characterisation of Microstructures in Low-carbon Lath Martensite. ISIJ International 2022;62:1972–80. https://doi.org/10.2355/isijinternational.ISIJINT-2022-157.
[61] Morito S, Yoshida S, Hayamizu R, Hayashi T, Ohba T, Terasaki H, et al. Three-dimensional approach to observing growth of blocks and packets in Fe-18Ni maraging steel. Materials Science Forum, vol. 783–786, Trans Tech Publications Ltd; 2014, p. 916–9. https://doi.org/10.4028/www.scientific.net/msf.783-786.916.
[62] Morito S, Edamatsu Y, Ichinotani K, Ohba T, Hayashi T, Adachi Y, et al. Quantitative analysis of three-dimensional morphology of martensite packets and blocks in iron-carbon-manganese steels. J Alloys Compd 2013;577. https://doi.org/10.1016/j.jallcom.2012.02.004.

[63] Rowenhorst DJ, Gupta A, Feng CR, Spanos G. 3D Crystallographic and morphological analysis of coarse martensite: Combining EBSD and serial sectioning. Scr Mater 2006;55:11–6. https://doi.org/10.1016/j.scriptamat.2005.12.061.
[64] Shibata A, Gutierrez-Urrutia I, Nakamura A, Miyamoto G, Madi Y, Besson J, et al. Multi-scale three-dimensional analysis on local arrestability of intergranular crack in high-strength martensitic steel. Acta Mater 2022;234. https://doi.org/10.1016/j.actamat.2022.118053.
[65] Morsdorf L, Tasan CC, Ponge D, Raabe D. 3D structural and atomic-scale analysis of lath martensite: Effect of the transformation sequence. Acta Mater 2015;95:366–77. https://doi.org/10.1016/j.actamat.2015.05.023.
[66] Hata K, Fujiwara K, Kawano K, Sugiyama M, Fukuda T, Kakeshita T. Three-dimensional EBSD analysis and TEM observation for interface microstructure during reverse phase transformation in low carbon steels. ISIJ International 2018;58:742–50. https://doi.org/10.2355/isijinternational.ISIJINT-2017-639.
[67] Nagao A, Smith CD, Dadfarnia M, Sofronis P, Robertson IM. The role of hydrogen in hydrogen embrittlement fracture of lath martensitic steel. Acta Mater 2012;60:5182–9. https://doi.org/10.1016/j.actamat.2012.06.040.
[68] Deng Y, Liang Y, Zhao F, Xu F, Yang M, Long S. Influence of Microstructure on Tensile Properties and Fatigue Crack Propagation Behavior for Lath Martensitic Steel. Crystals (Basel) 2023;13:1392. https://doi.org/10.3390/cryst13091392.
[69] Zhang Y, Wang S, Xu G, Wang G, Zhao M. Effect of Microstructure on Fatigue-Crack Propagation of 18CrNiMo7-6 High-Strength Steel. Int J Fatigue 2022;163:107027. https://doi.org/10.1016/j.ijfatigue.2022.107027.
[70] Wang C, Qiu H, Kimura Y, Inoue T. Morphology, crystallography, and crack paths of tempered lath martensite in a medium-carbon low-alloy steel. Materials Science and Engineering: A 2016;669:48–57. https://doi.org/10.1016/j.msea.2016.05.041.
[71] Briffod F, Shiraiwa T, Enoki M. Modeling and crystal plasticity simulations of lath martensitic steel under fatigue loading. Mater Trans 2019;60:199–206. https://doi.org/10.2320/matertrans.ME201713.
[72] Shchyglo O, Du G, Engels JK, Steinbach I. Phase-field simulation of martensite microstructure in low-carbon steel. Acta Mater 2019;175:415–25. https://doi.org/10.1016/j.actamat.2019.06.036.
[73] Gallardo-Basile FJ, Naunheim Y, Roters F, Diehl M. Lath martensite microstructure modeling: A high-resolution crystal plasticity simulation study. Materials 2021;14:1–20. https://doi.org/10.3390/ma14030691.
[74] Xiang H, Van Paepegem W, Kestens LAI. Study of Microstructural Morphology of Ti-6Al-4V Alloy by Crystallographic Analysis and Phase Field Simulation. Materials 2022;15. https://doi.org/10.3390/ma15155325.
[75] Miyamoto G, Iwata N, Takayama N, Furuhara T. Quantitative analysis of variant selection in ausformed lath martensite. Acta Mater 2012;60:1139–48. https://doi.org/10.1016/j.actamat.2011.11.018.
[76] Liu W Bo, Song P Cheng, Zhang C, Yun D, Yao C fa, Yang Z gang. Crystallographic analysis of lath martensite in a 13Cr-5Ni steel by electron backscattering diffraction. Journal of Iron and Steel Research International 2018;25:213–20. https://doi.org/10.1007/s42243-018-0023-5.

[77] Sugiyama M, Takei M, Sekida S, Maruyama N. Characterization of hierarchical lath martensite microstructure in low carbon steels using ultra-high voltage TEM and SEM-EBSD analysis. IOP Conf Ser Mater Sci Eng 2022;1249:012020. https://doi.org/10.1088/1757-899x/1249/1/012020.
[78] Bobrowski P, Pedzich Z, Faryna M. Three-dimensional microstructural characterization of porous cubic zirconia. Micron 2015;78:73–8. https://doi.org/10.1016/j.micron.2015.07.004.
[79] Ram F, Lloyd JT, Rohrer GS. Habit planes of twins in a deformed Mg alloy determined from three-dimensional microstructure analysis. Mater Charact 2020;159:110014. https://doi.org/10.1016/j.matchar.2019.110014.
[80] Polonsky AT, Lang CA, Kvilekval KG, Latypov MI, Echlin MP, Manjunath BS, et al. Three-dimensional Analysis and Reconstruction of Additively Manufactured Materials in the Cloud-Based BisQue Infrastructure. Integr Mater Manuf Innov 2019;8:37–51. https://doi.org/10.1007/s40192-019-00126-7.
[81] Burdet P, Vannod J, Hessler-Wyser A, Rappaz M, Cantoni M. Three-dimensional chemical analysis of laser-welded NiTi–stainless steel wires using a dual-beam FIB. Acta Mater 2013;61:3090–8. https://doi.org/10.1016/j.actamat.2013.01.069.
[82] McDonald SA, Reischig P, Holzner C, Lauridsen EM, Withers PJ, Merkle AP, et al. Non-destructive mapping of grain orientations in 3D by laboratory X-ray microscopy. Sci Rep 2015;5:14665. https://doi.org/10.1038/srep14665.
[83] Zhao Y, Niverty S, Ma X, Liu X, Chawla N. 3D grain structure of an extruded 6061 Al alloy by lab-scale X-ray diffraction contrast tomography (DCT). Mater Charact 2020;170:110716. https://doi.org/10.1016/j.matchar.2020.110716.
[84] McDonald SA, Burnett TL, Donoghue J, Gueninchault N, Bale H, Holzner C, et al. Tracking polycrystal evolution non-destructively in 3D by laboratory X-ray diffraction contrast tomography. Mater Charact 2021;172:110814. https://doi.org/10.1016/j.matchar.2020.110814.
[85] Kobayashi M, Zhang Y, Ishikawa H, Sun J, Oddershede J, Jensen DJ, et al. Relationships between 3D grain structure and local inhomogeneous deformation: A laboratory-based multimodal X-ray tomography investigation. Acta Mater 2022;240:118357. https://doi.org/10.1016/j.actamat.2022.118357.
[86] Ghafoori-Ahangar R, Verreman Y. Fatigue behavior of load-carrying cruciform joints with partial penetration fillet welds under three-point bending. Eng Fract Mech 2019;215:211–23. https://doi.org/10.1016/j.engfracmech.2019.05.015.
[87] Sabourin M, Thibault D, Bouffard DA, Lévesque M. New parameters influencing hydraulic runner lifetime. IOP Conf Ser Earth Environ Sci 2010;12:012050. https://doi.org/10.1088/1755-1315/12/1/012050.

Chapter 2

New insights into the morphology and crystallography of lath martensite using 3D EBSD characterization of a low-carbon stainless steel

New insights into the morphology and crystallography of lath martensite using 3D EBSD characterization of a low-carbon stainless steel

Mehdi Mosayebi[1,4], Daniel Paquet[2], Pierre-Antony Deschênes[2,3], Laurent Tôn-Thât[2], Nabil Bassim[1,4,*]

[1] Department of Materials Science and Engineering, McMaster University, Hamilton, ON, Canada.
[2] Hydro Quebec Research Institute (IREQ), Varennes, QC, Canada.
[3] Department of Mechanical Engineering, École de technologie supérieure, Montreal, QC, Canada.
[4] Canadian Centre for Electron Microscopy, McMaster University, Hamilton, ON, Canada.

Abstract

This study presents a comprehensive characterization of lath martensite morphology in a low-carbon as-cast 13Cr-4Ni stainless steel. Two-dimensional (2D) analyses using energy-dispersive spectroscopy (EDS) and electron backscatter diffraction (EBSD) revealed a predominantly lath martensitic matrix interspersed with delta-ferrite particles and non-metallic inclusions. Expanding to three dimensions (3D), large-volume Xe plasma focused ion beam (PFIB) serial sectioning tomography and EBSD were employed to reconstruct and analyze the microstructure. Using 3D-EBSD results, the martensitic matrix was segmented into prior austenite grains (PAGs), packets, blocks, and sub-blocks, enabling 3D statistical analysis of these structural units. Heterogeneities such as delta-ferrite particles, inclusions, and micropores were reconstructed using a multimodal 3D imaging approach, revealing their distinct spatial distributions and morphological characteristics. Two delta-ferrite morphologies were identified: (i) elongated particles with faceted interfaces located at PAG boundaries, and (ii) smaller, spherical particles distributed within PAG interiors. The 3D networks of sub-block, block, packet, and PAG boundaries were identified, quantified, and classified, using the well-established Kurdjumov-Sachs (K-S) orientation relationship (OR) and its associated intervariant misorientations, providing deeper insights into the crystallography and morphology of internal boundaries. Additionally, 3D morphological analysis of martensitic blocks and packets revealed three primary interaction types: hard impingement of blocks from two distinct packets, mutual intersection of blocks from two distinct packets, and interpenetration of sub-blocks/blocks within a single packet. These interactions contributed to the formation of an interlocked martensitic microstructure characterized by inhomogeneous boundary networks exhibiting complex morphological and crystallographic features. These new insights highlight the advantages of advanced 3D techniques in enabling a thorough characterization of microstructural intricacies, offering a robust foundation for developing predictive models that link microstructure to the mechanical performance of these alloys.

Keywords: 3D electron backscatter diffraction (3D EBSD), focused ion beam (FIB), martensitic steels, 3D defect characterization, 3D boundary network

2.1 Introduction

Ferrous martensite exhibits a diverse array of morphologies influenced primarily by composition, particularly carbon content. These morphologies include lath, butterfly, lenticular, and thin plate structures [1-3]. Among these, lath martensite, which forms in low-carbon steels (0.01-0.3 wt.%C), holds significant industrial importance due to its remarkable combination of high strength, toughness, and weldability [4-5]. This morphology is closely associated with the Kurdjumov-Sachs orientation relationship (OR) [1,6,7], wherein a prior austenite grain is subdivided into a three-level hierarchy during the martensitic phase transformation: packet, block, and lath. Specifically, a single γ-phase crystal can evolve into 24 crystallographically distinct variants (V1-V24), dictated by the symmetry of cubic system. These variants are grouped into four distinct crystallographic packets, as γ contains four close-packed (CP) {111} planes, with six variants corresponding to each {111} plane (as summarized in Table 2.1). Within a given packet, the variants share the same habit plane and are organized into variant pairs to form blocks, which are further subdivided into low-misorientation sub-blocks [1,8].

The intricate interplay between this hierarchical morphology and the diverse K-S OR variants, creates an abundance of internal boundaries (i.e., intervariant boundaries) with varying misorientations and morphologies. Unlike diffusional transformations, such as ferrite formation, the boundary network in lath martensite emerges from the constraints imposed by the martensitic shear transformation, leading to highly intricate boundary morphologies [2,9-11]. This network, governed largely by crystallographic relationships [12,13], plays a pivotal role in dictating the extent of microstructural refinement and, consequently, the mechanical behavior of the material. Numerous studies [14,17] have demonstrated that both block and sub-block boundaries follow a

Hall-Petch like relationship, acting as effective barriers to dislocation motion and thereby contributing to the enhanced strength of lath martensitic steels. Furthermore, the morphology and misorientation characteristics of high-angle boundaries, such as block, packet, and PAG boundaries, have been shown to significantly influence the material's susceptibility to hydrogen embrittlement [9,18] and its fatigue crack behavior [19-22], particularly by affecting the tortuosity of crack paths. However, the degree of these property changes or enhancements is strongly influenced by the characteristics of the boundary network, including the population, spatial distribution, and connectivity of the boundaries [2,21,23-26].

In addition to the hierarchical martensitic matrix, various heterogeneities, including retained austenite, delta-ferrite, non-metallic inclusions, and casting defects can significantly influence the properties of lath martensitic steels [14,27-29]. Among these, delta-ferrite and inclusions, commonly observed in such steels, can act as stress concentrators or influence the nucleation and growth of martensitic structures, thereby impacting the overall microstructural evolution. The size, distribution, and morphology of these heterogeneities play a crucial role in determining the mechanical performance of the material, as evidenced by numerous experimental studies [29-33]. This effect is particularly pronounced in cast martensitic stainless steels, where casting defects and secondary phases are frequently identified as crack initiation sites, adversely impacting ductility, fatigue performance, and fracture resistance [34-36].

Due to the critical role of this complex microstructure in determining the material's mechanical properties, lath martensite has been the subject of extensive research. Most of these studies have conventionally relied on two-dimensional (2D) imaging techniques, such as optical microscopy, transmission electron microscopy (TEM), scanning electron microscopy (SEM), and electron

backscatter diffraction (EBSD) [6,37-39]. While these 2D techniques have provided valuable insights into the microstructure of martensitic steels, they inherently fall short of capturing the full three-dimensional (3D) complexity of the microstructure. In particular, they lack the capability to resolve the spatial distribution, intricate connectivity, and interactions of microstructural features and their interfaces. As a result, these limitations hinder a deeper understanding of the mechanisms governing the mechanical behavior of these complex materials.

Recently, advancements in focused ion beam (FIB) serial sectioning tomography have revolutionized our ability to investigate highly intricated microstructures. This technique enables the sequential removal of ultra-thin material layers, sometimes as fine as tens of nanometers [40-44], allowing for high-resolution three-dimensional (3D) characterization. When combined with advanced analytical methods such as energy-dispersive spectroscopy (EDS) and electron backscatter diffraction (EBSD), FIB tomography facilitates the simultaneous acquisition of compositional, morphological, and crystallographic data from each layer, enabling precise 3D reconstructions [45-53]. These capabilities provide insights into microstructural characteristics that cannot be fully captured through conventional 2D characterizations. For instance, 3D SEM/EBSD analyses have been instrumental in uncovering intricate grain boundary networks in ferritic and austenitic steels [25,54-56], mapping phase connectivity in dual-phase steels [57-59], and characterizing the distribution of secondary phases and defects in various alloys [60-63]. In lath martensitic steels, Morito et al. [8,64-66] combined EBSD with serial sectioning to examine the morphology of lath martensite in low-carbon steels, while Rowenhorst et al. [67] used this approach to investigate the 3D morphology of coarse martensite crystals in commercial HSLA-100 steel. Similarly, serial sectioning has been applied to Widmanstätten [49,71,72], bainitic [70], and ferritic [71] structures, revealing intricate plate intersections. Few other studies [21,27,72],

have utilized FIB tomography to analyze the morphology and crystallography of single laths, block boundaries, and sub-block boundaries at higher resolutions. Despite significant progress, most previous studies have primarily focused on small to mid-sized structural units, leaving gaps in understanding the larger-scale architecture of lath martensite, an aspect critical for accurate virtual mechanical testing and digital twin development of these steels. Moreover, a comprehensive 3D analysis of the interfaces developed during the austenite-to-martensite transformation remains largely unexplored in the literature. Addressing this gap is essential for understanding the hierarchical structure and boundary networks that govern the mechanical properties and transformation behavior of lath martensitic steels.

Accordingly, the present study aims to achieve a comprehensive 3D characterization of lath martensite through large-volume serial sectioning tomography, utilizing a combination of Xe plasma FIB (PFIB) tomography and EBSD techniques. This advanced approach enables the systematic characterization, quantification, and classification of the morphological and crystallographic features of lath martensite and their associated interfaces in 3D. Furthermore, this study highlights the potential of simultaneous data acquisition from both EBSD and SEM, facilitating correlated 3D reconstruction of critical microstructural components, including delta-ferrite particles, non-metallic inclusions, and casting defects, allowing for a detailed investigation of their morphologies, spatial distributions, and interactions within the martensitic matrix.

Table 2.1: The 24 possible variants formed through the martensitic phase transformation under the K-S orientation relationship. The distribution of the 16 independent K-S intervariant misorientations is expressed as area fractions (%), determined through the 3D-EBSD analysis.

Variant	Plane parallel	Direction parallel	Rotation angle/axis from V1	Percentage of the 16 unique intervarian boundaries calculated using 3D EBSD
V1	$(111)_\gamma \parallel (011)_\alpha$	$[-101]_\gamma \parallel [-1-11]_\alpha$	-	-
V2		$[-101]_\gamma \parallel [-11-1]_\alpha$	60°/[11-1]	12.1
V3		$[01-1]_\gamma \parallel [-1-11]_\alpha$	60°/[011]	14.7
V4		$[01-1]_\gamma \parallel [-11-1]_\alpha$	10.53°/[0-1-1]	3.9
V5		$[1-10]_\gamma \parallel [-1-11]_\alpha$	60°/[0-1-1]	-
V6		$[1-10]_\gamma \parallel [-11-1]_\alpha$	49.47°/[011]	6.1
V7	$(1-11)_\gamma \parallel (011)_\alpha$	$[10-1]_\gamma \parallel [-1-11]_\alpha$	49.47°/[-1-11]	1.6
V8		$[10-1]_\gamma \parallel [-11-1]_\alpha$	10.53°/[11-1]	4.1
V9		$[-1-10]_\gamma \parallel [-1-11]_\alpha$	50.51°/[-10 3 -13]	2.2
V10		$[-1-10]_\gamma \parallel [-11-1]_\alpha$	50.51°/[-7 -55]	2.7
V11		$[011]_\gamma \parallel [-1-11]_\alpha$	14.88°/[13 5 1]	6.2
V12		$[011]_\gamma \parallel [-11-1]_\alpha$	57.21°/[-356]	5.4
V13	$(-111)_\gamma \parallel (011)_\alpha$	$[0-11]_\gamma \parallel [-1-11]_\alpha$	14.88°/[5 -13 -1]	-
V14		$[0-11]_\gamma \parallel [-11-1]_\alpha$	50.51°/[-55-7]	-
V15		$[-10-1]_\gamma \parallel [-1-11]_\alpha$	57.21°/[-6-25]	0.9
V16		$[-10-1]_\gamma \parallel [-1-11]_\alpha$	20.61°/[11-11 -6]	0.7
V17		$[110]_\gamma \parallel [-1-11]_\alpha$	51.73°/[-11 6 -11]	2.3
V18		$[110]_\gamma \parallel [-11-1]_\alpha$	47.11°/[-24 -10 21]	1.7
V19	$(11-1)_\gamma \parallel (011)_\alpha$	$[-110]_\gamma \parallel [-1-11]_\alpha$	50.51°/[-3 13 10]	-
V20		$[-110]_\gamma \parallel [-11-1]_\alpha$	57.21°/[36-5]	-
V21		$[0-1-1]_\gamma \parallel [-1-11]_\alpha$	20.61°/[30-1]	1.1
V22		$[0-1-1]_\gamma \parallel [-11-1]_\alpha$	47.11°/[-10 21 24]	-
V23		$[101]_\gamma \parallel [-1-11]_\alpha$	57.21°/[-2-5-6]	-
V24		$[101]_\gamma \parallel [-11-1]_\alpha$	21.06°/[9-40]	0.9

2.2 Material and methods

The material used in this study is the CA6NM alloy [28,73], a low-carbon as-cast martensitic stainless-steel with an average PAG size of 158.1 μm (Figure 2.1(a)), widely utilized in the hydroelectric industry. The chemical composition of this steel is provided in Table 2.2. A volume of roughly 140 × 140 × 90 μm^3 (X, Y, Z) was lifted out from a 10 mm × 10 mm × 4 mm specimen (Figure 2.2(a)) for serial sectioning using a dual-beam TFS Helios G5 Xe PFIB system equipped with an Oxford Symmetry EBSD detector. All stage movements, serial sectioning, mapping, and communications were controlled by the Auto-slice-and-view software under the following conditions.

The slice thickness was set to 250 nm and EBSD were collected every two slices, resulting in a final Z-resolution of 500 nm. A current of 0.2 μA was used for slicing the block, and a 5° rocking mill was employed to minimize curtaining effects. For EBSD mapping, the SEM was operated at 20 kV and 13 nA, with the EBSD camera chip set to a 4 × 4 binning configuration, maintaining an indexing rate above 90%. Each EBSD map covered the entire sample face with indexing at 500 nm step size in order to provide cubic voxels for the 3D reconstruction. A total of 200 individual slices were collected on a sequence of X-Y planes. Although this resolution does not resolve individual martensitic laths, larger microstructural units such as sub-blocks, blocks, packets, and prior austenite grains (PAGs) were readily identifiable within the dataset. The total time per slice, including PFIB milling, SEM imaging, EBSD mapping and stage movements, was ~30 min, resulting in a total collection time of ~4 days.

Processing of the EBSD maps to generate a coherent 3D representation of the microstructure was conducted using the open-source software DREAM.3D [74], with the final visualizations

created in ParaView 5.9.1 [75]. Misorientation tolerances and other key reconstruction parameters were optimized iteratively to preserve the integrity of the original data while ensuring an accurate representation of the microstructure. Throughout the process, the reconstructed volume was analyzed from multiple orthogonal perspectives to manually verify that the applied filters accurately represented the 3D microstructure. Leveraging insights from previous studies on 3D-EBSD reconstruction of complex microstructures—including martensitic, bainitic, and additively manufactured materials [44,51,53,76-78]—the primary processing steps were implemented using the various built-in filters available in DREAM.3D. These steps included raw data importation, thresholding, alignment, clean-up, segmentation, and grain boundary meshing, as detailed below:

Initially, the stack of 2D EBSD maps, stored as a series of .ctf files, was converted into HDF5 format to enable analysis in DREAM.3D. Thresholding was then applied to create a binary mask, separating "good" data from "bad" data for subsequent reconstruction and analysis. Band contrast (BC) and Error metrics (a binary value set to 0 for successfully indexed points and 3 for unindexed points [44]) served as the criteria for thresholding. Voxels flagged as "bad" through these metrics, being unindexed and lacking orientation data, were masked out. However, these masked voxels were later utilized for identifying defects, such as pores and non-metallic inclusions, during the segmentation process, as elaborated in Section 3.3 of the paper.

Following the thresholding step, individual EBSD maps were aligned using a misorientation tolerance of 1°, ensuring alignment by minimizing the misorientation between adjacent pixels in the Z direction. The aligned 3D volume was subsequently cropped into a neat rectangular prism with 140 × 130 × 85 μm^3 dimensions (Figure 2.2(b)), to create smooth edges, facilitating visual inspection and preventing erroneous behavior during the clean-up and segmentation steps.

Next, four primary clean-up steps were conducted. First, a filter was applied to convert bad voxels into good voxels if they shared the same orientation as at least four of their neighbors within a 5° tolerance. Subsequently, another filter was used to fill bad data points with data from their most reliable neighbor, based on a minimum confidence index of 0.2 and a misorientation tolerance of 5°. The third filter removed features with fewer than two neighbors or lacking minimum feature size of 64 voxels. This corresponds to 4 × 4 × 4 voxels across a feature and an equivalent diameter of ~2.5 μm (approximately five times larger than the EBSD and serial sectioning resolutions of 0.5 μm), eliminating small artifacts generated during earlier clean-up processes. The remaining features were then isotropically coarsened to fill gaps left by removed small features, ensuring that only grains sufficiently large relative to the data resolution were characterized. Finally, a fourth clean-up filter was employed to remove small noise in the data while preserving larger contiguous regions that might represent features, such as pores or defects. This filter eroded the "bad cells" until none remained, but contiguous clusters of "bad cells" exceeding the minimum defect size of 64 voxels were retained. Since these clean-up steps had the potential to erroneously alter or remove unindexed/bad voxels associated with defects and inclusions, comparisons were made between the processed EBSD maps (primarily the inverse pole figures (IPF) and BC maps) and the corresponding secondary electron (SE) images and forward scatter diode (FSD) maps. This was done to ensure that these features were accurately represented, considering both their spatial locations and morphological characteristics in the processed 3D volume.

Following the thresholding and clean-up processes, a misorientation-based segmentation approach was employed to separate microstructural features, such as sub-blocks, blocks, and ferrite particles, by grouping neighboring voxels into the same feature. For conventional microstructures, such as

those with equiaxed or recrystallized grains, 3D segmentation is relatively straightforward, as grains typically exhibit well-defined high-angle grain boundaries and minimal internal misorientation variations. In such cases, segmentation can be performed by grouping neighboring face-sharing voxels with mutual misorientation angles below a critical threshold, commonly set at 5° [44,53,79]. For the present martensitic microstructure, however, a stricter misorientation threshold of 1° was necessary, owing to its hierarchical morphology and diverse orientation relationships (OR). This choice was also guided by the angular resolution limits introduced by the EBSD acquisition conditions. Specifically, a 4 × 4 binning configuration was employed on the EBSD detector to maintain high indexing rates across the large-scanned volume. While this binning improves signal-to-noise ratio and acquisition efficiency, it reduces the effective angular resolution to approximately 1°, as it broadens the Kikuchi bands and limits the precision of orientation determination. As a result, orientation differences below 1° fall within the noise level and cannot be reliably distinguished. Accordingly, a 1° disorientation tolerance was selected as the lowest practical threshold to avoid over-segmentation and ensure that only crystallographically meaningful boundaries were preserved. The effectiveness of this threshold was validated through systematic trial-and-error adjustments during the segmentation process, as detailed in Section 2.3.2. The same threshold was subsequently applied across all analyses, including size measurements, morphological assessments, PAG/packet reconstructions, and boundary network characterizations. Additionally, this segmentation process assigned unique feature IDs to the masked-out “bad/unindexed” voxels, facilitating subsequent defect analysis in later stages.

Once the 3D orientation data reconstruction was completed and all the features were assigned unique feature IDs, a variety of statistical parameters, including size, volume fraction, aspect ratio and sphericity, were calculated to characterize the microstructure. Internal misorientation gradients within the features were analyzed using 3D kernel averaging (with a kernel volume of 2 × 2 × 2 μm^3) to aid in identifying delta-ferrite particles within the martensitic matrix (as detailed in Section 3.3). To further analyze the internal boundaries, a triangular mesh of the boundary surfaces was generated using the Quick Surface Mesh filter in DREAM.3D. Due to the terrace-step geometry introduced by cube-shaped voxels, the boundary meshes were smoothed using a Laplacian smoothing algorithm in DREAM.3D, employing 100 iterations with a weighting factor of 0.05. Each triangle in the resulting mesh provided detailed information about the orientations of the features on either side, the disorientation across the triangle, the centroid coordinates, the triangle area, and the normal vector. These data facilitated the computation and 3D mapping of internal boundaries based on their area sizes, local curvature, and crystallographic characteristics. Additionally, using this boundary information and the Brandon criterion [80], coincidence site lattice (CSL) boundaries were identified within the 3D dataset. PAG identification and variant analysis were conducted using a MATLAB-based code with the help of MTEX toolbox [44,81].

Table 2.2: Chemical composition of the CA6NM steel used in the current study (wt.%).

C	Cr	Ni	Mo	Mn	Si	P	S	Fe
0.02	12.1	3.57	0.55	0.52	0.26	0.034	0.005	Bal.

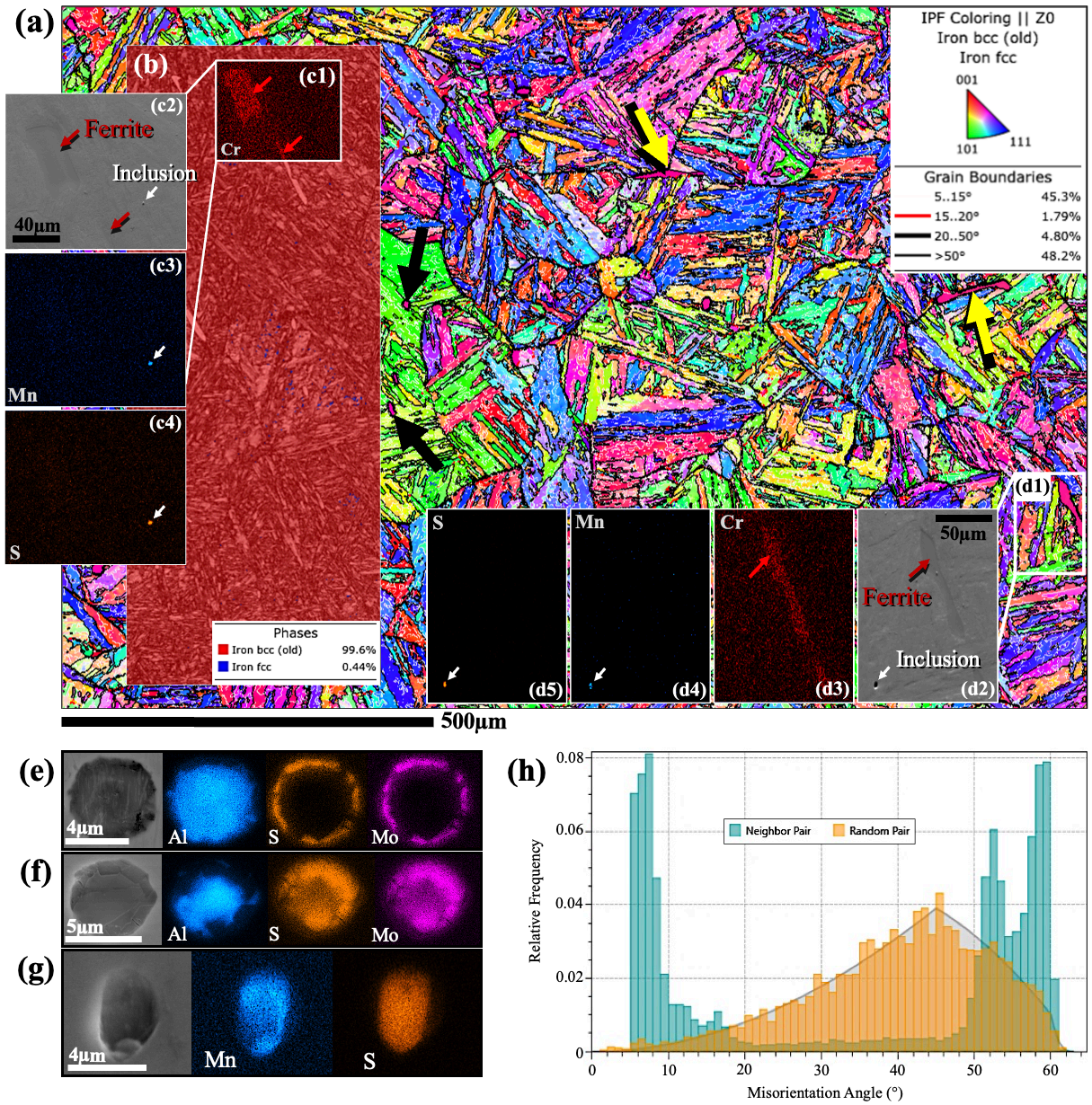

Figure 2.1: (a) A large-area 2D IPF-Z map of the martensitic microstructure with an overlaid boundary map representing misorientation angle (θ) ranges of 5°≤θ<15° (white lines), 15°≤θ<20° (red lines), 20°≤θ≤50° (thick black lines), and θ>50° (thin black lines). **(b)** Corresponding phase map superimposed on the IPF map in (a), illustrating the distribution of BCC (red) and FCC (blue) phases in a selected area of the microstructure. **(c1-c4)** and **(d1-d5)** SEM and EDS maps of the selected areas highlighted by white boxes in (c1) and (d1), respectively. **(e-g)** High-magnification SEM and EDS maps illustrating three different inclusions within the microstructure. **(h)** Misorientation angle distribution of the microstructure, extracted from the orientation map in (a). (White, yellow, and black arrows indicate examples of non-metallic inclusions, ferrite particles at prior austenite grain boundaries, and ferrite particles within prior austenite grains, respectively).

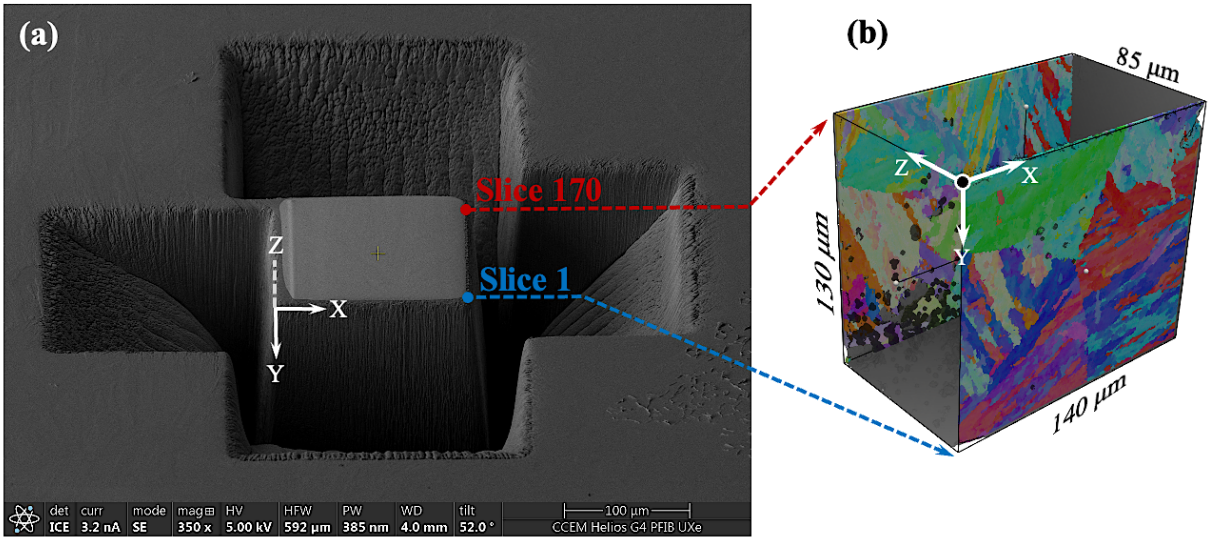

Figure 2.2: (a) SEM overview of the analyzed volume (~ 140 × 140 × 100 µm^3) isolated for the lift-out process and subsequent serial-sectioning and imaging. **(b)** 3D reconstruction of the microstructure, cropped into a rectangular prism of ~ 140 × 130 × 85 µm^3. The approximate positions of the first and the last EBSD scans are indicated in both (a) and (b). The X-Y plane represents the EBSD imaging plane, while the Z-axis corresponds to the slicing direction. (IPF maps in (b) are color-coded based on IPF-Z, while Z//slicing direction).

2.3 Results and discussion

2.3.1 General characteristics of 2D microstructure

Figure 2.1 provides a comprehensive overview of the crystallographic and compositional features of the microstructure. The phase and energy-dispersive spectroscopy (EDS) maps, overlaid on the EBSD orientation map in Figure 2.1(a)**,** reveal a predominantly lath martensitic matrix interspersed with delta-ferrite particles and non-metallic inclusions. Delta-ferrite particles, enriched in chromium (Figures 2.1(c1, d3)), constitute 1.3% of the microstructure. These particles display a mean aspect ratio of 3.4±2.8 (Min=1.2, Max=13.5) and average equivalent diameter of 22.8±14.4 µm (Min=6.2 µm, Max=66.7 µm), indicating a wide size distribution. The ferrite crystals not only mark the former austenite grain boundaries, but also extend into the interior of the grains, as indicated by the yellow and black arrows, respectively, in Figure 2.1(a). The presence

of delta-ferrite is a well-documented characteristic of cast martensitic stainless steels and is attributed to the segregation of ferrite-promoting elements during solidification, which stabilizes the ferrite phase at room temperature [29,32]. Additionally, non-metallic inclusions enriched in manganese (Mn), sulfur (S), aluminum (Al), and molybdenum (Mo) were identified within the microstructure.(Figures 2.1(e-g)). These inclusions, with an average diameter of 4.6±1.1 μm, are sparsely distributed and predominantly spherical in morphology.

The boundary map superimposed on the EBSD orientation map in Figure 2.1(a) further highlights the hierarchical characteristic of the lath martensitic structure. Given the steel's low carbon content (0.02 wt%), the Kurdjumov-Sachs (K-S) orientation relationship (OR) was assumed to govern the austenite-to-martensite phase transformation [1,82]. In this IPF map, the distinctly colored regions represent aligned crystallographic orientations (i.e., blocks), which are delineated by sharp transitions forming high-angle boundaries, represented as thin black lines in Figure 2.1(a). Within these blocks, gradual orientation changes signify the presence of low-angle boundaries, marked as white lines in Figure 2.1(a), which further subdivide the microstructure into finer sub-blocks.

This hierarchical boundary structure is quantitatively illustrated by the misorientation angle distribution in Figure 2.1(h), exhibiting a bimodal pattern with two pronounced peaks in the ~5-20° and ~45–60° ranges. This bimodal misorientation distribution is consistent with previous studies [9,13] and reflects the theoretical misorientation angles predicted by the K–S OR theory (Table 1). The 24 K-S variants formed within a single austenite grain yield 23 intervariant misorientations, reduced to 16 misorientations due to crystal symmetry (e.g., V1-V3 and V1-V5 being identical) [2]. As detailed in Table 2.1, these 16 misorientations cluster into two distinct ranges, forming the observed bimodal pattern. Consequently, each individual parent austenite

grain can be partitioned by these 16 specific boundaries, which can serve as a basis for identifying microstructural constituents such as packets and blocks. It is noteworthy that misorientation angles in the ~20-45° range are absent among the intervariant misorientations derived from the K–S OR. Instead, these angles are associated with prior austenite grain boundaries (PAGBs) or non-K–S boundaries [13], as depicted by thick black lines in Figure 2.1(a). These 2D analyses highlight the significance of crystallographic analysis and the relevance of the K-S OR in unraveling the intricate interplay between crystallographic orientations and hierarchical morphology of the material.

2.3.2 Overview of the 3D PFIB volume and segmentation of the crystallographic features

The morphological characteristics of the microstructure were further examined using the 3D volume obtained from PFIB-EBSD analysis (Figures 2.2 and 2.3). To accurately delineate individual crystallographic features, such as sub-blocks and blocks, the segmentation of the 3D microstructure was systematically refined by varying the misorientation tolerance between 1° and 5°. Figures 2.3(a1–a3) and Figures 2.3(b1–b3) illustrate feature ID maps and their corresponding misorientation angle distributions obtained from 3D segmentations using misorientation tolerances of 5°, 2°, and 1°, respectively. Increasing the misorientation tolerance to 2° and 5° led to excessive merging of features, particularly affecting the accurate identification of microstructural units defined by low-angle boundaries (LABs, 5°–15°), as shown in Figures 2.3(b1, b2). This over-merging resulted in a loss of resolution in distinguishing sub-block and block boundaries, leading to feature volumes that no longer aligned with the expected hierarchical morphology of lath martensite. In contrast, segmentation at 1° preserved the distinct crystallographic features with minimal over-merging, yielding a misorientation angle distribution (Figure 2.3(b3)) that closely matched the characteristic bimodal pattern of K-S OR intervariant boundaries, exhibiting two

distinct peaks in the ~5°–20° and ~45°–60° ranges. Applying this threshold across the dataset enabled accurate feature identification, with ~45,000 individual features exhibiting volumes ranging from 8.3 μm^3 to 68.1 × 10^3 μm^3 (Figure 2.3(c2)) and an average aspect ratio of 4.8±3.3 (Figure 2.3(c3)), reflecting the substantial size variability and elongated morphology of lath martensite structures. Building upon this segmentation, Figure 2.4 provides a detailed 3D reconstruction of prior austenite grains (PAGs) and their boundaries, outlining the spatial extent of the original austenitic grains (Figure 2.4(a2)). Despite the considerable volume analyzed, all three PAGs appear truncated (Figures 2.4(b1-b3)), with only portions present within the reconstructed dataset, emphasizing the coarse-grained nature of the material. Statistical analyses of these PAGs revealed average block and sub-block thicknesses of 19.1±8.8 μm and 8.6±2.9 μm, respectively (Figures 2.4(b1-b3)). These results highlight the hierarchical structure of the microstructure and emphasize the critical role of the segmentation approach in capturing its intricate architectural details.

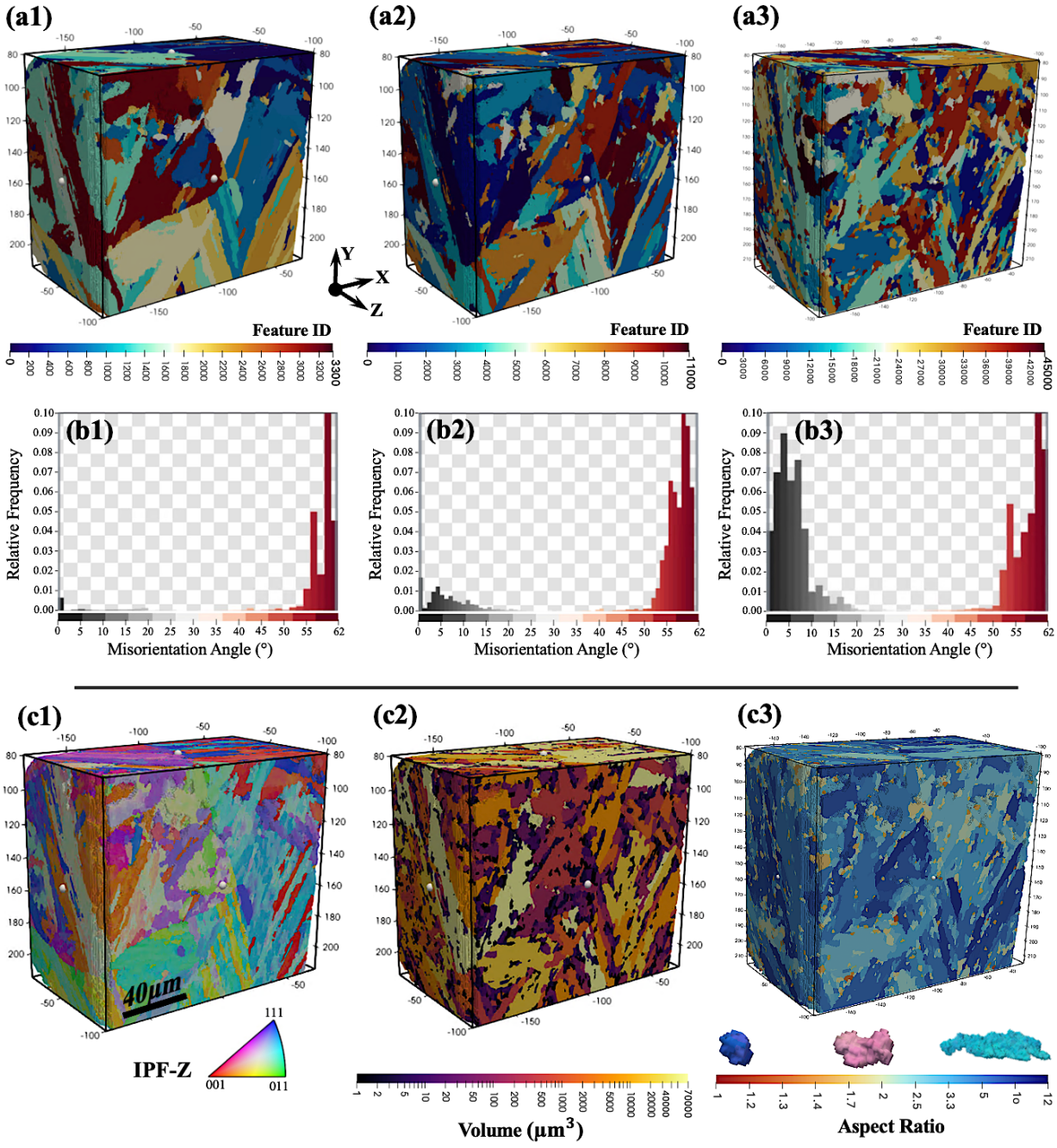

Figure 2.3: (a1-a3) 3D reconstruction and segmentation of the microstructure using misorientation tolerances of 5°, 2°, and 1°, presented as feature ID maps. **(b1-b3)** Misorientation angle distributions of internal boundaries corresponding to the volumes shown in **(a1-a3)**, respectively. **(c1-c3)** 3D rendering of the microstructure segmented at 1° (as shown in (a3)), with segmented features color-coded by IPF-Z (c1), volume (c2), and aspect ratio (c3). Representative examples of segmented features with varying aspect ratios are depicted in the legend of (c3).

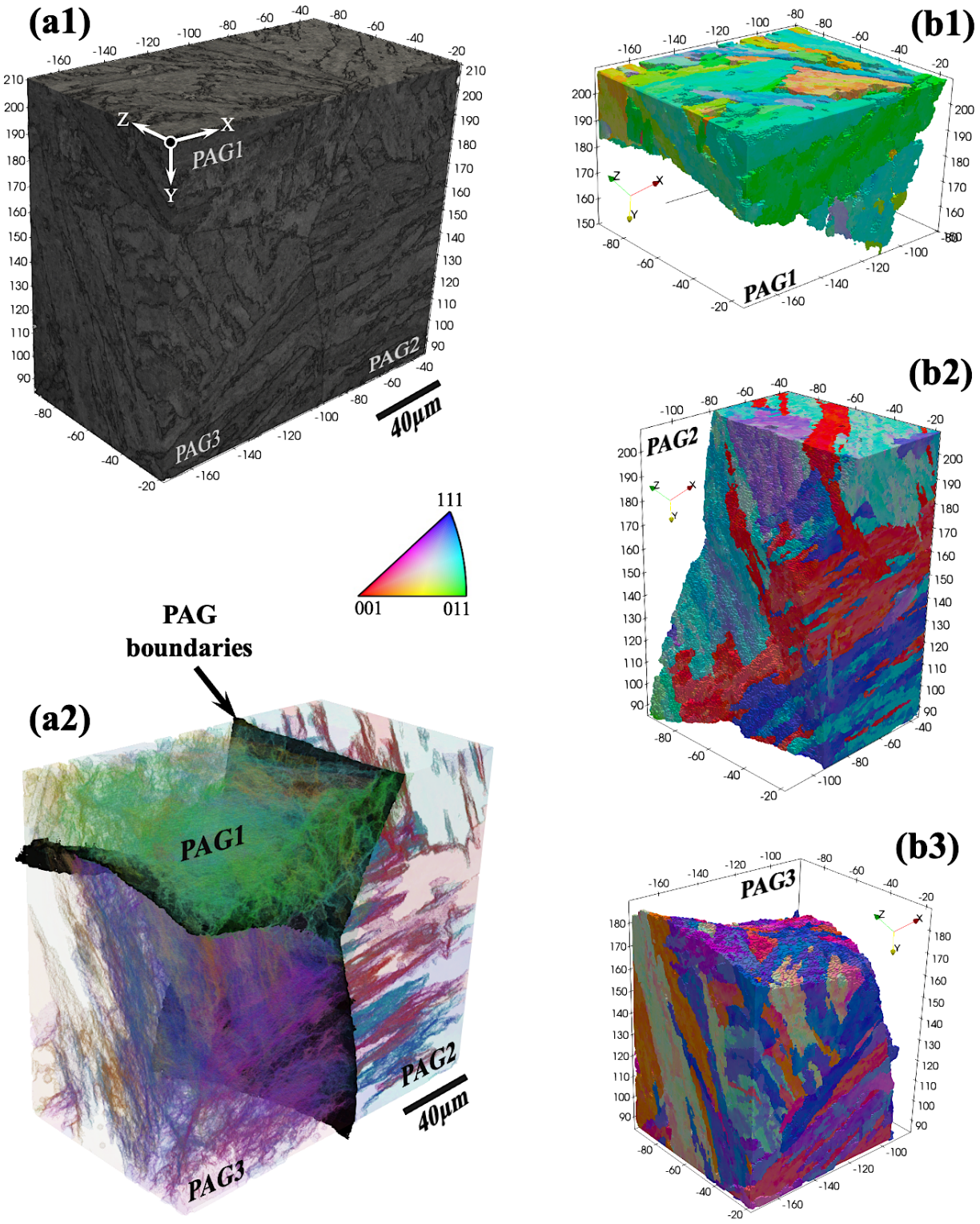

Figure 2.4: (a1-a2) 3D band contrast (BC) and IPF-Z maps of the microstructure segmented with a 1.2° misorientation tolerance. **(b1-b3)** 3D reconstruction of prior austenite grains (PAG1–PAG3) in the form of IPF-Z maps. PAG boundaries (PAGBs) are highlighted in black in (a2), illustrating the spatial extent of the reconstructed grains.

2.3.3 3D segmentation of micropores, inclusions, and delta-ferrite particles

Micropores and inclusions were initially identified using a combination of misorientation-based (i.e., by analyzing non-indexed/bad pixels from the EBSD orientation maps) and contrast-based (i.e., by leveraging contrast variations in SE, FSD, and BC maps) methods. To pinpoint the spatial positions of these features, 25 individual slices, each with intervals of 3 μm and containing SE, FSD, BC, and IPF maps, were selected as reference points. Figure 2.5 illustrate the progressive detection of micropores and inclusions across four representative layers of the 3D structure. Once the features were identified and located within the microstructure, their 3D segmentation was performed by grouping the non-indexed/bad voxels, allowing for the reconstruction of individual features that accurately represent the true morphology and 3D shape of the pores and inclusions. This was achieved through the optimized parameters determined during the thresholding, clean-up, and segmentation steps, as also outlined earlier in Section 2. In total 15 micropores and 9 inclusions were identified within the analyzed volume, corresponding to volume fractions of 0.3% and 0.03%, respectively.

These microstructural features can generally be distinguished and classified based on their sphericity and size. The sphericity factor (Ψ), which is a measure of shape, is defined as the ratio of the surface area of a sphere with the same volume as the feature to the actual surface area of the feature [83,84]. A Ψ value closer to 1 indicates a shape that is closer to a perfect sphere, and it is expressed as follows:

$$\Psi = \frac{\pi^{1/3}.(6V)^{2/3}}{A} \tag{2.1}$$

where V represents the volume and A represents the surface area. The sizes of the features were quantified using the equivalent diameter (ED), defined as the diameter of a sphere with the same volume as the feature, and calculated using the following equation [83,54]:

$$ED=\sqrt[3]{\frac{6V}{\pi}} \tag{2.2}$$

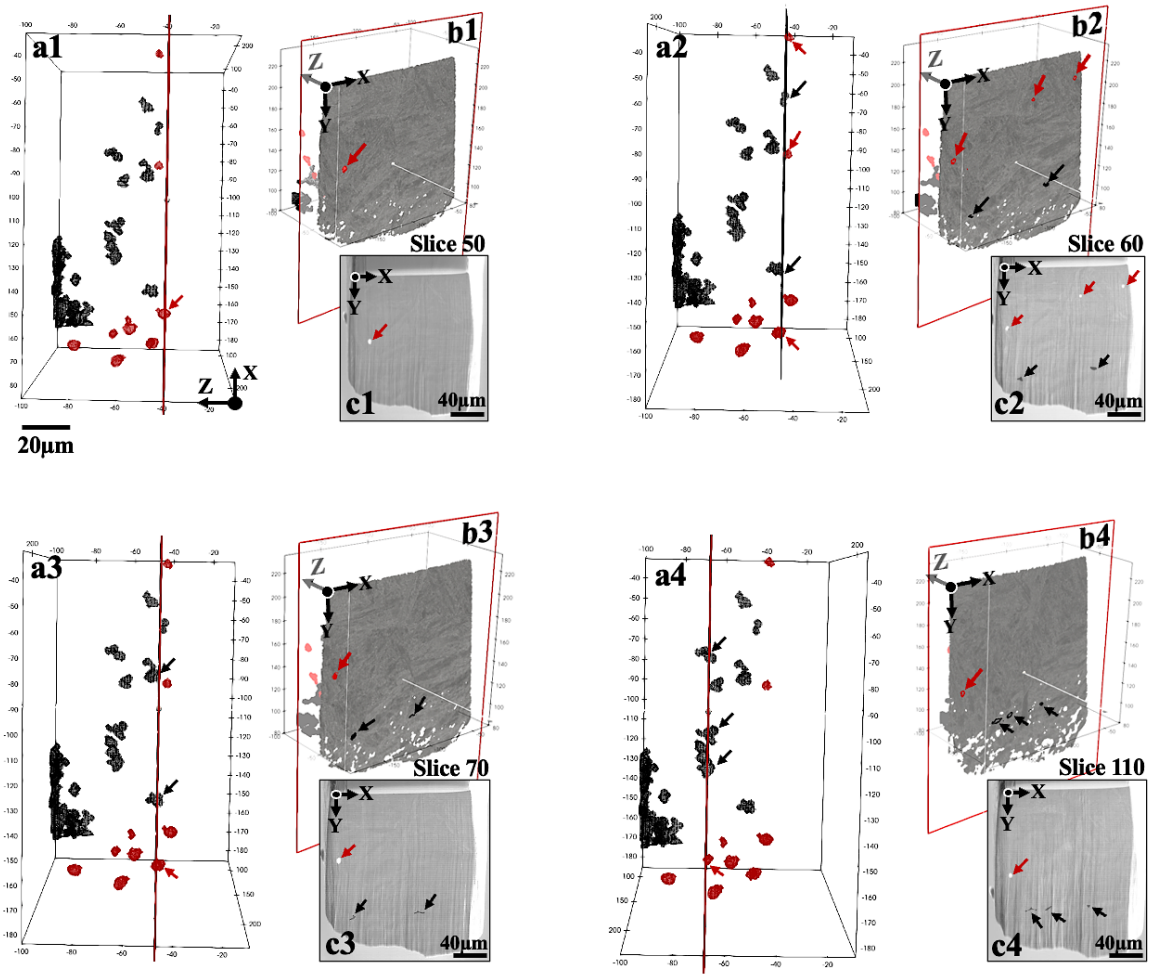

Figure 2.5: (a1-a4) The progressive detection of pores (shown in black) and inclusions (shown in red) across layers of the 3D structure, using a combination of band contrast (BC) **(b1-b4)**, and forward scatter diodes (FSD) **(c1-c4)** maps, corresponding to slices 50, 60, 70, and 110, respectively. (Black and red arrows in both volumetric and 2D views indicate the same pores and inclusions across slices, enabling the tracking of their spatial distributions and morphological changes through a comparative 2D and 3D analysis for each individual feature).

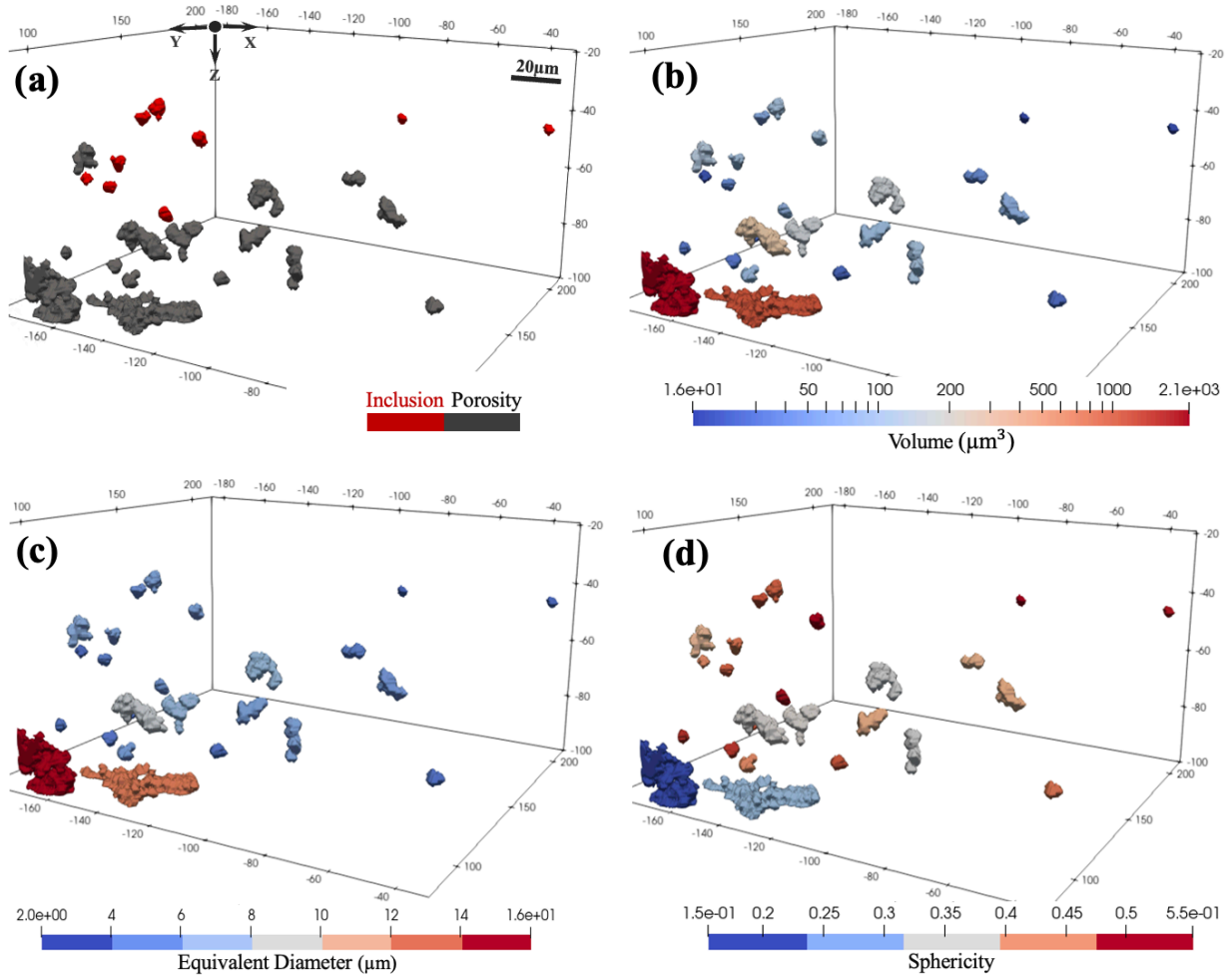

Figure 2.6: 3D visualizations of pores (black) and inclusions (red) in **(a)**, with features color-coded based on their volumes **(b)**, equivalent diameters **(c)**, and sphericity **(d)**, highlighting their morphological characteristics and spatial distributions.

Figures 2.6(a-d) presents 3D visualizations of the pores and inclusions, detailing their volumes, EDs, and sphericity values. The micropores were subsequently categorized into three primary types: gas pores (Figures 2.7(a1-a4)), gas-shrinkage pores (Figures 2.7(b1-b4)), and shrinkage pores (Figures 2.7(c1-c4)). Gas pores, nearly spherical with average sphericity coefficients of 0.49±0.03 and small volumes (<75 μm³), formed due to trapped gas during early solidification, resulting in smooth, round morphologies [85-87]. Instances of coalescence between

these gas pores were observed, as illustrated in Figure 2.7(a3). Gas-shrinkage pores, illustrated in Figures 2.7(b1-b4), display intermediate morphologies characterized by convex protrusions or elongated tails. A larger average volume of 116±72 μm³ and a reduced average sphericity coefficients of 0.37±0.04, reflect the combined effects of gas entrapment and shrinkage during solidification [85-87]. In contrast, shrinkage pores, shown in Figures 2.7(c1,c2), are highly irregular and interconnected (Figures 2.7(c3,c4)), with an average volume of 1650±450 μm³ and a sphericity coefficient averaging 0.21±0.06. Inclusions, depicted in red in Figures 2.6 and 2.7, were near-spherical, with an average volume of 52.6±29 μm³ and a sphericity coefficient of 0.51±0.03.

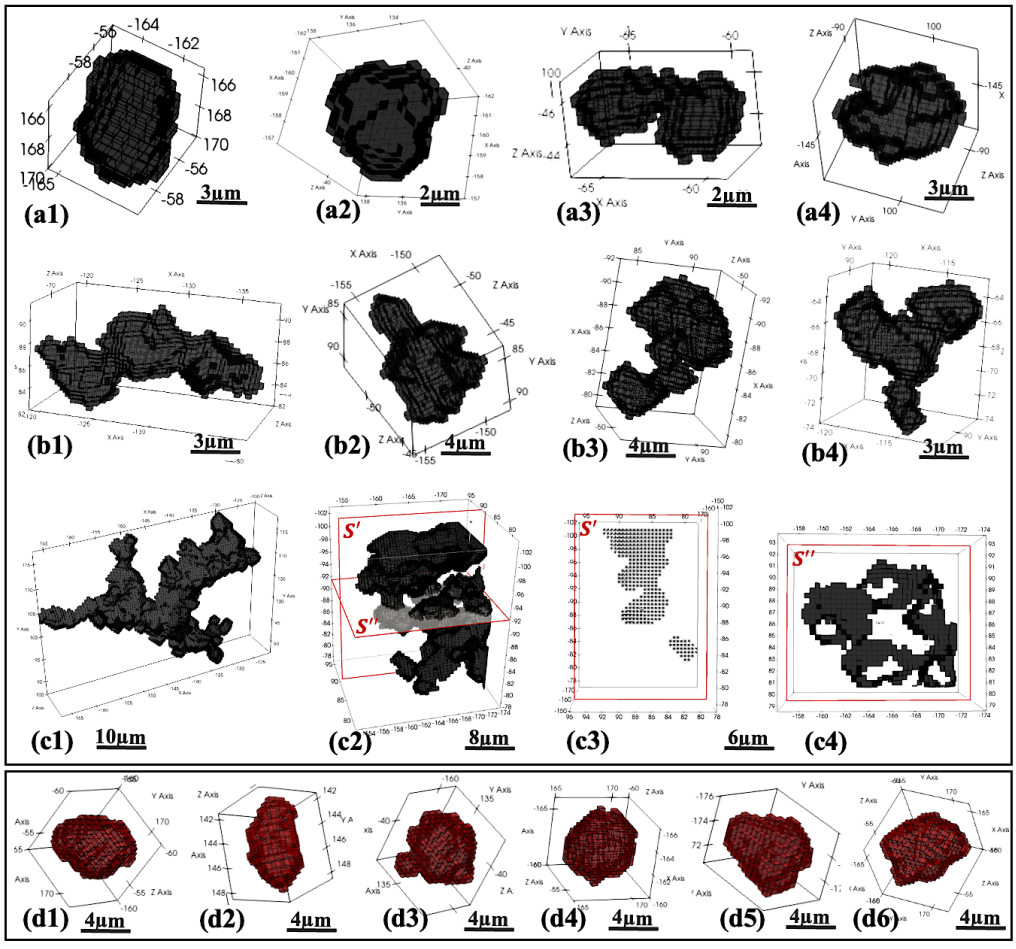

Figure 2.7: Examples of gas pores **(a1-a4)**, gas-shrinkage pores **(b1-b4)**, shrinkage pores **(c1-c4)**, and inclusions **(d1-d6),** reconstructed in 3D. **(c3, c4)** Two cross-sectional views of the complex pore shown in (c2), across S′and S″ planes, respectively.

The identification and reconstruction of delta-ferrite particles were carried out using Kernel Average Misorientation (KAM) analysis, which effectively distinguished these particles based on their lower KAM values relative to the surrounding martensitic matrix (Figures 2.8(a-c)) [88]. KAM mapping was particularly useful for identifying smaller, spherical particles that might otherwise be indistinguishable from the martensitic matrix in conventional IPF and BC maps. In total, 12 delta-ferrite particles were identified within the reconstructed volume, corresponding to a volumetric fraction of 0.94%. These 3D analyses revealed two distinct morphologies of delta-ferrite particles: (i) elongated particles located at or near PAGBs, such as P1-P3 in Figures 2.8(a-c), and (ii) smaller, spherical particles distributed within PAGs interiors, such as P4 and P5 in Figures 2.8(a-c). Additionally, the elongated particles P1 and P2 in Figures 2.8(d1-d3) and (e1-e3), respectively, exhibit faceted interfaces, whereas particle P3, with only a limited contact with its adjacent PAGB (indicated by the red arrow in Figure 2.8(a)), displays a spherical cross-section, indicative of a non-faceted interface (Figures 2.8(f1-f3)). As discussed by Smith [91] and Hillert [92], such faceted morphology, referred to as smithiomorph morphology, is characteristic of grain boundary allotriomorphs. It is hypothesized that the "grain boundary nucleated ferrite" tends to adopt a favorable orientation relationship with one of the austenite grains, resulting in a partially coherent interface with low mobility and energy (i.e., the faceted side) [92,93]. Conversely, the other side of the nucleus interacts with the adjacent grain through a mobile, incoherent interface, contributing to its relatively round morphology.

To gain a comprehensive understanding of these microstructural features and their collective role in shaping the overall 3D microstructure, Figure 2.9 illustrates the spatial distribution of micropores (black), inclusions (red), delta-ferrite particles (blue), and PAGBs (transparent black). Delta-ferrite particles exhibit the broadest equivalent diameter range, spanning from 2.6 μm to

25.7 μm. Their morphology varies from small, spherical particles below 7 μm (with average sphericity of 0.48±0.08), to elongated particles exceeding 25 μm (with average sphericity of 0.28±0.01), reflecting their dual morphological characteristics. Micropores, in contrast, show a narrower equivalent diameter range of 3.6 μm to 16 μm, but still display notable diversity, ranging from small gas pores with diameters below 9μm to larger shrinkage pores exceeding 16 μm. The sphericity of micropores, ranging from 0.15 to 0.53, decreases significantly with increasing size, reflecting the irregular and complex morphology of larger shrinkage pores. Inclusions, predominantly spherical, exhibit the narrowest equivalent diameter range (3.2 μm to 5.5 μm) and, unlike micropores, exhibit no significant size-dependent variations in sphericity, highlighting their morphological stability. Regarding spatial organization, spherical delta-ferrite particles exhibit the most uniform distribution within the analyzed volume. Inclusions show moderate clustering, with slightly higher concentrations in localized regions, while micropores exhibit the highest degree of clustering, consistent with their formation mechanisms and irregular morphologies. This comprehensive 3D analysis highlights the heterogeneous distribution and morphological diversity of these microstructural features, emphasizing their potential impact on the mechanical properties and transformation behaviors of the material.

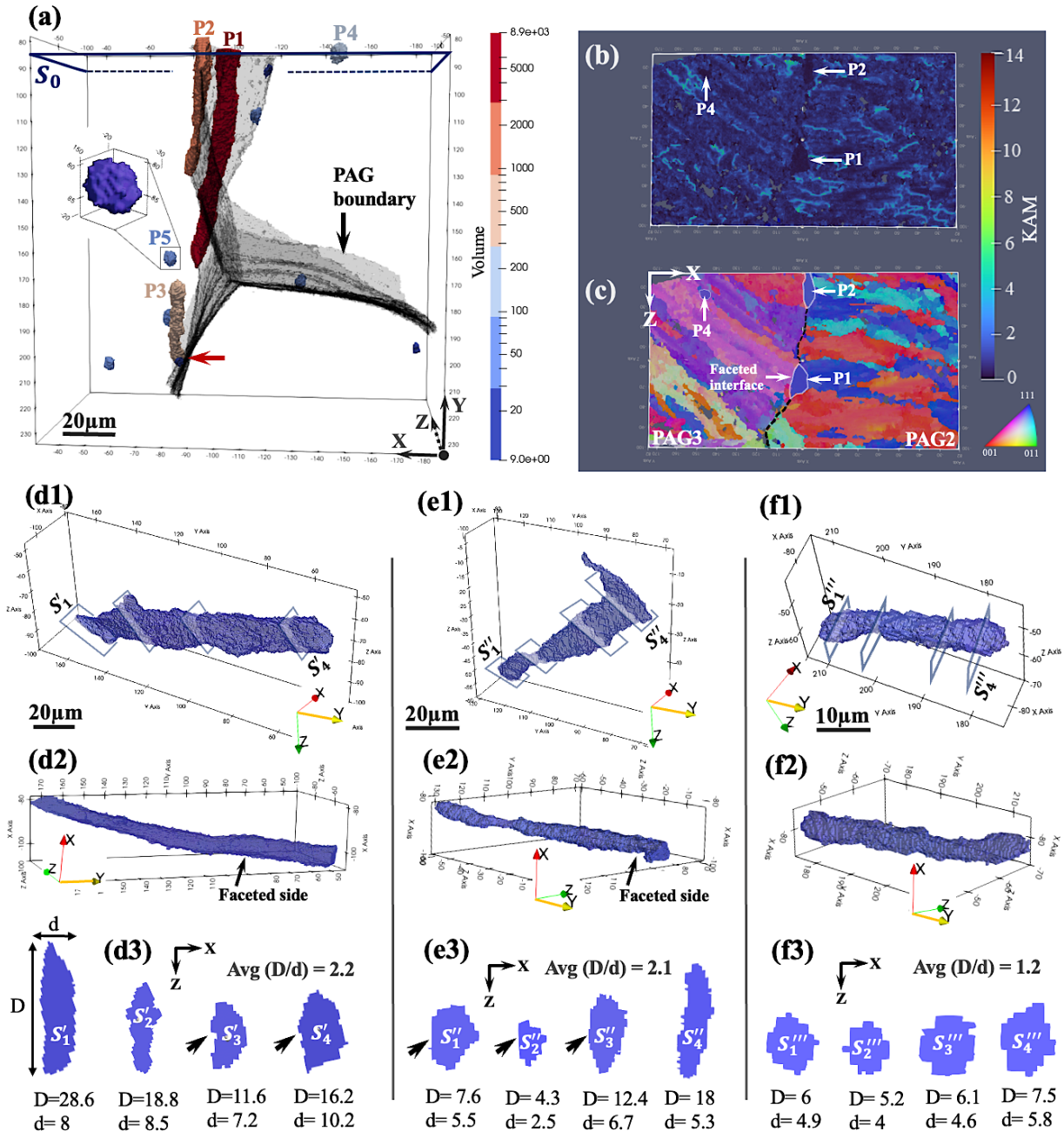

Figure 2.8: (a) 3D distribution of delta-ferrite particles with relative to the PAGBs, color-coded according to their volumes, with the five largest particles labeled as P1-P5. **(b, c)** 2D cross-sectional views of the microstructure (parallel to the S_0 plane in (a)), displayed as kernel average misorientation (KAM) and IPF-Z maps, highlighting particles P1, P2 and P4. Isolated 3D views of particles P1, P2, and P3 are presented in **(d1, d2)**, **(e1, e2)** and **(f1, f2)**, respectively, from two different perspectives. Cross-sectional views of P1, P2, and P3, are also presented in **(d3, e3, f3)**, respectively. The approximate locations of these cross-sectional views, labeled as S_1'-S_4', S_1''–S_4'', and S_1'''–S_4''', are shown in (d1), (e1), and (f1), respectively. Black arrows in (d2, d3, e2, e3)) point to the faceted sides of P1 and P2 particles. The average aspect ratios of the cross-sections shown in (d3, e3, f3) are denoted as Avg(D/d), where d and D are defined in (j)).

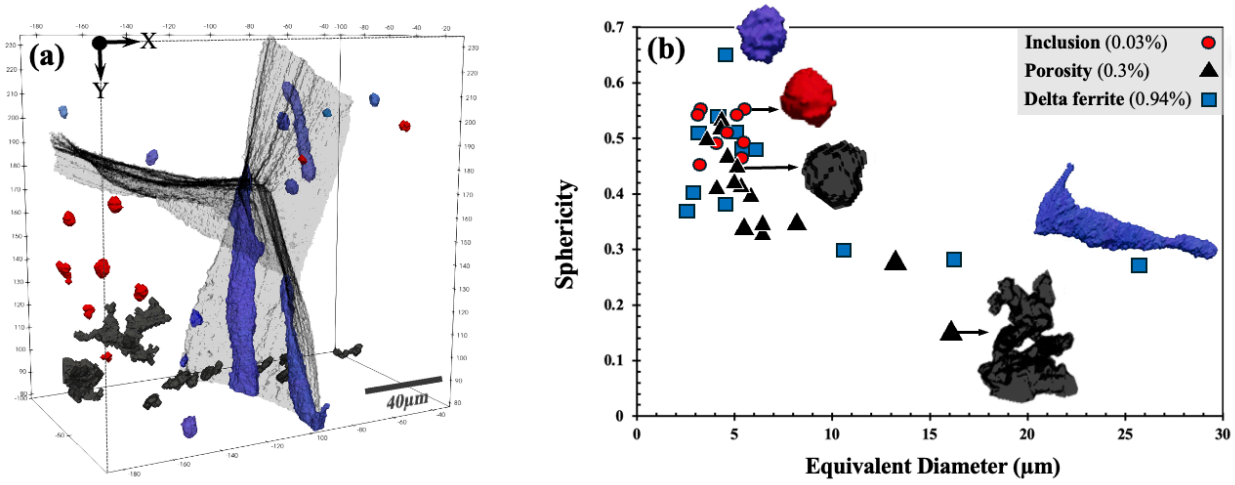

Figure 2.9: (a) 3D distribution of micropores (black), inclusions (red), delta-ferrite particles (blue), and prior austenite grain boundaries (transparent black), within the microstructure volume. **(b)** A graph illustrating the relationship between equivalent diameter and sphericity of pores, inclusions, and delta ferrite particles. The volume fractions of these features are presented in the top-right corner of (b).

2.3.4 3D visualization and distribution of internal boundaries

Figure 2.10 presents a detailed 3D visualization of internal boundaries, extracted from the segmented microstructure at a misorientation tolerance of 1° (Figure 2.3(a3)). To effectively illustrate the complexity of the boundary network, boundaries were color-coded based on their misorientation angles (θ) and classified into four distinct groups (Figures 2.10(c1-c4)). The classification scheme was designed to illustrate both K-S (Table 2.1) and non-K–S boundaries (θ ≈ 20-45°) with minimal overlap, ensuring a clear distinction between different boundary types. To establish a robust classification, the following sequential approach was adopted:

I. **Identification of Non-K-S Boundaries ($23° \leq \theta \leq 45°$)**

- The first step was to isolate non-K-S boundaries from the entire boundary network to minimize interference with K-S boundaries.

- A misorientation range of 23–45° was determined through iterative thresholding, optimizing for minimal overlap with the K-S boundaries (Figure 2.10(c3)).
- This approach aligns with previous studies [13,94] on misorientation-based phase transformation analysis, where boundaries with angles in this range are often associated with non-K-S martensite-austenite interfaces or deformation-induced boundaries.

II. **Extraction of Low-Angle Boundaries ($5° \leq \theta \leq 10°$)**

- Low-angle boundaries, typically corresponding to sub-block boundaries [8,17]**,** were then isolated and categorized separately (Figure 2.10(c1)).

III. **Classification of K-S Intervariant Boundaries ($10° < \theta < 23°$ and $45° < \theta \leq 62°$)**

- The remaining boundaries, predominantly corresponding to K-S intervariant boundaries**,** were categorized into two distinct groups (Figures 2.10(c2, c4)).
- These two groups encompass both packet boundaries (PBs) and block boundaries (BBs), which were identified based on their misorientations and using the crystallographic variant analysis within MTEX toolbox.
- BBs were defined as interfaces between two variants within the same crystallographic packet (e.g., between V1 and V2–V6), while PBs were characterized as interfaces formed by the impingement of variants from different packets, each possessing distinct habit planes (e.g., between V1 and V7–V24) [2,11,13].

Given that experimental misorientations often deviate slightly from theoretical values [13,94], a 3° deviation limit was applied for the precise identification of PBs and BBs. The relative populations of PBs and BBs within the microstructure were quantified and presented in Table 2.1, allowing for a deeper statistical understanding of boundary distributions. Each boundary category was then subjected to detailed morphological analyses to assess its role in the overall 3D microstructural architecture, which is further discussed in the following sections.

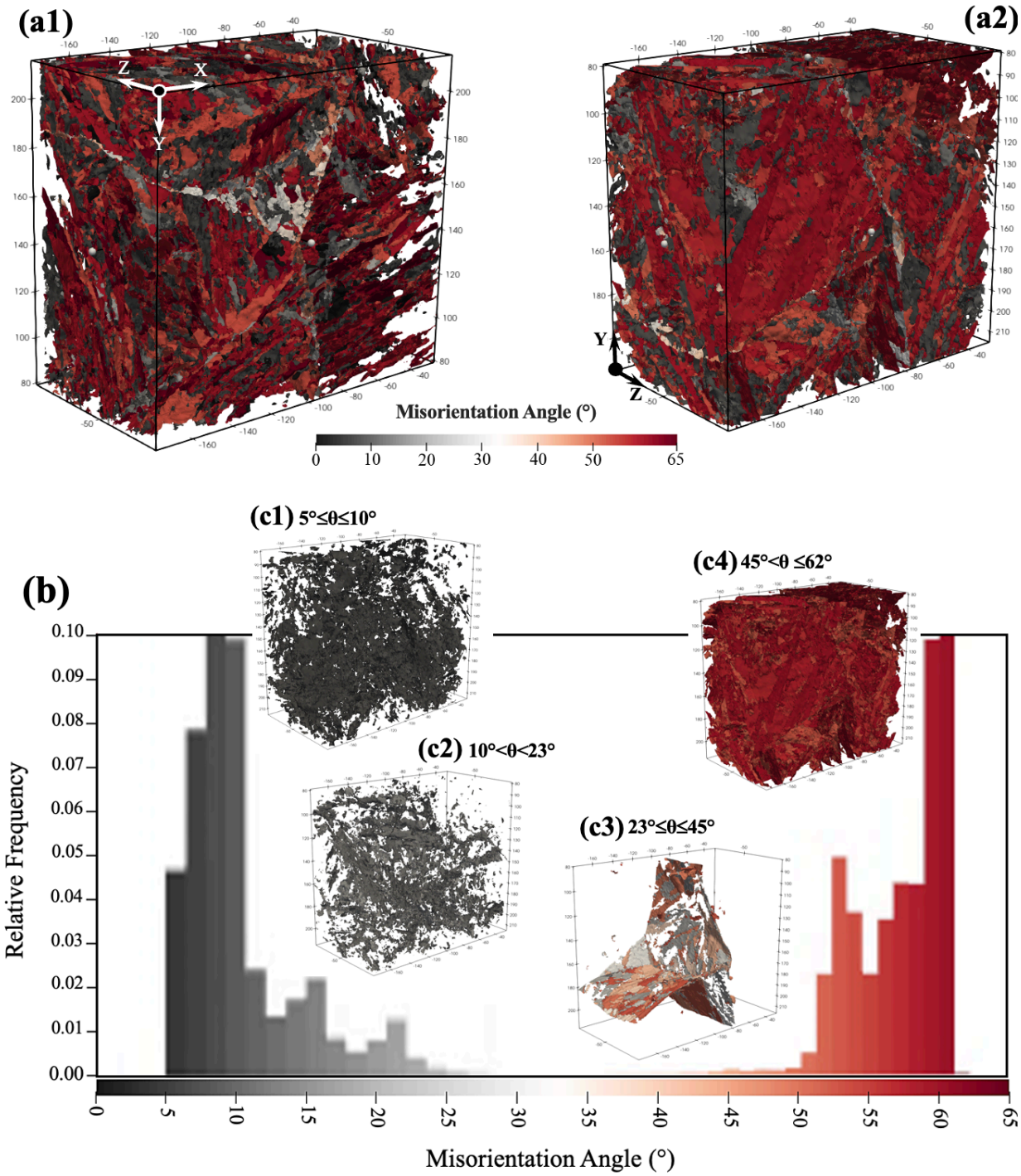

Figure 2.10: (a1, a2) Two perspectives of the microstructure showing the 3D network of internal boundaries color-coded based on their misorentation angles (θ). **(b)** Misorientation angle distribution for boundaries within the range of 5°–65°, extracted from (a1, a2). **(c1-c4)** 3D representation of internal boundaries categorized by misorientation angle ranges of 5°≤θ<10°, 10°<θ<23°, 23°<θ<45°, and 45°<θ≤62°, respectively. (For reference, the 3D volumes in (a1) and (c1–c4) share the same perspective and scale as those shown in Figures 2.2, 2.4, and 2.9).

2.3.4.1 Boundaries with misorentation angle range of 5° ≤ θ ≤ 10°

Figure 2.11 provides a comprehensive 3D visualization of low-angle boundaries (LABs) within the 5°–10° misorientation range, which account for approximately 25% of the total boundary network, confirming the presence of numerous sub-block boundaries, consistent with previous observations [10,95]. Given the complexity and heterogeneity of these boundaries, a size-based classification was implemented to facilitate their 3D visualization and morphological analysis. Boundaries were categorized by surface area into three distinct groups: small (10–100 μm²), medium (101–700 μm²), and large (701–2069 μm²), as shown in Figures 2.11(b1–b3). This classification was helpful with identifying distinct boundary morphologies and to account for their significant size variability. Three primary boundary morphologies were identified: (i) small, closed-loop or high-curvature segments (Figures 2.11(c1, c2)), (ii) medium-sized, elongated boundaries with strip-like geometries (Figures 2.11(c3–c5)), and (iii) large, irregular boundaries with porous and tortuous structures (Figure 2.11(c6)).

Large, irregular boundaries are commonly observed separating substantial sub-blocks (e.g., V1 and V4 in Figure 2.11(c6)), exhibiting tangled and tortuous morphologies. Further misorientation analysis revealed that these boundaries possess a misorientation angle of approximately 7°, which can be related to the prominent 7° peak in the misorientation angle distributions provided in Figure 2.10(b) and Figure 2.1(h). Despite their pronounced irregularity, these large-area boundaries tend to align parallel to the longitudinal axis of the parent block, as indicated by the black and white arrows in Figure 2.11(c6). This directionality suggests structural anisotropy, consistent with the findings of Morito et al. [8,10], who reported variations in sub-block morphologies even among those aligned along similar directions. Such complex boundary morphologies can be attributed to the coupled, competitive growth dynamics of large sub-blocks

during the martensitic transformation [8,11]. Medium-sized boundaries, characterized by strip-like geometries, generally separate elongated sub-blocks with relatively simple shapes from the parent block. These boundaries were predominantly observed along the edges of the blocks, as shown in Figures 2.11(c3-c5). As evident, some of these strip-like boundaries align with the longitudinal axis of the parent block (Figure 2.11(c3)), while others are oriented perpendicularly (Figures 2.11(c4, c5)). This variation in orientation may indicate the presence of directional stresses and anisotropic transformation behaviors, as demonstrated by Archie et al. [96], who analyzed micro-stresses in lath martensite using the FIB ring-core milling technique. Small boundaries, typically characterized by closed-loop or high-curvature geometries, define and isolate smaller sub-blocks within the parent block (Figures 2.11(c1, c2)). Two examples of the segmentation of large blocks involving these three types of sub-block boundary morphologies are demonstrated in Figures 2.11(d1, d2) and Figures 2.11(e1, e2).

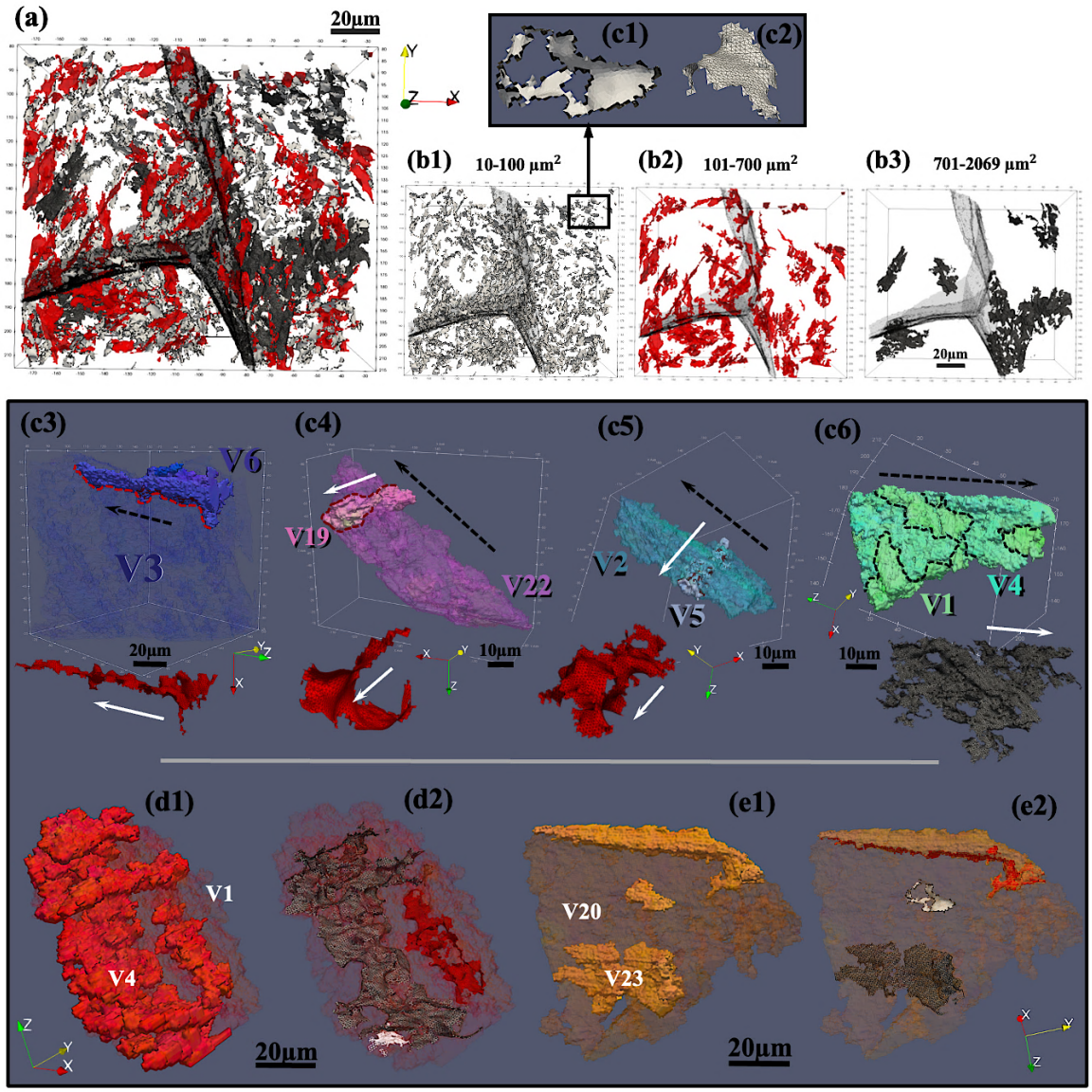

Figure 2.11: (a) 3D distribution of sub-block boundaries within the misorientation angle range of 5°≤θ<10°, classified based on area size into small boundaries (10-100 µm², shown in white), medium boundaries (101-700 µm², shown in red), and large boundaries (701-2069 µm², shown in black). PAGBs are also rendered in transparent black to provide spatial reference and a better sense of scale. **(c1-c6)** Representative examples of sub-block boundaries corresponding to area sizes of 10-100 µm² (c1, c2), 101–700 µm² (c3-c5), and 701–2069 µm² (c6), illustrating their 3D morphologies and associated sub-blocks/variants. Black arrows in (c3-c6) indicate the longitudinal direction of blocks/sub-blocks, while white arrows denote the longitudinal orientation of sub-block boundaries. The outlines of sub-block boundaries in (c3-c6) are highlighted with black and red dashed lines. **(d1, d2)** A large block segmented into multiple sub-blocks corresponding to K-S variants V1 (shown in transparent red) and V4 (shown in solid red), along with the sub-block boundary network formed between these variants. **(e1, e2)** A large block segmented into multiple sub-blocks corresponding to K-S variants V20 (shown in transparent orange) and V4 (shown in solid orange), along with the sub-block boundary network formed between these variants.

2.3.4.2 Boundaries with misorentation angle range of 10° < θ < 23°

Figure 2.12(a) provides a comprehensive 3D visualization of boundaries with misorientation angles ranging between 10° and 23°, representing 16.8% of the overall boundary structure. According to the K-S intervariant misorientations listed in Table 2.1, this range includes several PB types, including misorientations of 10.5°[11-1], 14.8°[13 5 1], 20.6°[30-1], 20.6°[11-11-6], and 21.06°[9-40], as well as a single BB type corresponding to 10.5°[0-1-1]. Following 3D segmentation of these boundaries, PBs with a 14.8°[13 5 1] misorientation emerged as the most dominant boundary type within this range, accounting for 6.1% of the overall boundary structure. These boundaries, highlighted in red in Figure 2.12(a, b), form an interconnected network of elongated/high-aspect-ratio boundaries, which play a critical role in partitioning the martensitic microstructure into distinct packets. Conversely, PBs associated with the remaining four intervariant misorientations (10.5°[11-1], 20.6°[30-1], 20.6°[11-11-6], and 21.06°[9-40]), rendered in white in Figure 2.12(a, b), display a more fragmented and discontinuous network. Collectively, these PBs account for a total area fraction of 6.8%, only slightly surpassing the contribution of the 14.8°[13 5 1] PB alone. On the other hand, BBs with a 10.5°[0-1-1] misorientation, shown in yellow in Figure 2.12(a, c), are significantly less prevalent compared to PBs. These BBs are characterized by shorter, segmented geometries and occupy a smaller area fraction of 3.9% within the microstructure. These observations suggest that within the $10° \leq \theta < 23°$ range, PBs are the primary contributors to defining the overall microstructural hierarchy, whereas BBs primarily provide localized structural refinement within the established packet framework.

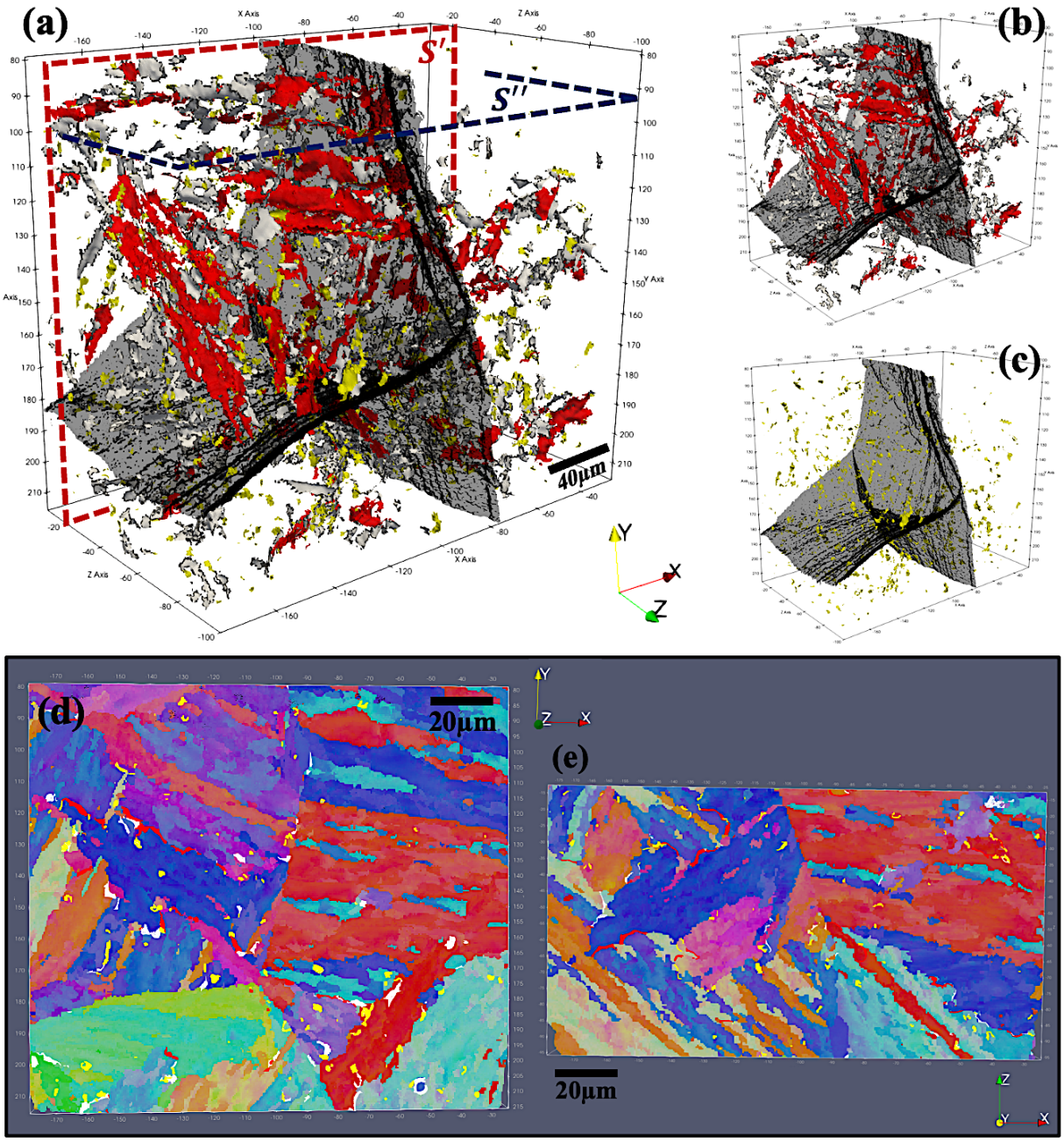

Figure 2.12: (a) 3D distribution of boundaries within the misorientation angle range of 10°<θ<23°. **(b, c)** Isolated 3D networks of PBs and BBs, respectively: boundaries in red correspond to 14.8°[13 5 1] PBs, boundaries in white represent 10.5°[11-1], 20.6°[30-1], 20.6°[11-11-6], and 21.06°[9-40] PBs (b), and boundaries in yellow correspond to 10.5°[0-1-1] BBs (c). **(d, e)** two cross-sectional views of the microstructure (parallel to S' and S'' in (a)) illustrating the distribution of 10°<θ<23° boundaries overlaid on 2D IPF-Z maps, with boundaries color-coded as in (a-c). The prior austenite grain boundary (PAGB) is indicated by transparent black in (a).

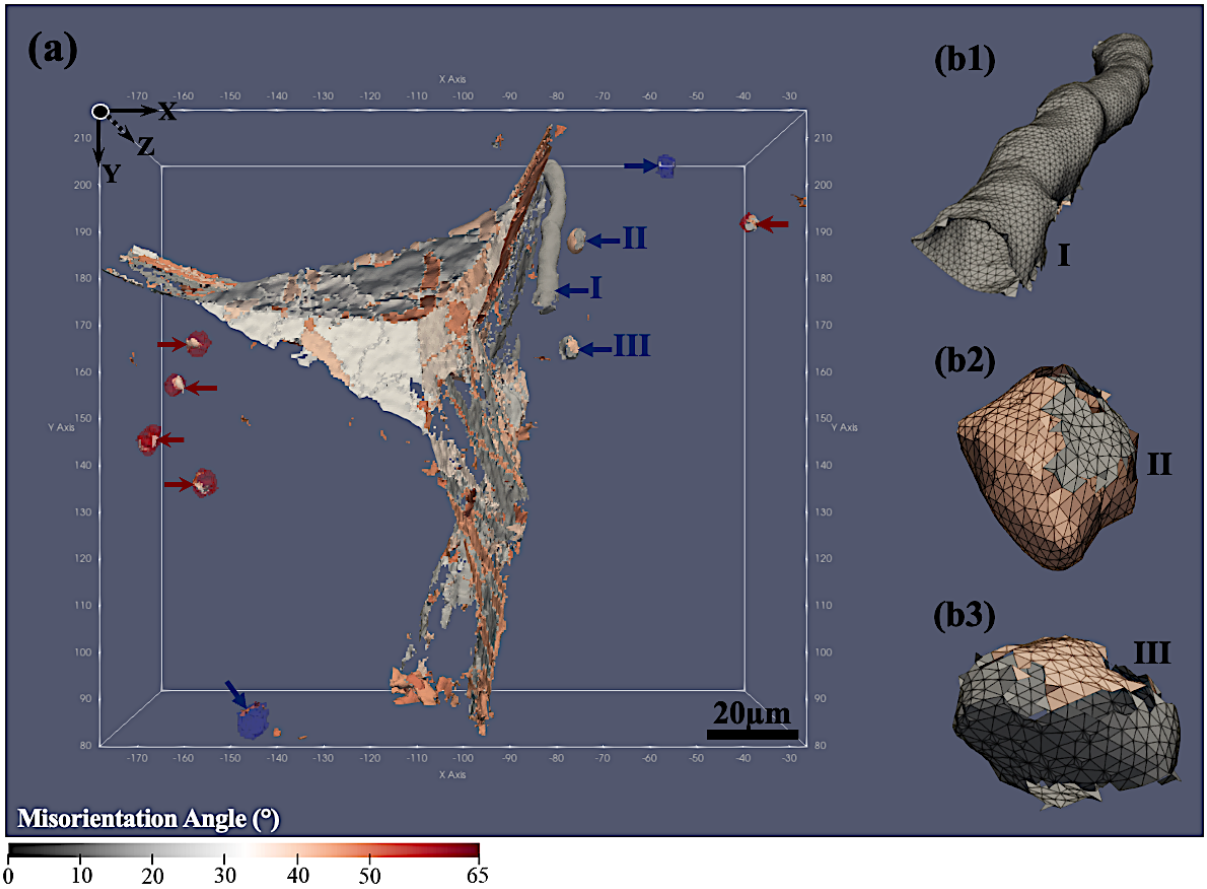

Figure 2.13: (a) 3D distribution of boundaries within the misorientation angle range of 23°<θ<45°. Interfaces between inclusions and the martensitic matrix, as well as those between ferrite particles and the martensitic matrix, are indicated with red and blue arrows, respectively. **(b1–b3)** 3D meshed views of three distinct ferrite/martensite interfaces, labeled as I, II, and III in (a).

2.3.4.3 Boundaries with misorentation angle range of 23° ≤ θ ≤ 45°

Figure 2.13(a) presents a 3D analysis of boundaries with misorientation angles ranging from 23° to 45°, accounting for 8.3% of the overall boundary structure. This range, corresponding to the characteristic "gap" observed in the misorientation angle distributions shown Figure 2.10(b) and Figure 2.1(h), is primarily associated with PAGBs or non-K-S boundaries. The heterogeneous crystallographic structure of these boundaries (Figure 2.13(a)) originates from the martensite variants that either nucleate at original austenite grain boundaries or terminate their growth upon

encountering these boundaries. In addition to these predominant PAG boundaries, Figures 2.13(b1-b3) highlights other interfaces within the same misorientation angle range. These include boundaries at the interfaces between inclusions and the martensitic matrix (indicated by red arrows) and those between delta-ferrite particles and the martensitic matrix (indicated by blue arrows). These interfaces are indicative of localized microstructural heterogeneity, reflecting interactions between the transforming austenite and pre-existing features such as inclusions or delta-ferrite particles. Such interactions likely influence local transformation kinetics, variant selection, and the resulting boundary morphologies [97-101].

2.3.4.4 Boundaries with misorentation angle range of $45° < \theta \leq 62°$

A 3D visualization of boundaries with misorientation angles ranging from 45° to 62° is presented by Figure 2.14. These boundaries, comprising 51% of the total boundary structure, are predominantly composed of high-angle BBs and PBs (Table 1). PBs can be associated with intervariant misorientations of 47.1°[-10 21 24], 47.2°[-2-5-6], 49.5°[-1-11], 50.5°[-10 3 -13], 50.5°[-7 -5 5], 51.7°[-11 6 -11], 57.2°[-356] and 57.2°[-6-25], while BBs can be associated with intervariant misorientations of 49.5°[011], 60°[111] and 60°[011]. Notably, two of the BB types within this range are coincident site lattice (CSL) boundaries, including Σ11 (49.5°[011]) and Σ3 (60°[111]). BBs were subsequently segmented and rendered in yellow, green, and blue to represent Σ11, Σ3, and 60°[011] boundaries, respectively (Figures 2.14(c2-c4). PBs, forming the remainder of the boundaries in this range, were all rendered in red (Figure 2.14(c1)).

From a quantitative standpoint, PBs within this misorientation range account for 18% of the total boundary structure, while BBs contribute 33%, with the 60°[011] boundaries being the most prevalent at 14.7%. Σ3 and Σ11 boundaries collectively account for 18.3% of the total boundary

area, with Σ3 boundaries being the dominant type, constituting 12.1%. The dominance of BBs, particularly 60°/[110] and Σ3 boundaries, reflects a tendency for local variant pairing during the martensitic transformation. Although all the 24 K-S variants typically form with near-equal probability within a given austenite grain, local variant pairing often promotes the formation of specific intervariant boundaries, such as 60°/[110] boundaries, to accommodate strain from the shear transformation [13,102,103].

From a morphological perspective, PBs (Figures 2.14(c1, d1)) and Σ11 (Figures 2.14(c2, d2)) boundaries exhibit fragmented geometries with areas ranging from 25 μm² to 750 μm². The Σ11 boundary network, in particular, demonstrates the lowest level of connectivity within this misorientation range, thereby reducing its contribution to the overall structural cohesion. In contrast, Σ3 and 60°[011] boundaries are characterized by larger, more continuous regions, extending up to 11,000 μm² (Figures 2.14(d3, d4)). These larger boundary areas suggest a more prominent role in structural refinement and connectivity, particularly for the 60°[011] BBs, which show the highest connectivity with numerous intersections between the boundaries. The interconnected nature of 60°[011] boundaries, highlights their ability to enhance stress transfer and improve the overall toughness of the martensitic matrix, as previously noted in studies on martensitic steels [9,26].

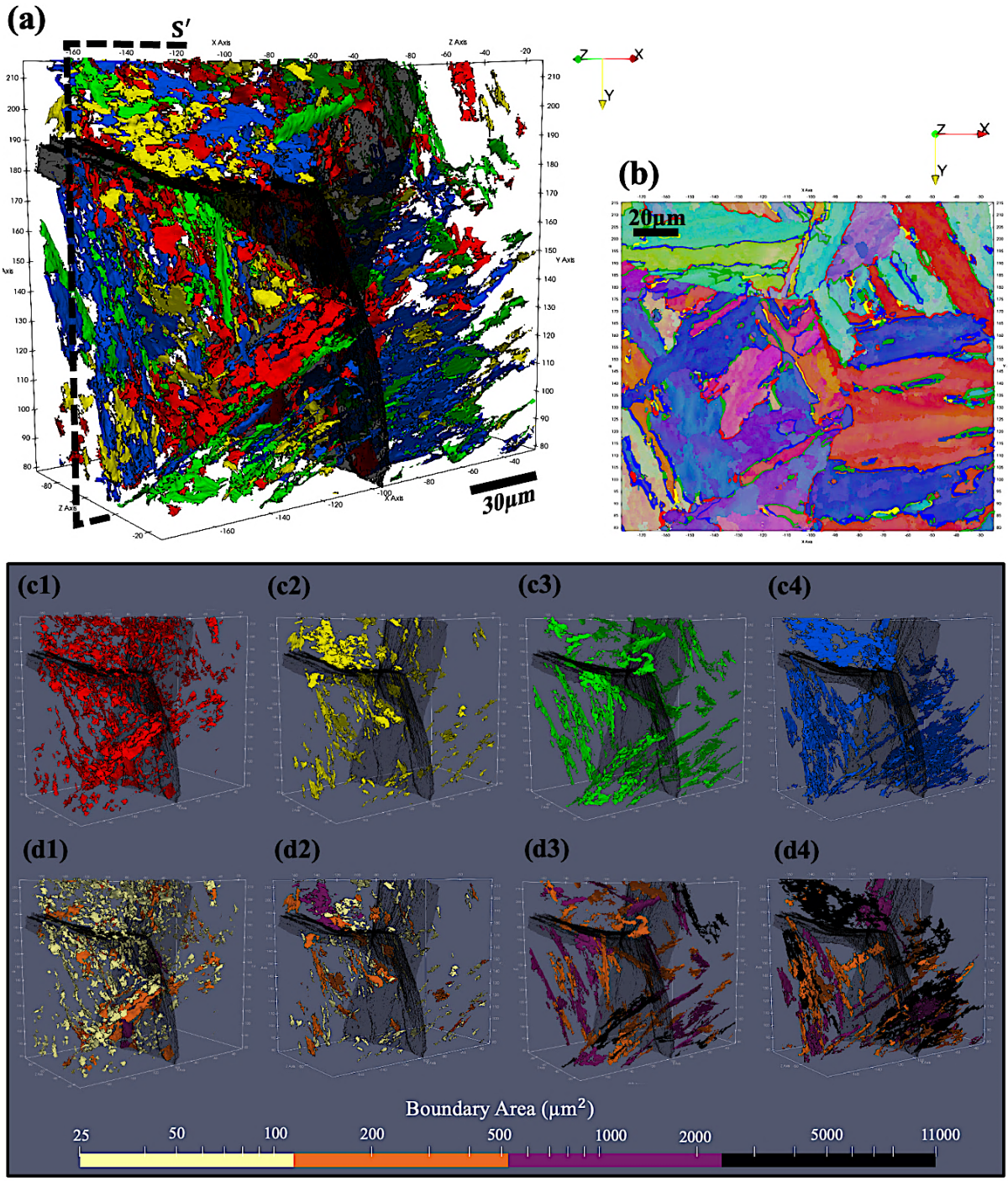

Figure 2.14: (a) 3D distribution of boundaries within the misorientation angle range of 45°<θ≤62°, with PBs represented in red and BBs shown in yellow, green, and blue, corresponding to 49.5°[011], 60°[111], and 60°[011] misorientations, respectively. (b) A cross-sectional IPF-Z map (parallel to S′ in (a)) showing the distribution of 45°-62° boundaries, color-coded as in (a). (c1-c4) Isolated 3D networks of PBs, 49.5°[011] BBs, 60°[111] BBs, and 60°[011] BBs, respectively. (d1-d4) 3D representations of the boundary networks from (c1-c4), with boundaries color-coded based on their area sizes (in μm²). (All 3D volumes share the same 3D perspectives for consistency.)

2.3.5 3D morphology of packet and block boundaries

Figures 2.15(a, b) provides a comprehensive 3D visualization of all BBs, PBs, and PAGBs, within the entire volume of the analyzed microstructure, highlighting their hierarchical structures and network characteristics; the PB network delineates the spatial extent of packets within each PAG, while BBs are confined to the internal regions of these packets, forming a dense and intricate network (Figure 2.15(b)).

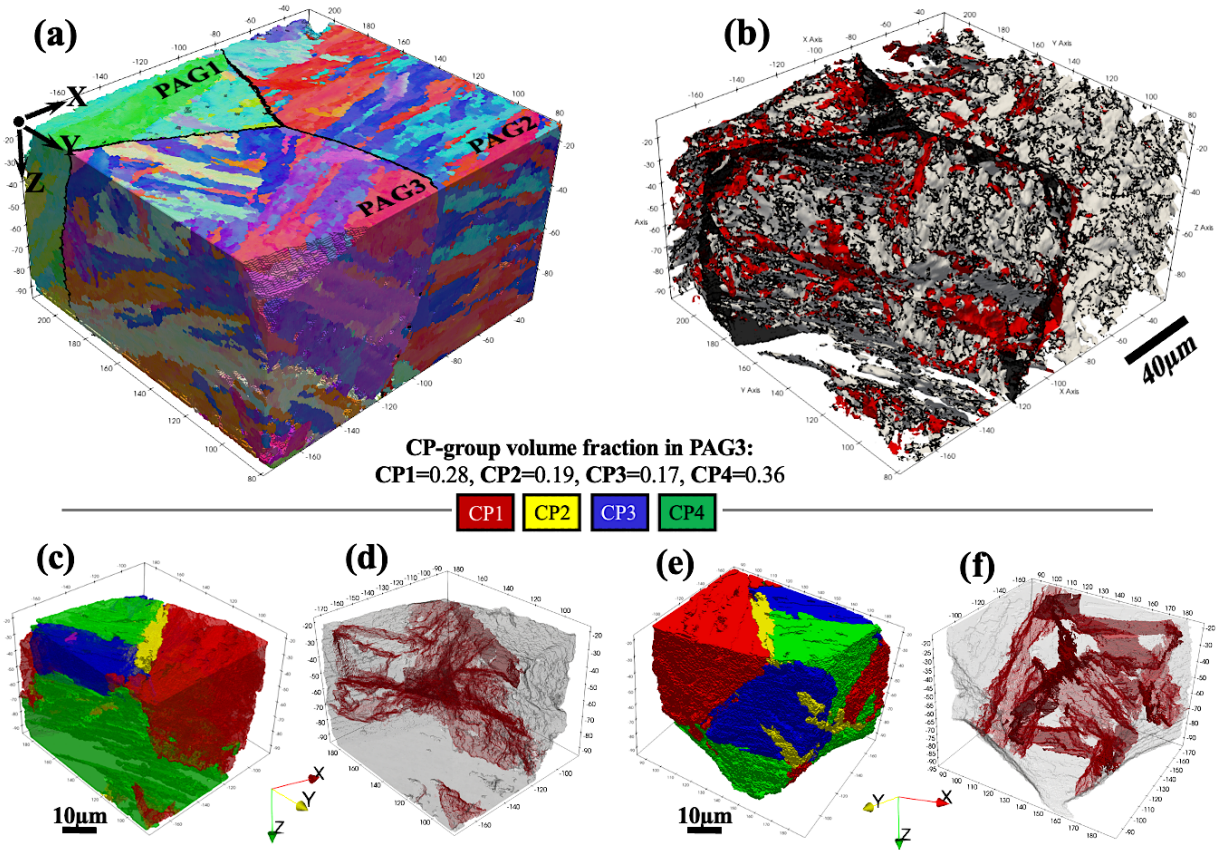

Figure 2.15: A volumetric representation of the microstructure in the form of IPF-Z map **(a)** and boundary map **(b)**, displaying all internal boundaries ($5°\leq\theta\leq62°$). Packet boundaries are shown in red, block boundaries in white, and PAGBs in black. **(c, e)** Two different views of PAG3, highlighting martensitic packets within the PAG volume, color-coded according to their corresponding close-packed (CP) $\{111\}\gamma$ //$\{110\}\alpha$ planes: red (CP1), yellow (CP2), blue (CP3), and green (CP4), representing the (111), (1-11), (-111), and (11-1) planes, respectively. **(d, f)** Two different views of the packet boundary network in PAG3, corresponding to the volumes in (c) and (e). (Note: All volumes in (a-d) share the same 3D perspectives.)

In the case of PB networks, greater details regarding their morphological characteristics and connectivity were achieved, when each PB was analyzed in relation to its corresponding packets (i.e., the pair of packets that form the PB at their contact surface) and their 3D interactions. Figures 2.15(c-f) and Figures 2.16(a-f) provide 3D visualizations of PAG3, along with its corresponding packets and PB network, serving as a representative example. As observed, packets are anisotropic in shape and exhibit varying spatial orientations, making their 3D interactions and resulting interfaces highly intricate and inhomogeneous, both morphologically and crystallographically. Taking these 3D interactions into account, PBs were classified into two primary types through a comprehensive analysis of the 3D reconstructions provided in Figures 2.16(a-f). The first type of PB morphology occurs when two growing packets merely contact each other and create a wavy or step-like interface (Figures 2.17(a-c)). These boundaries exhibit minimal complexity and narrow misorientation distributions (Figure 2.17(d)), indicating a straightforward interaction. This interaction, also referred to as hard impingement of blocks/packets, has been previously discussed by Wan et al. [71] in their study of acicular ferrite in a low-carbon steel weld metal. In contrast, the second type of PB morphology emerges when two growing packets intersect as they widen in nearly perpendicular directions. This mutual intersection leads to an interlocked martensitic microstructure (Figure 2.18(d)), producing more complex PB networks. These PB networks are characterized by broader misorientation distributions and increased curvature, that stems from the interplay between the variant configurations within each packet and the strains induced by their mutual penetration. Another example of this interaction type is depicted in Figure 2.19, where two blocks (B1 and B2) from different packets are highlighted in PAG2. As seen in Figures 2.19(a1-a5), these blocks intersect and interlock, creating a highly convoluted interface with significant curvature and diverse misorientation distributions (Figures 2.19(b1-b4)).

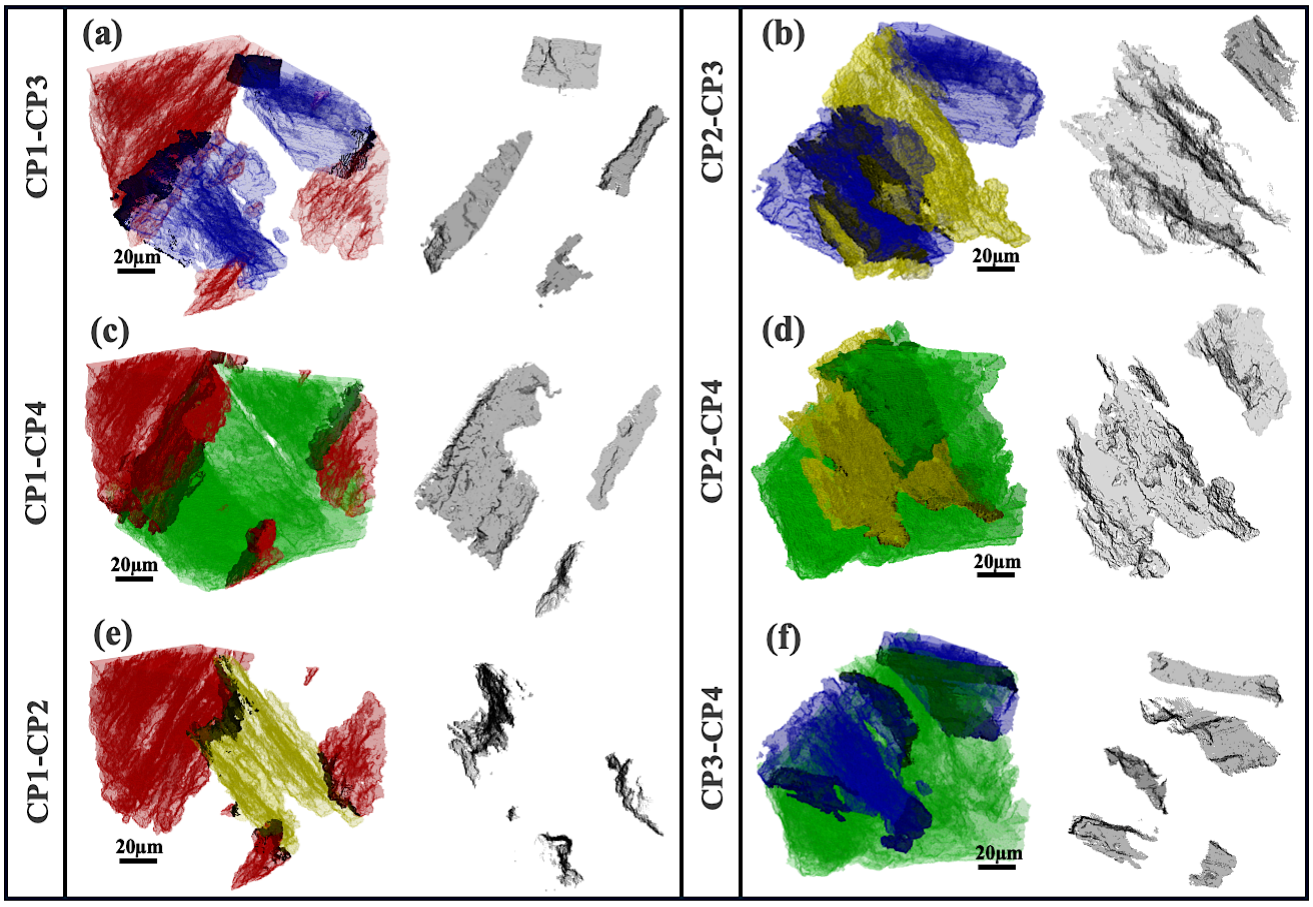

Figure 2.16: (a-f) 3D visualization of packet boundaries (rendered in transparent black) formed between pairs of CPs within PAG3. Packets are displayed in the same colors as the CP maps in Figure 2.15(c, e). All reconstructed CPs and their boundaries maintain the same 3D perspective as shown in Figure 2.15(e, f).

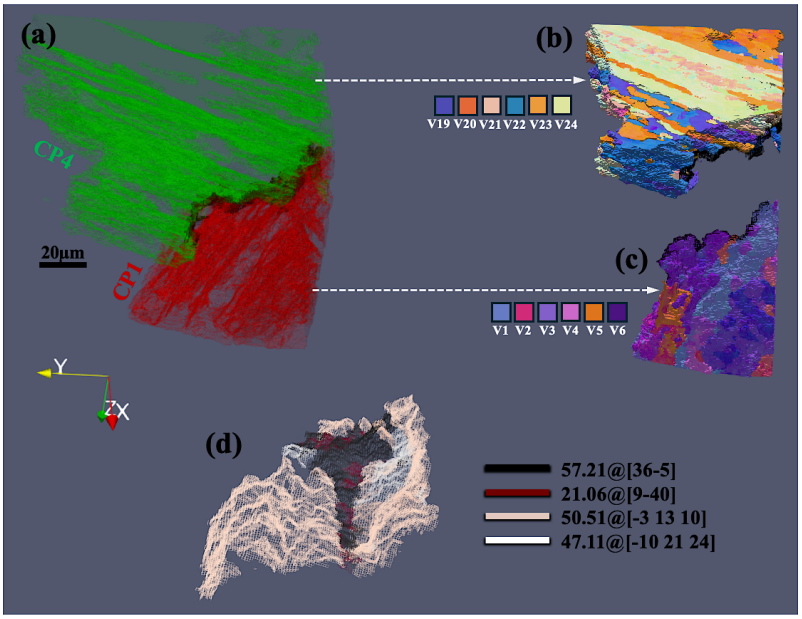

Figure 2.17: (a-c) Hard impingement of two distinct packets (corresponding to the CP1 and CP4 groups in Figure 16(c)), forming a wavy-shaped interface highlighted in black in (b, c). The 3D distribution of K-S variants within these packets (V1–V6 and V19–V24) is illustrated in IPF-Z maps in (b, c). **(d)** 3D reconstruction and misorientation distribution of the wavy-shaped boundary formed by the hard impingement of the packets shown in (a).

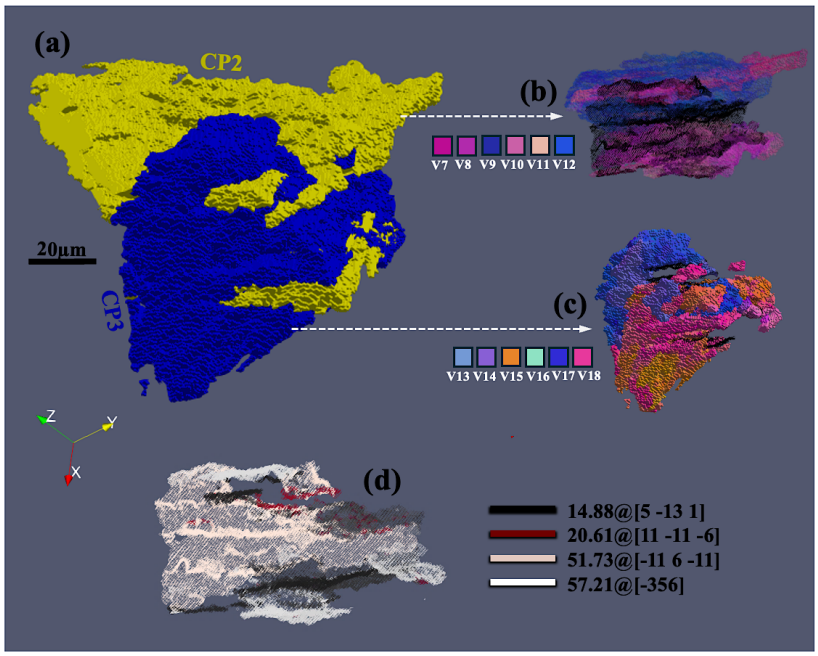

Figure 2.18: (a-c) Mutual intersection of two distinct packets (corresponding to the CP2 and CP3 groups in Figure 16(b)), forming an interlocked configuration with a complex interface, highlighted in black in (b, c). The 3D distribution of K-S variants within these packets (V7-V12 and V13-V18) is illustrated in IPF-Z maps in (b, c). **(d)** 3D reconstruction and misorientation distribution of the boundary formed by the mutual intersection of the packets shown in (a).

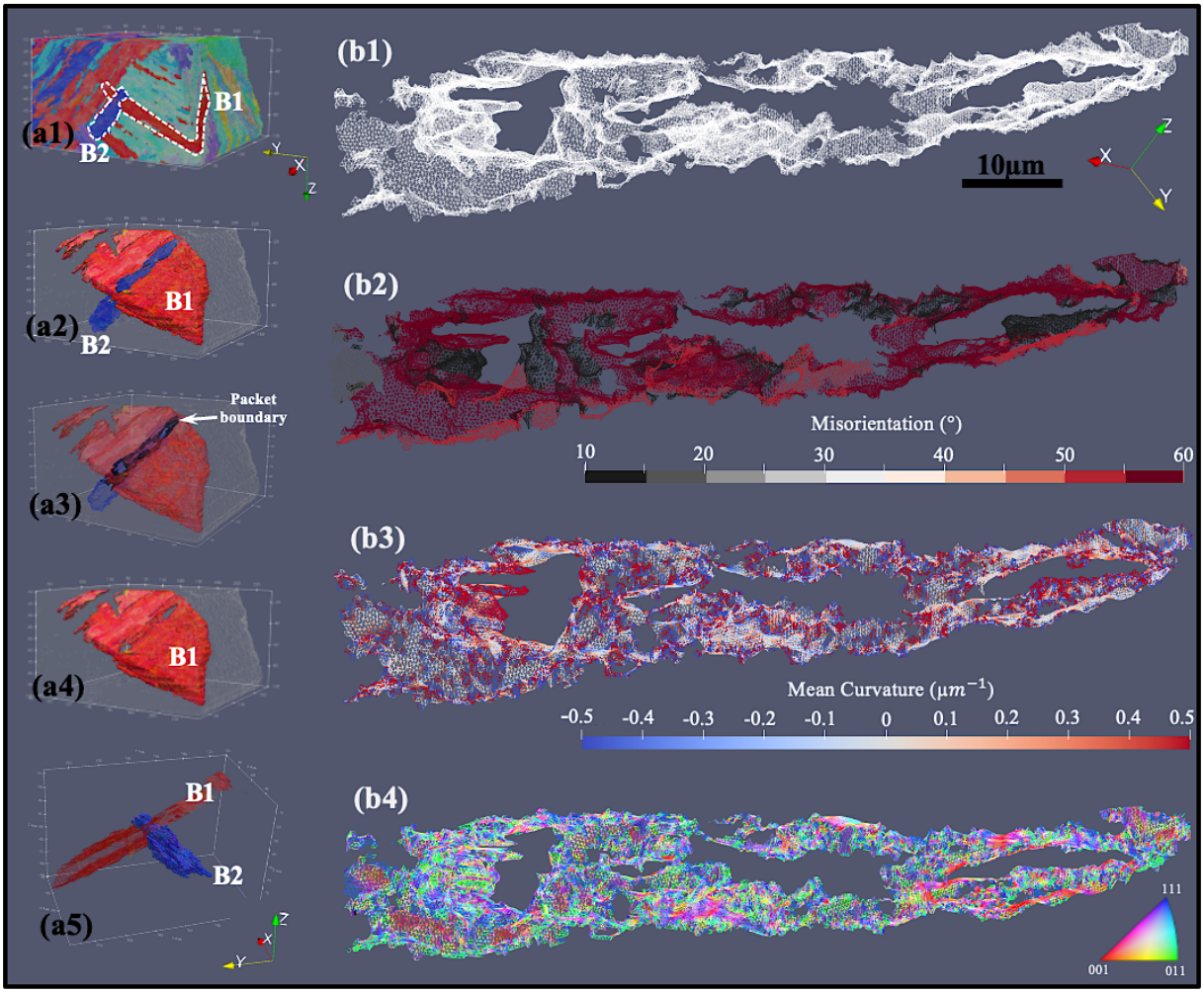

Figure 2.19: (a1) 3D view of the entire microstructure with two specific blocks highlighted by white dashed lines, labeled as B1 and B2. **(a2-a4)** 3D morphology and configuration of B1 and B2, with their interface highlighted in black in (a2). **(a5)** Alternate 3D rendering view of B1 and B2, illustrating their interlocked configuration. **(b1-b4)** 3D reconstruction of the interface between B1 and B2, color-coded based on misorientation angle distribution **(b2)**, mean curvature **(b3)**, and IPF-Z **(b4)**.

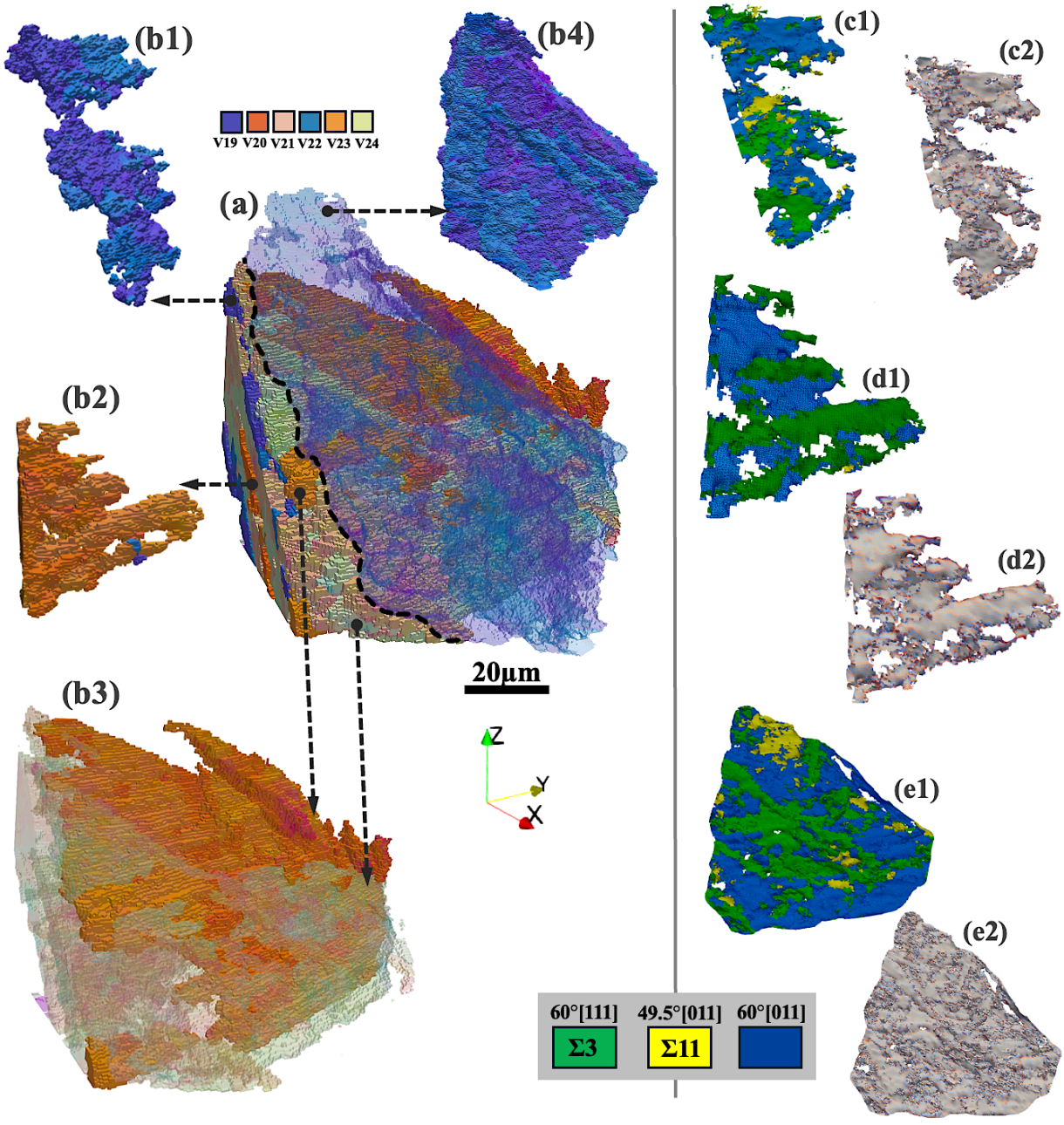

Figure 2.20: (a) 3D IPF-Z map of a packet corresponding to the CP4 group in Figure 17(b)in PAG3. **(b1-b4)** decomposition of the 3D volume of the selected packet into its largest constituent blocks. **(c1, c2)** Interface between the blocks shown in (b1) and (b3), represented through misorientation angle/axis and mean curvature distributions, respectively. **(d1, d2)** Interface between the blocks shown in (b2) and (b3), represented through misorientation angle/axis and mean curvature distributions, respectively. **(e1, e2)** Interface between the blocks shown in (b3) and (b4), represented through misorientation angle/axis and mean curvature distributions, respectively.

A similar 3D analysis was performed on BBs, as shown in Figure 2.20, focusing on a packet corresponding to CP4 in PAG3 (see Figure 2.17(b)). This packet was decomposed into its largest constituent blocks, revealing diverse morphologies ranging from thick, wedge-shaped blocks to thin, irregularly shaped blocks (Figures 2.20(b1-b4)), with notable thickness variations across their areas. Importantly, these blocks are not simply stacked or aligned but frequently interpenetrate, forming intricate networks of BBs. Examples of such networks are depicted in Figures 2.20(c1-e2). As evident, these interfaces are segmented into several high-angle BB regions with irregular or porous morphologies, sharing the same spatial boundary plane but exhibit distinct crystallographic features. Among these, 60°[011] boundaries demonstrate the highest level of continuity, serving as the primary structural framework for these interfaces. As expected, these interfaces are less curvilinear or step-like compared to PBs and are characterized by their relatively flat profiles. Such systematic observation of boundaries, inaccessible through conventional 2D characterization techniques, highlights the variability in boundary morphologies within lath martensitic steels and further offers valuable insights into their mechanical roles, particularly their influence on crack propagation behaviors, including the tortuosity of crack paths under different loading conditions.

2.4 Conclusions

This study highlights the significance and utility of advanced 3D characterization techniques in unraveling the intricate and heterogeneous nature of lath martensite in steels. The findings offer a detailed and comprehensive understanding of the hierarchical morphology of lath martensite and its internal interfaces, establishing a valuable foundation for future investigations aimed at exploring or modeling critical aspects of martensitic transformation. The key findings are summarized as follows:

1. The microstructure of the low-carbon as-cast 13Cr-4Ni stainless steel was characterized by a predominant lath martensitic matrix, interspersed with small fraction of delta-ferrite particles (0.94%), non-metallic inclusions (0.03%), and micropores (0.3%).
2. Non-metallic inclusions and micropores were reconstructed in 3D using a multimodal approach, revealing three distinct micropore morphologies, including: gas pores, gas-shrinkage pores, and shrinkage pores.
3. The 3D identification and reconstruction of delta-ferrite particles, facilitated by KAM analysis, revealed two distinct morphologies: (i) elongated particles with faceted interfaces located at PAG boundaries, and (ii) smaller spherical particles with non-faceted interfaces distributed within the interiors of PAGs.
4. The intricate networks of the internal boundaries were analyzed and categorized based on the K-S OR and its associated intervariant misorientations across four primary misorientation angle (θ) ranges, as follows:

    - **5°≤θ<10°:** Three primary morphologies were observed for the sub-block boundaries within this range: (i) small, closed-loop or high-curvature boundary segments, (ii) medium-sized, elongated boundaries with strip-like geometries, and (iii) large, irregular boundaries with porous and tortuous shapes.
    - **10°<θ<23°:** PBs were the most prominent boundaries within this range, particularly those with a misorientation of 14.8°[13 5 1], forming an interconnected network of elongated/high-aspect-ratio boundaries.
    - **23°<θ<45°:** These boundaries were predominantly associated with PAG boundaries or non-K-S boundaries, originating from martensite variants nucleating or halting at original austenite grain boundaries. Additional boundaries were

identified at the interfaces between inclusions and delta-ferrite particles with the martensitic matrix, within this range.

- **45°<θ≤62°:** This range was predominantly characterized by high-angle PBs and BBs, with BBs including Σ3, Σ11, and 60°[011] boundaries, being particularly dominant.

5. Three main types of interactions were observed between the blocks: (i) hard impingement of blocks from distinct packets, (ii) mutual intersection of blocks from different packets, and (iii) interpenetration of sub-blocks/blocks within a single packet. These interactions contributed to the formation of an interlocked martensitic microstructure, leading to inhomogeneous boundary networks with notable morphological and crystallographic complexities.

References

[1] Morito S, Huang X, Furuhara T, Maki T, Hansen N. The morphology and crystallography of lath martensite in alloy steels. Acta Mater 2006;54:5323–31. https://doi.org/10.1016/j.actamat.2006.07.009.

[2] Beladi H, Rohrer GS, Rollett AD, Tari V, Hodgson PD. The distribution of intervariant crystallographic planes in a lath martensite using five macroscopic parameters. Acta Mater 2014;63:86–98. https://doi.org/10.1016/j.actamat.2013.10.010.

[3] Hayashi T, Morito S, Ohba T. Lath and butterfly composite martensite microstructure of a medium-carbon steel and its quantitative evaluation. ISIJ International 2018;58:1524–31. https://doi.org/10.2355/isijinternational.ISIJINT-2018-152.

[4] Trudel A, Lévesque M, Brochu M. Microstructural effects on the fatigue crack growth resistance of a stainless steel CA6NM weld. Eng Fract Mech 2014;115:60–72. https://doi.org/10.1016/j.engfracmech.2013.11.013.

[5] Ghafoori-Ahangar R, Verreman Y. Fatigue behavior of load-carrying cruciform joints with partial penetration fillet welds under three-point bending. Eng Fract Mech 2019;215:211–23. https://doi.org/10.1016/j.engfracmech.2019.05.015.

[6] Sandvik BPJ, Wayman CM. Characteristics of Lath Martensite: Part I. Crystallographic and Substructural Features. n.d.

[7] Kitahara H, Ueji R, Tsuji N, Minamino Y. Crystallographic features of lath martensite in low-carbon steel. Acta Mater 2006;54:1279–88. https://doi.org/10.1016/j.actamat.2005.11.001.

[8] Morito S, Adachi Y, Ohba T. Morphology and crystallography of Sub-blocks in ultra-low carbon lath martensite steel. Mater Trans 2009;50:1919–23. https://doi.org/10.2320/matertrans.MRA2008409.
[9] Mirzaei A, Barrett CD, Ma X, Hodgson PD, Beladi H. On the propensity of lath martensite intervariant boundaries to hydrogen absorption using molecular statics simulation. Materialia (Oxf) 2022;25. https://doi.org/10.1016/j.mtla.2022.101539.
[10] Morito S, Pham AH, Ohba T, Hayashi T, Furuhara T, Miyamoto G. Three-dimensional observations of morphology of low-angle boundaries in ultra-low carbon lath martensite. Microscopy 2017;66:380–7. https://doi.org/10.1093/jmicro/dfx027.
[11] Morito, S., T. Hayashi, T. Ohba, and Y. Adachi. "The relationship between microstructural units and their boundary natures in ultra-low carbon lath martensite." In *Proc. of the 35th Int. Symp. on Mater. Sci., RISÖ DTU, Roskilde, Denmark*, pp. 397-404. 2014.
[12] Beladi H, Tari V, Rohrer GS. On Σ9 grain boundary plane orientation. Materialia (Oxf) 2022;25. https://doi.org/10.1016/j.mtla.2022.101540.
[13] Mirzaei A, Ghaderi R, Hodgson PD, Ma X, Rohrer GS, Beladi H. The influence of parent austenite characteristics on the intervariant boundary network in a lath martensitic steel. J Mater Sci 2022;57:8904–23. https://doi.org/10.1007/s10853-022-07204-w.
[14] Deschênes PA, Wheeler R, Paquet D, Lanteigne J, Serventi AM, Tôn-Thât L, et al. Micromechanical properties of low-carbon martensitic stainless steel by microtensile experiments. Materials Science and Engineering: A 2022;858. https://doi.org/10.1016/j.msea.2022.144030.
[15] Kwak K, Mine Y, Morito S, Ohmura T, Takashima K. Correlation between strength and hardness for substructures of lath martensite in low- and medium-carbon steels. Materials Science and Engineering: A 2022;856. https://doi.org/10.1016/j.msea.2022.144007.
[16] Du C, Hoefnagels JPM, Vaes R, Geers MGD. Block and sub-block boundary strengthening in lath martensite. Scr Mater 2016;116:117–21. https://doi.org/10.1016/j.scriptamat.2016.01.043.
[17] Shibata A, Nagoshi T, Sone M, Morito S, Higo Y. Evaluation of the block boundary and sub-block boundary strengths of ferrous lath martensite using a micro-bending test. Materials Science and Engineering: A 2010;527:7538–44. https://doi.org/10.1016/j.msea.2010.08.026.
[18] Nagao A, Smith CD, Dadfarnia M, Sofronis P, Robertson IM. The role of hydrogen in hydrogen embrittlement fracture of lath martensitic steel. Acta Mater 2012;60:5182–9. https://doi.org/10.1016/j.actamat.2012.06.040.
[19] Deng Y, Liang Y, Zhao F, Xu F, Yang M, Long S. Influence of Microstructure on Tensile Properties and Fatigue Crack Propagation Behavior for Lath Martensitic Steel. Crystals (Basel) 2023;13:1392. https://doi.org/10.3390/cryst13091392.
[20] Zhang Y, Wang S, Xu G, Wang G, Zhao M. Effect of Microstructure on Fatigue-Crack Propagation of 18CrNiMo7-6 High-Strength Steel. Int J Fatigue 2022;163:107027. https://doi.org/10.1016/j.ijfatigue.2022.107027.
[21] Shibata A, Gutierrez-Urrutia I, Nakamura A, Miyamoto G, Madi Y, Besson J, et al. Multi-scale three-dimensional analysis on local arrestability of intergranular crack in high-strength martensitic steel. Acta Mater 2022;234. https://doi.org/10.1016/j.actamat.2022.118053.

[22] Wang C, Qiu H, Kimura Y, Inoue T. Morphology, crystallography, and crack paths of tempered lath martensite in a medium-carbon low-alloy steel. Materials Science and Engineering: A 2016;669:48–57. https://doi.org/10.1016/j.msea.2016.05.041.
[23] Ueki S, Mine Y, Takashima K. Microstructure-sensitive fatigue crack growth in lath martensite of low carbon steel. Materials Science and Engineering: A 2020;773:138830. https://doi.org/10.1016/j.msea.2019.138830.
[24] Ueki S, Mine Y, Lu X, Chiu YL, Bowen P, Takashima K. Effect of geometric lath orientation on fatigue crack propagation via out-of-plane dislocation glide in martensitic steel. Scr Mater 2021;203:114045. https://doi.org/10.1016/j.scriptamat.2021.114045.
[25] Liu T, Xia S, Zhou B, Bai Q, Rohrer GS. Three-dimensional characteristics of the grain boundary networks of conventional and grain boundary engineered 316L stainless steel. Mater Charact 2017;133:60–9. https://doi.org/10.1016/j.matchar.2017.09.026.
[26] Mirzaei A, Barrett CD, Ma X, Hodgson PD, Beladi H. New Insight into Toughness Enhancement in a Lath Martensitic Steel. Metallurgical and Materials Transactions A 2024;55:1409–17. https://doi.org/10.1007/s11661-024-07325-8.
[27] Morsdorf L, Tasan CC, Ponge D, Raabe D. 3D structural and atomic-scale analysis of lath martensite: Effect of the transformation sequence. Acta Mater 2015;95:366–77. https://doi.org/10.1016/j.actamat.2015.05.023.
[28] Thibault D, Bocher P, Thomas M, Lanteigne J, Hovington P, Robichaud P. Reformed austenite transformation during fatigue crack propagation of 13%Cr-4%Ni stainless steel. Materials Science and Engineering: A 2011;528:6519–26. https://doi.org/10.1016/j.msea.2011.04.089.
[29] Stone DJ, Alexandrov BT, Penso JA. Control Of Retained Delta Ferrite In Type 410 Stainless Steel. 2017.
[30] Foroozmehr F, Verreman Y, Chen J, Thibault D, Bocher P. Effect of inclusions on fracture behavior of cast and wrought 13% Cr-4% Ni martensitic stainless steels. Eng Fract Mech 2017;175:262–78. https://doi.org/10.1016/j.engfracmech.2017.02.002.
[31] Furuhara T, Saito H, Miyamoto G, Maki T. Crystallography of ferrite nucleation at austenite grain boundary in a low carbon steel. Materials Science Forum, vol. 654–656, Trans Tech Publications Ltd; 2010, p. 7–10. https://doi.org/10.4028/www.scientific.net/MSF.654-656.7.
[32] Wang P, Lu SP, Xiao NM, Li DZ, Li YY. Effect of delta ferrite on impact properties of low carbon 13Cr-4Ni martensitic stainless steel. Materials Science and Engineering: A 2010;527:3210–6. https://doi.org/10.1016/j.msea.2010.01.085.
[33] Singh J, Nath SK. Improvement in Mechanical Properties and Wear Resistance of 13Cr–4Ni Martensitic Steel by Cyclic Heat Treatment. Transactions of the Indian Institute of Metals 2020;73:2519–28. https://doi.org/10.1007/s12666-020-02043-2.
[34] Meimandi S, Vanderesse N, Thibault D, Bocher P, Viens M. Macro-defects characterization in cast CA-6NM martensitic stainless steel. Mater Charact 2017;124:31–9. https://doi.org/10.1016/j.matchar.2016.11.040.
[35] Melado AC, Nishikawa AS, Goldenstein H, Giles MA, Reed PAS. Effect of microstructure on fatigue behaviour of advanced high strength ductile cast iron produced by quenching and partitioning process. Int J Fatigue 2017;104:397–407. https://doi.org/10.1016/j.ijfatigue.2017.07.009.
[36] Nikulin SA, Rozhnov AB, Rogachev SO, Nechaykina TA, Anikeenko VI, Turilina VYu. Improvement of mechanical properties of large-scale low-carbon steel cast products using

spray quenching. Mater Lett 2016;185:499–502. https://doi.org/10.1016/j.matlet.2016.09.079.
[37] Murata Y. Formation mechanism of lath martensite in steels. Mater Trans 2018;59:151–64. https://doi.org/10.2320/matertrans.M2016430.
[38] Wakasa K, Wayman CM. The morphology and crystallography of ferrous lath martensite. Studies of Fe-20%Ni-5%Mn—I. Optical microscopy. Acta Metallurgica 1981;29:973–90. https://doi.org/10.1016/0001-6160(81)90051-1.
[39] Sarma DS, Whiteman JA, Woodhead JH. Habit plane and morphology of lath martensites. Metal Science 1976;10:391–6. https://doi.org/10.1080/03063453.1976.11683562.
[40] Echlin MP, Burnett TL, Polonsky AT, Pollock TM, Withers PJ. Serial sectioning in the SEM for three dimensional materials science. Curr Opin Solid State Mater Sci 2020;24. https://doi.org/10.1016/j.cossms.2020.100817.
[41] Burnett TL, Kelley R, Winiarski B, Contreras L, Daly M, Gholinia A, et al. Large volume serial section tomography by Xe Plasma FIB dual beam microscopy. Ultramicroscopy 2016;161:119–29. https://doi.org/10.1016/j.ultramic.2015.11.001.
[42] Zankel A, Wagner J, Poelt P. Serial sectioning methods for 3D investigations in materials science. Micron 2014;62:66–78. https://doi.org/10.1016/j.micron.2014.03.002.
[43] Schaffer M, Wagner J, Schaffer B, Schmied M, Mulders H. Automated three-dimensional X-ray analysis using a dual-beam FIB. Ultramicroscopy 2007;107:587–97. https://doi.org/10.1016/j.ultramic.2006.11.007.
[44] DeMott R, Haghdadi N, Kong C, Gandomkar Z, Kenney M, Collins P, et al. 3D electron backscatter diffraction characterization of fine α titanium microstructures: collection, reconstruction, and analysis methods. Ultramicroscopy 2021;230:113394. https://doi.org/10.1016/j.ultramic.2021.113394.
[45] DeMott R, Haghdadi N, Gandomkar Z, Liao X, Ringer S, Primig S. Formation and 3D morphology of interconnected α microstructures in additively manufactured Ti-6Al-4V. Materialia (Oxf) 2021;20. https://doi.org/10.1016/j.mtla.2021.101201.
[46] MANGAN MA, LAUREN PD, SHIFLET GJ. Three-dimensional reconstruction of Widmanstätten plates in Fe–12.3Mn–0.8C. J Microsc 1997;188:36–41. https://doi.org/10.1046/j.1365-2818.1997.2380799.x.
[47] Nishikawa H, Furuya Y, Osada T, Kawagishi K, Hara T. Three-dimensional high-resolution crystallographic observation of the entire volume of microstructurally small fatigue cracks in Ni-Co based superalloy. Scr Mater 2023;222. https://doi.org/10.1016/j.scriptamat.2022.115026.
[48] Singh SS, Loza JJ, Merkle AP, Chawla N. Three dimensional microstructural characterization of nanoscale precipitates in AA7075-T651 by focused ion beam (FIB) tomography. Mater Charact 2016;118:102–11. https://doi.org/10.1016/j.matchar.2016.05.009.
[49] Wirth R. Focused Ion Beam (FIB) combined with SEM and TEM: Advanced analytical tools for studies of chemical composition, microstructure and crystal structure in geomaterials on a nanometre scale. Chem Geol 2009;261:217–29. https://doi.org/10.1016/j.chemgeo.2008.05.019.
[50] Burdet P, Vannod J, Hessler-Wyser A, Rappaz M, Cantoni M. Three-dimensional chemical analysis of laser-welded NiTi–stainless steel wires using a dual-beam FIB. Acta Mater 2013;61:3090–8. https://doi.org/10.1016/j.actamat.2013.01.069.

[51] DeMott R, Collins P, Kong C, Liao X, Ringer S, Primig S. 3D electron backscatter diffraction study of α lath morphology in additively manufactured Ti-6Al-4V. Ultramicroscopy 2020;218. https://doi.org/10.1016/j.ultramic.2020.113073.
[52] Sun Z, Tsai S-P, Konijnenberg P, Wang J-Y, Zaefferer S. A large-volume 3D EBSD study on additively manufactured 316L stainless steel. Scr Mater 2024;238:115723. https://doi.org/10.1016/j.scriptamat.2023.115723.
[53] Ram F, Lloyd JT, Rohrer GS. Habit planes of twins in a deformed Mg alloy determined from three-dimensional microstructure analysis. Mater Charact 2020;159:110014. https://doi.org/10.1016/j.matchar.2019.110014.
[54] Beladi H, Rohrer GS. The relative grain boundary area and energy distributions in a ferritic steel determined from three-dimensional electron backscatter diffraction maps. Acta Mater 2013;61:1404–12. https://doi.org/10.1016/j.actamat.2012.11.017.
[55] Zhong X, Rowenhorst DJ, Beladi H, Rohrer GS. The five-parameter grain boundary curvature distribution in an austenitic and ferritic steel. Acta Mater 2017;123:136–45. https://doi.org/10.1016/j.actamat.2016.10.030.
[56] Beladi H, Nuhfer NT, Rohrer GS. The five-parameter grain boundary character and energy distributions of a fully austenitic high-manganese steel using three dimensional data. Acta Mater 2014;70:281–9. https://doi.org/10.1016/j.actamat.2014.02.038.
[57] McGarrity KS, Sietsma J, Jongbloed G. Characterisation and quantification of microstructural banding in dual-phase steels Part 2 – case study extending to 3D. Materials Science and Technology 2012;28:903–10. https://doi.org/10.1179/1743284712Y.0000000028.
[58] Sato N, Adachi Y, Kawata H, Kaneko K. Topological Approach to Ferrite/Martensite Dual-phase Microstructures. ISIJ International 2012;52:1362–5. https://doi.org/10.2355/isijinternational.52.1362.
[59] Brands D, Balzani D, Scheunemann L, Schröder J, Richter H, Raabe D. Computational modeling of dual-phase steels based on representative three-dimensional microstructures obtained from EBSD data. Archive of Applied Mechanics 2016;86:575–98. https://doi.org/10.1007/s00419-015-1044-1.
[60] Galliopoulou EC, Jones C, Coghlan L, Zimina M, Martin TL, Flewitt PEJ, et al. CREEP CAVITATION IMAGING AND ANALYSIS IN 9%CR 1%MO P91 STEELS 2024. https://doi.org/10.31399/asm.cp.epri2024p0219.
[61] Bobrowski P, Pedzich Z, Faryna M. Three-dimensional microstructural characterization of porous cubic zirconia. Micron 2015;78:73–8. https://doi.org/10.1016/j.micron.2015.07.004.
[62] Medghalchi S, Karimi E, Lee S-H, Berkels B, Kerzel U, Korte-Kerzel S. Three-dimensional characterisation of deformation-induced damage in dual phase steel using deep learning. Mater Des 2023;232:112108. https://doi.org/10.1016/j.matdes.2023.112108.
[63] Polonsky AT, Echlin MP, Lenthe WC, Dehoff RR, Kirka MM, Pollock TM. Defects and 3D structural inhomogeneity in electron beam additively manufactured Inconel 718. Mater Charact 2018;143:171–81. https://doi.org/10.1016/j.matchar.2018.02.020.
[64] Morito S, Pham AH, Hayashi T, Miyamoto G, Furuhara T. Three-dimensional Characterisation of Microstructures in Low-carbon Lath Martensite. ISIJ International 2022;62:1972–80. https://doi.org/10.2355/isijinternational.ISIJINT-2022-157.

[65] Morito S, Yoshida S, Hayamizu R, Hayashi T, Ohba T, Terasaki H, et al. Three-dimensional approach to observing growth of blocks and packets in Fe-18Ni maraging steel. Materials Science Forum, vol. 783–786, Trans Tech Publications Ltd; 2014, p. 916–9. https://doi.org/10.4028/www.scientific.net/msf.783-786.916.
[66] Morito S, Edamatsu Y, Ichinotani K, Ohba T, Hayashi T, Adachi Y, et al. Quantitative analysis of three-dimensional morphology of martensite packets and blocks in iron-carbon-manganese steels. J Alloys Compd 2013;577. https://doi.org/10.1016/j.jallcom.2012.02.004.
[67] Rowenhorst DJ, Gupta A, Feng CR, Spanos G. 3D Crystallographic and morphological analysis of coarse martensite: Combining EBSD and serial sectioning. Scr Mater 2006;55:11–6. https://doi.org/10.1016/j.scriptamat.2005.12.061.
[68] Cayron C. EBSD imaging of orientation relationships and variant groupings in different martensitic alloys and Widmanstätten iron meteorites. Mater Charact 2014;94:93–110. https://doi.org/10.1016/j.matchar.2014.05.015.
[69] Cao S, Wu S, Zhang C, Zhang Q. Three-Dimensional Morphology and Analysis of Widmanstätten Sideplates Ferrite. Metals (Basel) 2022;12:523. https://doi.org/10.3390/met12030523.
[70] Wang K, Feng H, Ling Y, Wan X, Zhou S, Yershov S, et al. Three-dimensional morphology and crystallographic characteristics of the low-temperature bainitic microstructure in high-carbon steel. Vacuum 2023;216. https://doi.org/10.1016/j.vacuum.2023.112465.
[71] Wan XL, Wang HH, Cheng L, Wu KM. The formation mechanisms of interlocked microstructures in low-carbon high-strength steel weld metals. Mater Charact 2012;67:41–51. https://doi.org/10.1016/j.matchar.2012.02.007.
[72] Shibata A, Miyamoto G, Morito S, Nakamura A, Moronaga T, Kitano H, et al. Substructure and crystallography of lath martensite in as-quenched interstitial-free steel and low-carbon steel. Acta Mater 2023;246. https://doi.org/10.1016/j.actamat.2023.118675.
[73] Mosayebi M, Paquet D, Deschênes PA, Tôn-Thât L, Huang B, Bassim N. On the correlation between the habit plane and 3D morphology of lath martensite: A direct 3D observation using serial sectioning tomography of a low-carbon stainless steel. Scr Mater 2025;255. https://doi.org/10.1016/j.scriptamat.2024.116367.
[74] Groeber MA, Jackson MA. Groeber and Jackson Integrating Materials and Manufacturing Innovation. vol. 3. 2014.
[75] Geveci B. ParaView: An End-User Tool for Large Data Visualization. n.d.
[76] He XY, Xu ZP, Rohrer GS, Kong C, Primig S, Haghdadi N. Three-dimensional analysis of the delta-ferrite to austenite phase transformation in an additively manufactured duplex stainless steel. Mater Charact 2025;221:114745. https://doi.org/10.1016/j.matchar.2025.114745.
[77] Pirgazi H. On the alignment of 3D EBSD data collected by serial sectioning technique. Mater Charact 2019;152:223–9. https://doi.org/10.1016/j.matchar.2019.04.026.
[78] Polonsky AT, Lang CA, Kvilekval KG, Latypov MI, Echlin MP, Manjunath BS, et al. Three-dimensional Analysis and Reconstruction of Additively Manufactured Materials in the Cloud-Based BisQue Infrastructure. Integr Mater Manuf Innov 2019;8:37–51. https://doi.org/10.1007/s40192-019-00126-7.

[79] Kelly MN, Glowinski K, Nuhfer NT, Rohrer GS. The five parameter grain boundary character distribution of α-Ti determined from three-dimensional orientation data. Acta Mater 2016;111:22–30. https://doi.org/10.1016/j.actamat.2016.03.029.
[80] Brandon DG. The structure of high-angle grain boundaries. Acta Metallurgica 1966;14:1479–84. https://doi.org/10.1016/0001-6160(66)90168-4.
[81] Niessen F, Nyyssönen T, Gazder AA, Hielscher R. Parent grain reconstruction from partially or fully transformed microstructures in MTEX. J Appl Crystallogr 2022;55:180–94. https://doi.org/10.1107/S1600576721011560.
[82] Chakraborty A, Webster RF, Primig S. Lath martensite substructure evolution in low-carbon microalloyed steels. J Mater Sci 2022;57:10359–78. https://doi.org/10.1007/s10853-022-07275-9.
[83] Torbati-Sarraf H, Sinclair D, Ganju E, Torbati-Sarraf SA, Niverty S, Singaravellu A, et al. Influence of contouring on the microstructure and micromechanical properties of Laser Powder Bed Fusion (LPBF) processed Al6061 enhanced with reactive particles. Mater Charact 2024;215. https://doi.org/10.1016/j.matchar.2024.114206.
[84] Gu C, Lu Y, Luo AA. Three-dimensional visualization and quantification of microporosity in aluminum castings by X-ray micro-computed tomography. J Mater Sci Technol 2021;65:99–107. https://doi.org/10.1016/j.jmst.2020.03.088.
[85] Li Z, Jing Y, Guo H, Sun X, Yu K, Yu A, et al. Study of 3D Pores and Its Relationship with Crack Initiation Factors of Aluminum Alloy Die Castings. Metallurgical and Materials Transactions B 2019;50:1204–12. https://doi.org/10.1007/s11663-019-01550-y.
[86] Liu X, Li Y, Wang J, He Y. The pore growth process and pore coalescence process in Gasar copper. Mater Charact 2018;137:231–43. https://doi.org/10.1016/j.matchar.2018.01.023.
[87] Wan Q, Zhao H, Zou C. Three-dimensional characterization and distribution of micropores in aluminum alloy high pressure die castings. Jinshu Xuebao/Acta Metallurgica Sinica 2013;49:284–90. https://doi.org/10.3724/SP.J.1037.2012.00553.
[88] Rosenauer A, Brandl D, Ressel G, Lukas S, Monschein S, Stockinger M, et al. Influence of delta ferrite on the impact toughness of a PH 13-8 Mo maraging steel. Materials Science and Engineering: A 2022;856. https://doi.org/10.1016/j.msea.2022.144024.
[89] Wu KM, Inagawa Y, Enomoto M. Three-dimensional morphology of ferrite formed in association with inclusions in low-carbon steel. Mater Charact 2004;52:121–7. https://doi.org/10.1016/j.matchar.2004.04.004.
[90] Niessen F, Tiedje NS, Hald J. Kinetics modeling of delta-ferrite formation and retainment during casting of supermartensitic stainless steel. Mater Des 2017;118:138–45. https://doi.org/10.1016/j.matdes.2017.01.026.
[91] Smith CS. Microstructure 1952 Campbell, Edward, Demille Memorial lecture. Transactions of the American Society for Metals 1953;45:533–75.
[92] Yin J, Hillert M, Borgenstam A. Morphology of Proeutectoid Ferrite. Metall Mater Trans A Phys Metall Mater Sci 2017;48:1425–43. https://doi.org/10.1007/s11661-016-3903-y.
[93] Furuhara T, Saito H, Miyamoto G, Maki T. Crystallography of ferrite nucleation at austenite grain boundary in a low carbon steel. Materials Science Forum, vol. 654–656, Trans Tech Publications Ltd; 2010, p. 7–10. https://doi.org/10.4028/www.scientific.net/MSF.654-656.7.

[94] Karthikeyan T, Dash MK, Saroja S, Vijayalakshmi M. Estimation of martensite feature size in a low-carbon alloy steel by microtexture analysis of boundaries. Micron 2015;68:77–90. https://doi.org/10.1016/j.micron.2014.09.008.
[95] Lv Z, Zhang X, Huang X, Hansen N. EBSD characterization of deformed lath martensite in IF steel. IOP Conf Ser Mater Sci Eng 2017;219:012033. https://doi.org/10.1088/1757-899X/219/1/012033.
[96] Archie F, Mughal MZ, Sebastiani M, Bemporad E, Zaefferer S. Anisotropic distribution of the micro residual stresses in lath martensite revealed by FIB ring-core milling technique. Acta Mater 2018;150:327–38. https://doi.org/10.1016/j.actamat.2018.03.030.
[97] Hajra RN, Dash MK, Chu W, Singh AN, Nam K-W, Kim JH. High-temperature phase stability, $\gamma \rightarrow \delta$ transformation of ferritic/martensitic steel studied by differential scanning calorimetry and electron backscatter diffraction. J Therm Anal Calorim 2023;148:3357–71. https://doi.org/10.1007/s10973-023-11979-8.
[98] Tian Q, Xu X, Li J, Liu N, Wu X, Shen P, et al. Formation Mechanism of Band Delta-Ferrite in 416 Stainless Steel and Its Relationship with MnS and M23C6. Metallurgical and Materials Transactions B 2021;52:2355–63. https://doi.org/10.1007/s11663-021-02181-y.
[99] Warke VS, Sisson RD, Makhlouf MM. The effect of porosity on the austenite to bainite transformation in powder metallurgy steels. J Mater Res 2009;24:3213–9. https://doi.org/10.1557/jmr.2009.0379.
[100] Javanbakht M, Ghaedi MS, Barchiesi E, Ciallella A. The effect of a pre-existing nanovoid on martensite formation and interface propagation: a phase field study. Mathematics and Mechanics of Solids 2021;26:90–109. https://doi.org/10.1177/1081286520948118.
[101] Shen Y, Wang C. In Situ Observation of Martensite Lath Growth Behaviors in the Coarse Grained Heat-Affected Zone of 1.25Cr-0.5Mo Heat-Resistant Steel During Simulated Welding. Metallurgical and Materials Transactions A 2019;50:4955–60. https://doi.org/10.1007/s11661-019-05420-9.
[102] Miyamoto G, Iwata N, Takayama N, Furuhara T. Quantitative analysis of variant selection in ausformed lath martensite. Acta Mater 2012;60:1139–48. https://doi.org/10.1016/j.actamat.2011.11.018.
[103] Miyamoto G, Iwata N, Takayama N, Furuhara T. Variant selection of lath martensite and bainite transformation in low carbon steel by ausforming. J Alloys Compd 2013;577:S528–32. https://doi.org/10.1016/j.jallcom.2011.12.111.

Chapter 3

Three-dimensional analysis of local and dominant habit planes in a lath martensitic stainless steel

Complete Citation:

Mehdi Mosayebi, Pierre-Antony Deschênes, Daniel Paquet, Laurent Tôn-Thât, and Nabil Bassim. "Three-dimensional analysis of local and dominant habit planes in a lath martensitic stainless steel." Under review by Materialia. http://dx.doi.org/10.2139/ssrn.5193961.

Three-dimensional analysis of local and dominant habit planes in a lath martensitic stainless steel

Mehdi Mosayebi[1,3], Pierre-Antony Deschênes[2], Daniel Paquet[2], Laurent Tôn-Thât[2], Nabil Bassim[1,3,*]

[1] Department of Materials Science and Engineering, McMaster University, Hamilton, ON, Canada.
[2] Hydro Quebec Research Institute (IREQ), Varennes, QC, Canada.
[3] Canadian Centre for Electron Microscopy, McMaster University, Hamilton, ON, Canada.

Abstract

The three-dimensional (3D) morphology of lath martensite in a low-carbon 13Cr–4Ni stainless steel (CA6NM alloy) was reconstructed using large-volume Xe^+ plasma focused ion beam (PFIB) serial sectioning tomography in combination with electron backscatter diffraction (EBSD). This approach enabled a detailed analysis of both dominant and local habit planes (HPs), offering new insights into their spatial distribution and variation. The dominant HP, determined by averaging the normal directions of high-angle block boundaries (BBs) within packets and across multiple prior austenite grains (PAGs), was found to lie between {111}γ and {557}γ, with an orientation of (0.51,0.52,0.66)γ. However, local HP analysis at individual BBs revealed significant deviations from both orientations in certain regions of the microstructure. 3D morphological observations indicated that bending within specific blocks directly contributed to these local HP variations. It is suggested that interactions between adjacent growing blocks, whether through spatial interference and growth competition within a single packet, or hard impingement between blocks from different packets, affect growth paths, ultimately leading to block bending and the macroscopic deflection of interface planes. These findings highlight the intricate interplay between microstructural evolution and crystallographic constraints during martensitic transformation, demonstrating the effectiveness of large-scale 3D characterization in capturing complex microstructural phenomena that are difficult to resolve through conventional 2D analyses.

Keywords: 3D electron backscatter diffraction, plasma focused ion beam, lath martensite, habit plane

3.1 Introduction

Ferrous martensite exhibits a diverse range of morphologies, primarily influenced by carbon content [1,2]. Among them, lath martensite, characteristic of low-carbon steels (0.01–0.3 wt.% C), is of particular industrial significance due to its exceptional combination of high strength, toughness, and weldability [3-5]. The formation of lath martensite in low-carbon steels follow the Kurdjumov-Sachs (K–S) orientation relationship (OR), wherein a single austenite (γ) grain transforms into 24 crystallographically distinct variants (V1–V24), dictated by the symmetry of the cubic system [4,6]. These variants are organized into four packets, each corresponding to a close-packed {111}γ plane of the face-centered cubic (FCC) structure. Within each packet, six K–S variants pair to form blocks, larger structural domains that share common habit planes (HPs) [7-9].

According to the phenomenological theory of martensite (PTM), HPs remain macroscopically invariant during martensitic lattice rearrangement, minimizing macro strain at domain interfaces and at the parent/martensite boundaries [10-12]. Analyzing the crystallography of HPs and interfaces can therefore provide key insights into the mechanisms governing martensitic transformation and shear strain accommodation. HPs are conventionally defined by 3D orientation of the martensitic plates in the austenite reference frame, making it difficult to characterize directly using 2D imaging techniques, as the inclination angle of the HP relative to the specimen surface is not directly available [11,13-16]. Early studies [17-19] employed the “two-surface technique” which relied on stereological analysis of martensite plates in large prior austenite grains (PAGs) observed from two intersecting surfaces. Another widely used approach, transmission electron microscope (TEM) trace analysis [19,20], involves determining HP indices using a series of images, including micrographs and diffraction patterns from different areas. Both methods,

however, have limitations, requiring complex specimen preparation, reliance on retained austenite, and yielding poor statistical reliability.

Recently, 3D characterization techniques have demonstrated significant potential in providing critical insights into the morphology and crystallography of complex microstructures. When high spatial resolution (~ tens of nanometers) is required, focused ion beam (FIB) serial sectioning tomography has proven effective in generating sequential 2D images that can be reconstructed into a 3D dataset [21-23]. However, conventional Ga^+ FIB systems are constrained by slow milling rates, limiting the volume that can be analyzed within a reasonable timeframe, particularly when acquiring crystallographic or compositional data. In contrast, Xe^+ plasma FIB (PFIB) enables significantly faster milling rates, allowing for the reconstruction of a sufficiently large volume to be representative of the bulk material's behavior while maintaining the spatial resolution necessary to capture key microstructural features [24,25]. When combined with advanced analytical techniques such as electron backscatter diffraction (EBSD), PFIB tomography enables the simultaneous acquisition of morphological, spatial, and crystallographic information in 3D [26-29]. This capability allows for the full identification of real-space features such as facets, interface planes, and HPs. For instance, Motomura et al. [16] utilized 3D reconstructed images of a Cu–17Al–11Mn (at.%) alloy for HP trace analysis of bainite. In the case of lath martensite, Rowenhorst et al. [23,30] and Morito et al. [31-34] applied FIB tomography to various martensitic steels to investigate the crystallography of facets and boundary planes using crystallographic interface normal distribution (CIND) analysis. Despite these advances, most studies have primarily focused on small to mid-sized structural units, such as facets on a single lath crystal [23], or individual block and sub-block boundaries within a packet [34]. As a result, the larger-scale 3D distribution and variation of crystallographic interfaces within the hierarchical structure of lath martensite

remain insufficiently explored. This is particularly relevant for low–carbon steels, where prior austenite grains (PAGs) can reach hundreds of microns in size, resulting in coarser martensitic features and larger interfaces in 3D [14,33,35]. Additionally, many previous studies have predominantly quantified interface boundary plane orientations using frequency histograms [1,23,34], leaving gaps in understanding the possible correlations between microstructural morphology and the crystallographic variation of 3D interfaces.

In this study, we employ large-volume 3D EBSD analysis to reconstruct the lath martensitic structure and demonstrate its application in directly measuring both dominant (i.e., average) and local HPs in a low-carbon stainless steel. Utilizing a combination of Xe^+ PFIB tomography and EBSD techniques, we visualize, for the first time ,the large-scale 3D distribution and variation of local HPs within the microstructural volume using 3D orientation maps. These results establish key correlations between local HP variations, martensitic feature morphology, and block interactions, providing new insights into the complex microstructural evolution of lath martensite.

3.2 Experimental

The material used in this study is the CA6NM alloy, a low-carbon martensitic stainless steel with an average prior austenite grain (PAG) size of 158.1 μm, widely utilized in the hydroelectric industry [36]. The experimental procedure closely follows our previous 3D EBSD study on this material [14], ensuring consistency in data acquisition and analysis. A volume of 140 × 140 × 90 μm^3 (X, Y, Z) was extracted from a 10 mm × 10 mm × 4 mm specimen for serial sectioning using a dual-beam TFS Helios G5 Xe PFIB system. Sectioning and EBSD scans were conducted using the Auto-Slice-and-View software under the following conditions. The slice thickness was set to 250 nm, with EBSD scans collected every other slice, resulting in a final Z-resolution of 500 nm.

A slicing current of 0.2 μA was used, and a 5° rocking mill was applied to minimize curtaining effects. 2D EBSD maps were acquired at 20 keV with a current of 13 nA, using an Oxford Symmetry detector and the Aztec control software. The EBSD camera chip was configured with 4 × 4 binning, maintaining an indexing rate above 90%. A total of 180 slices were collected, with each EBSD map indexing the entire sample face (X–Y planes) at a 500 nm step size, ensuring cubic voxel representation. While this resolution does not resolve individual martensitic laths, larger microstructural units such as sub-blocks, blocks, packets, and PAGs were readily identifiable. Reconstruction steps, including data importation, thresholding, alignment, clean-up, and segmentation, were performed using DREAM.3D software [37] with a misorientation tolerance of 2°. The 3D volume was cropped into a neat rectangular prism of 130 × 120 × 75 μm³ to create smooth edges and facilitate visual inspection. Internal misorientation gradients were analyzed using 3D kernel averaging with a kernel volume of 2 × 2 × 2 μm³. Following reconstruction and segmentation, the final 3D dataset was visualized using ParaView software [38].

3.3 Results and discussion

3.3.1 Average/dominant habit plane of the 3D microstructure

Figures 3.1(a, b) present the 3D volume reconstructed from the PFIB–EBSD experiment, revealing the characteristic lath martensitic structure. To elucidate its hierarchical morphology and crystallography, PAGs, their close-packed (CP) $\{111\}_\gamma$ planes, and the distribution of K–S variants were identified using 2D orientation maps extracted from different depths of the 3D dataset. This reconstruction was performed using MTEX and a MATLAB code originally developed by Niessen et al. [39], generating 2D PAG maps, CP maps, and K–S variant maps, as illustrated in Figures 3.2(a1–a4) and 3.2(b1–b4) for slices 150 and 50, respectively. Three distinct PAGs (PAG1–PAG3)

are partially captured within the dataset, with their boundaries marked by black dashed lines. These 2D reconstructions were served as reference points for subsequent segmentation and reconstruction of these martensitic features in 3D. Using 25 individual slices spaced at 3 µm intervals, each feature of the 3D microstructure was assigned to one of the three PAGs and further classified into one of the four CP groups (CP1–CP4), as depicted in Figure 3.3(a–c).

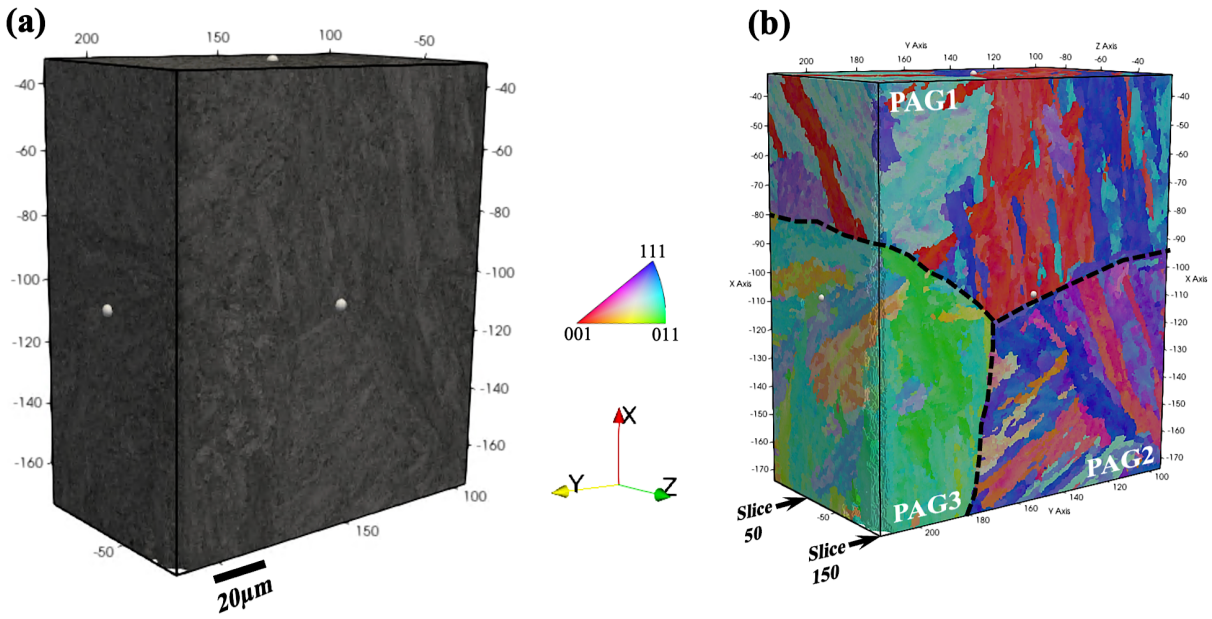

Figure 3.1: (a, b) 3D reconstruction of the martensitic microstructure presented as band contrast (BC) and inverse pole figure (IPF) maps, respectively. In (b), the black dashed lines indicate prior austenite grain (PAG) boundaries, and the orientation map is color-coded with respect to the Z direction of the sample reference frame (i.e. IPF-Z), where Z is parallel to the slicing direction.

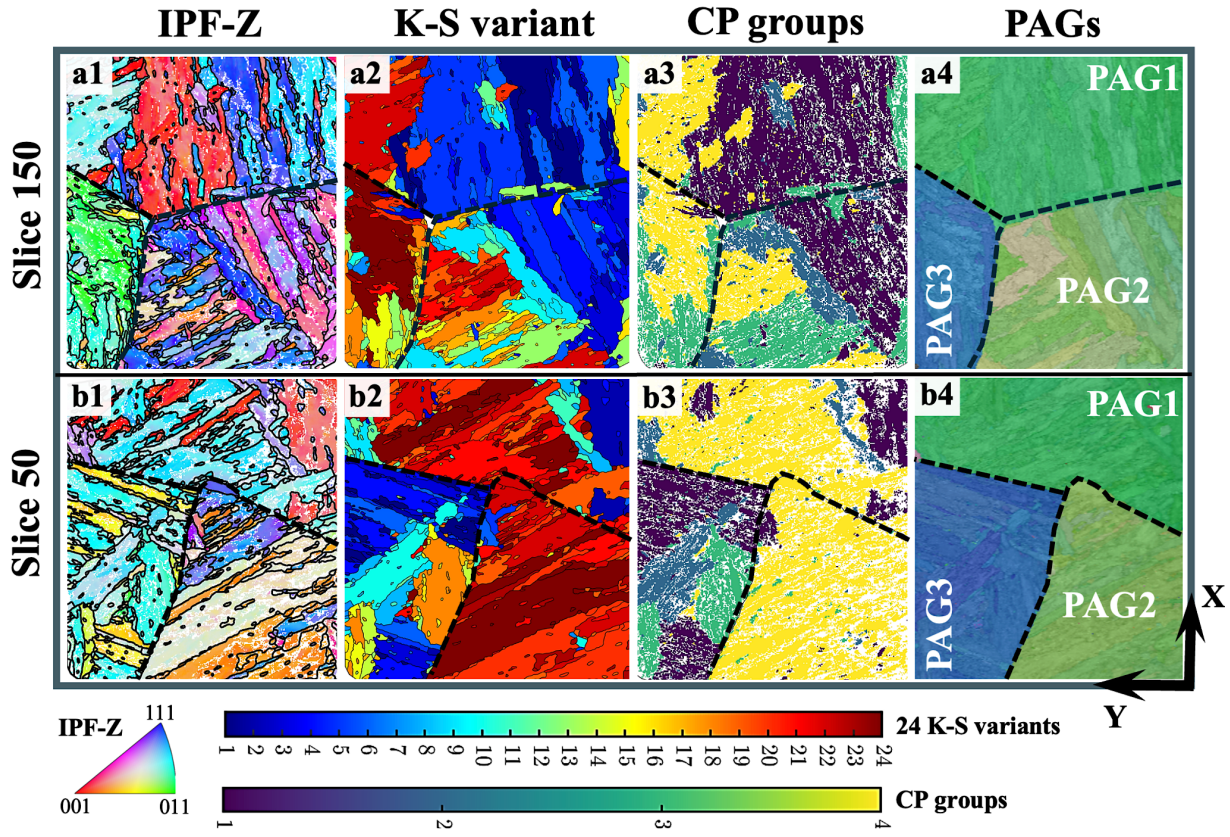

Figure 3.2: 2D IPF-Z, K-S variant, CP, and PAG maps for slices 150 **(a1-a4)** and 50 **(b1-b4)**; CP1-CP4 correspond to (111), $(1\bar{1}1)$, $(\bar{1}11)$, and $(11\bar{1})$ close-packed planes. The approximate position of slices 150 and 50 are shown in Fig.3.1(b).

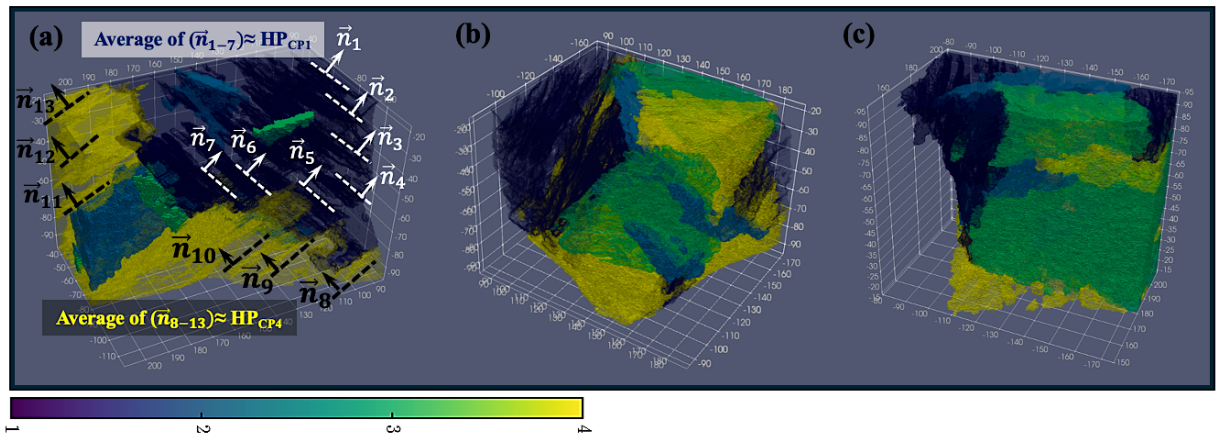

Figure 3.3: 3D reconstructions of PAG1 **(a)**, PAG2 **(b)**, and PAG3 **(c)**, with packets color-coded using CP maps in Figs.2(a3, b3). $\vec{n}_{1-7}$ and $\vec{n}_{8-13}$ represent block surface normals in CP1 and CP4 in PAG1.

Although none of the PAGs are fully enclosed within the dataset (i.e., all appear truncated), the large-volume 3D EBSD dataset successfully captures all four CP groups and most of their corresponding blocks across the three PAGs. As evident, packets exhibit anisotropic shapes with varying spatial orientations and consist of stacks of parallel blocks sharing the same HPs. With the exact 3D shape and spatial orientation of each packet, the index of these HPs can be determined by averaging the normal directions (NDs) of block surfaces or, equivalently, by averaging the NDs of the interfaces between the stacked parallel blocks within each packet, as schematically illustrated for CP1 and CP4 of PAG1 in Figure 3.3(a). To achieve this, a triangular mesh of the internal boundaries was generated using the Quick Surface Mesh filter in DREAM.3D, followed by smoothing with a Laplacian algorithm, employing 100 iterations with a weighting factor of 0.05, to eliminate the terrace-step geometry introduced by the cubic voxel structure (Figure 3.4(a–c)). Since each triangle in this boundary mesh contains detailed information about the orientations of the adjacent features (e.g. disorientation across the triangle, centroid coordinates, and normal vectors), individual boundaries between the parallel blocks (i.e. the high-angle block boundaries (BBs)) within each packet can be identified and reconstructed while their local and average normal directions (NDs) can also be determined within the sample reference frame (X–Y–Z). Figures 3.4(a–c) illustrate the 3D network of high-angle BBs, with the color-code in Figure 3.4(a) representing the ND at each voxel relative to the Z direction of the sample reference frame (i.e., IPF-Z). Since ND varies locally along the BB surfaces, both local and average NDs can be considered for analysis. Here, average NDs were used to determine the average HP of each packet and, consequently, the dominant HP of the entire microstructure (Figure 3.6), while local NDs were analyzed to assess variations in local HPs within the 3D microstructure (Figure 3.7). To ensure comparability between these HPs and literature values, they were first transformed from

the sample reference frame (X–Y–Z) into the crystallographic coordinate system of the PAGs (i.e., the austenite reference frame, representing the FCC austenite grains before transformation into martensite). The crystallographic coordinate systems of PAG1–PAG3 were determined from the reconstructed PAG maps generated by MTEX (Figures 3.2(a4, b4)) and expressed as average Euler angles ⟨φ1, Φ, φ2⟩, reflecting the original 3D orientations of FCC crystals within each PAG (Figures 3.5). These Euler angles were then converted into transformation matrices g1–g3 (corresponding to PAG1–PAG3, respectively) using the following formula [18]:

$$g = \begin{bmatrix} \cos\varphi_1 \cos\varphi_2 - \sin\varphi_1 \sin\varphi_2 \cos\Phi & \sin\varphi_1 \cos\varphi_2 + \cos\varphi_1 \sin\varphi_2 \cos\Phi & \sin\varphi_2 \sin\Phi \\ -\cos\varphi_1 \sin\varphi_2 - \sin\varphi_1 \cos\varphi_2 \cos\Phi & -\sin\varphi_1 \sin\varphi_2 + \cos\varphi_1 \cos\varphi_2 \cos\Phi & \cos\varphi_2 \sin\Phi \\ \sin\varphi_1 \sin\Phi & -\cos\varphi_1 \sin\Phi & \cos\Phi \end{bmatrix}$$

The transformation matrices were then applied to convert the NDs in Figure 3.4(a) from the sample coordinate system to their corresponding crystal coordinate system. Figure 3.6 presents the average HP of each packet within PAG1-PAG3 (shown as transparent triangles), along with their deviation from the theoretical K–S HP$\{111\}\gamma$, denoted as $\Delta\Theta_{CP}^{\{111\}\gamma}$. As shown, the average HPs of packets across all three PAGs exhibit angular deviations from $\{111\}\gamma$ HPs, ranging from 1.5° to 12.3°. Interestingly, the overall average $\Delta\Theta_{CP}^{\{111\}\gamma}$ across all packets in Figure 3.6 was calculated as 6.6°±3.5°, corresponding to the average HP of (0.51,0.52,0.66)γ, which closely matches the commonly reported $\{557\}\gamma$ HPs (only 2.5° difference) [19,20,40]. This result highlights the accuracy of this method in directly determining the dominant HP of the microstructure, showing strong agreement with previous studies.

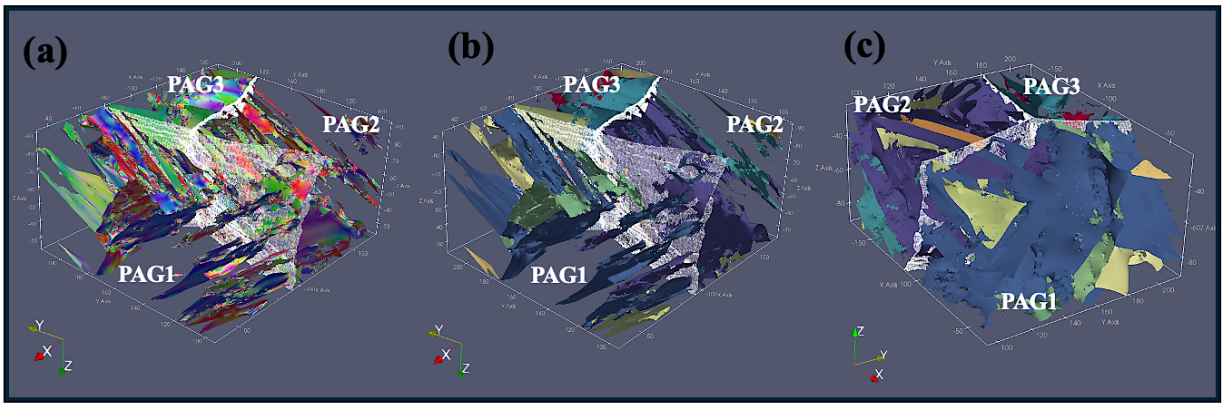

Figure 3.4: (a-c) 3D network of high-angle BBs; (a) color-coded by boundary normals in the sample coordinate system (IPF-Z), (b, c) individual BBs shown with random colors from two different views. PAG boundaries are also illustrated with transparent white in a-c.

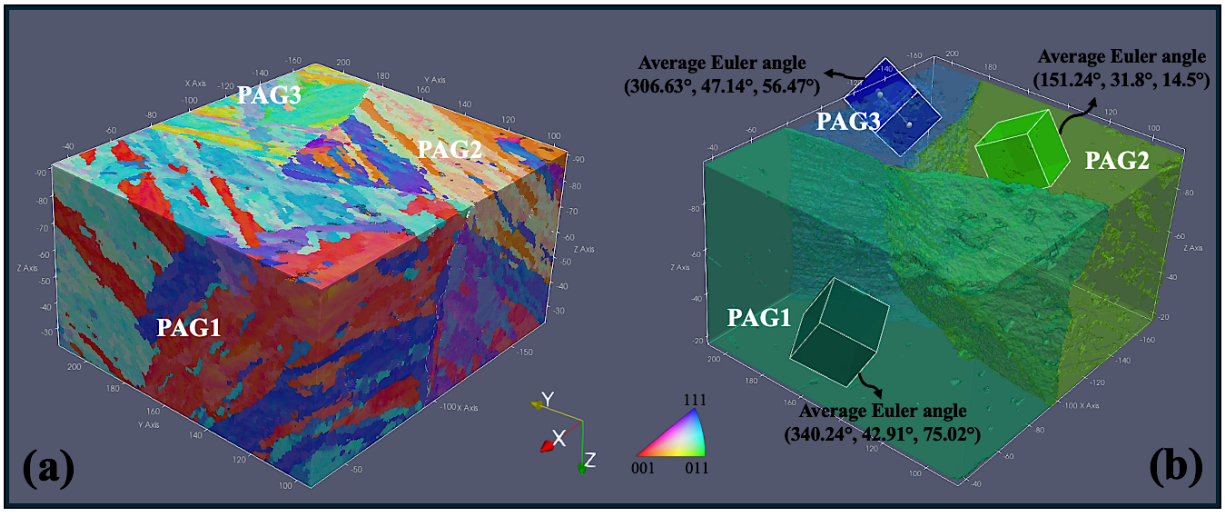

Figure 3.5: (a, b) 3D IPF-Z maps demonstrating the martensitic structure (a) and its PAGs (b), color-coded using PAG maps in **Figs.3.2(a4, b4).** The average Euler angles $<\varphi_1 , \Phi , \varphi_2>$ and 3D orientations of FCC crystals within PAGs are also presented in (e).

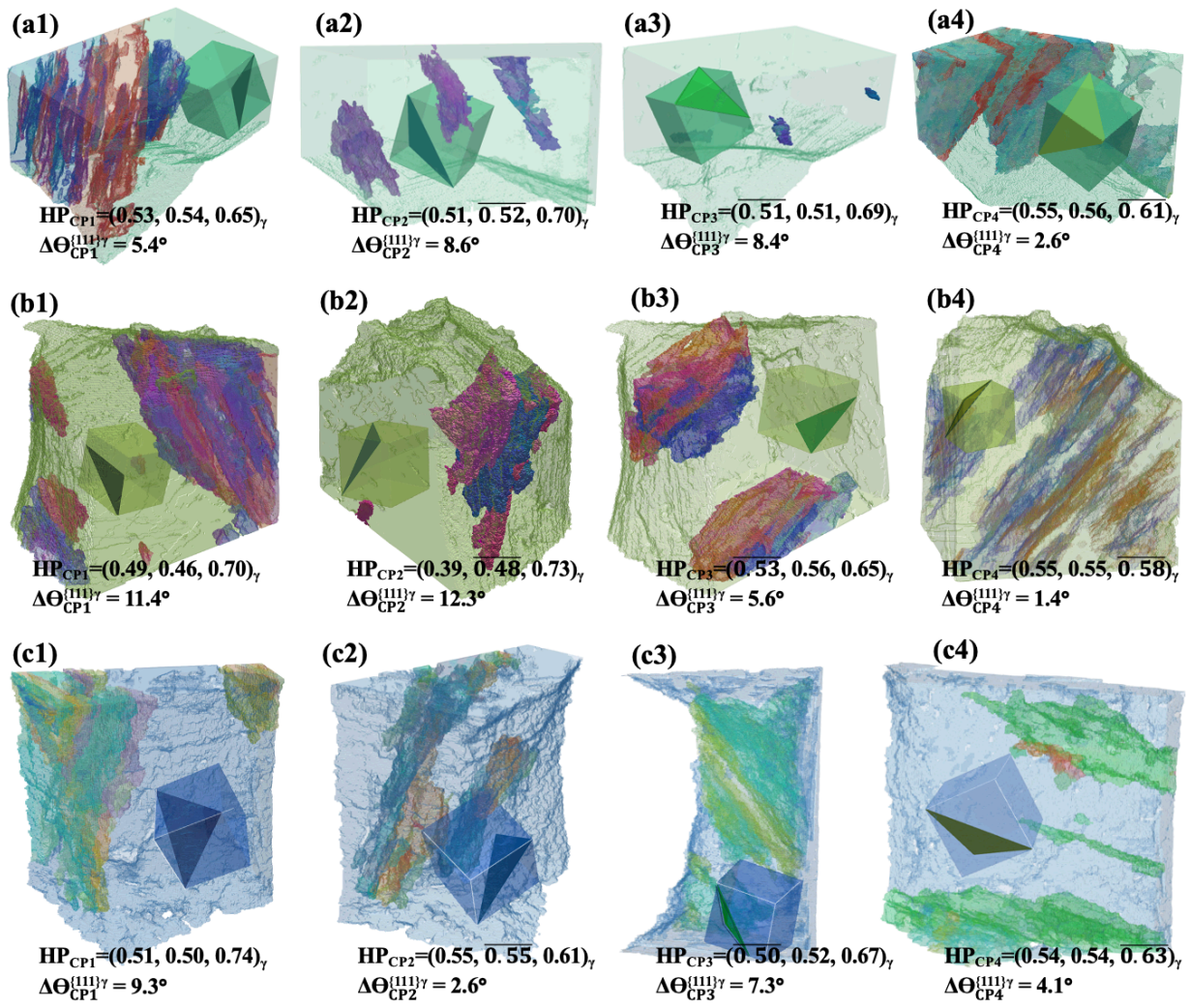

Figure 3.6: Average habit plane (HP) of CP1-CP4 within PAG1 **(a1-a4)**, PAG2 **(b1-b4)**, and PAG3 **(c1-c4)**, shown as transparent triangles in the austenite reference frame. The angular difference between the average HP of CPs and the theoretical K-S HP $\{111\}_\gamma$ is denoted as $\Delta\Theta_{CP}^{\{111\}\gamma}$. The transparent FCC crystals within PAGs are the same as in Fig.3.5(b).

3.3.2 Local habit planes within the 3D microstructure

While the average HP of packets falls between $\{111\}_\gamma$ and $\{557\}_\gamma$, with a tendency toward $\{557\}_\gamma$, analysis of local HPs at individual BBs in Figure 3.7 reveals significant deviations from both $\{111\}_\gamma$ and $\{557\}_\gamma$ in certain regions of the 3D microstructure. Figures 3.7(c, d) illustrate these deviations, color-coded based on the angular difference between the local HP and the theoretical K–S HP $\{111\}_\gamma$. While most regions show deviations of less than ~ 10° from $\{111\}\gamma$,

some BBs or portions of BBs exhibit larger deviations of up to ~ 18.5°, as highlighted in white dashed boxes I, II and III in Figures 3.7(c, d). Note that the angular deviation of $\{557\}_\gamma$ from $\{111\}_\gamma$ is only 9.5°. The average HP index of the regions corresponding to the maximum of ~18.5° was calculated to be $(0.42, 0.38, 0.77)_\gamma$, which is only 1.9° away from $\{112\}_\gamma$, one of the less commonly reported HPs for lath martensite [17,20]. Consistent with this, Yeddu et al. [41] predicted through modelling that an infinitesimally small martensite unit rotates away from the initial $\{111\}_\gamma$ HP toward $\{112\}_\gamma$ to minimize Gibbs free energy during martensitic transformation in an Fe–17% Cr–7% Ni alloy. Similarly, Galindo-Nava [42] used a mathematical theory of shear transformations to predict four distinct local HPs for lath martensite, linking them to the macroscopic HP of $\{557\}\gamma$.

Examination of the 3D morphology of blocks within these regions in Figures 3.7(a, b) shows that significant bending in certain blocks directly contributes to the observed local HP deviations. This behavior can be attributed to the interactions between adjacent growing blocks, either through spatial interference and growth competition within a single packet (e.g., white dashed lines in Figures 3.7(a, b)) or hard impingement between blocks from different packets (e.g., white and black arrows in Figures 3.7(a, b)) [43]. These interactions, particularly evident in high KAM regions in Figures 3.7(e, f), can alter growth paths, causing block bending and macroscopic deflection of interface planes, leading to deviations from their ideal HPs [44,45]. Another possible factor contributing to these local HP variations is matrix-embedded distortions, i.e., the local distortion and rotation of the surrounding FCC matrix during martensite nucleation and growth. Cayron [46] and Thome et al. [47] investigated this phenomenon, observing a gradient/continuum of ORs between Pitsch, Nishiyama-Wasserman (N–W), and K–S within martensitic laths in low-carbon steels. Their findings suggest that the final orientation and HP of each martensite crystal are not solely determined by a single most favorable OR but rather emerge from multiple locally

forming ORs. Consequently, the OR detected in a given region depends on the specific sampling location, which aligns with the experimental observations in this study.

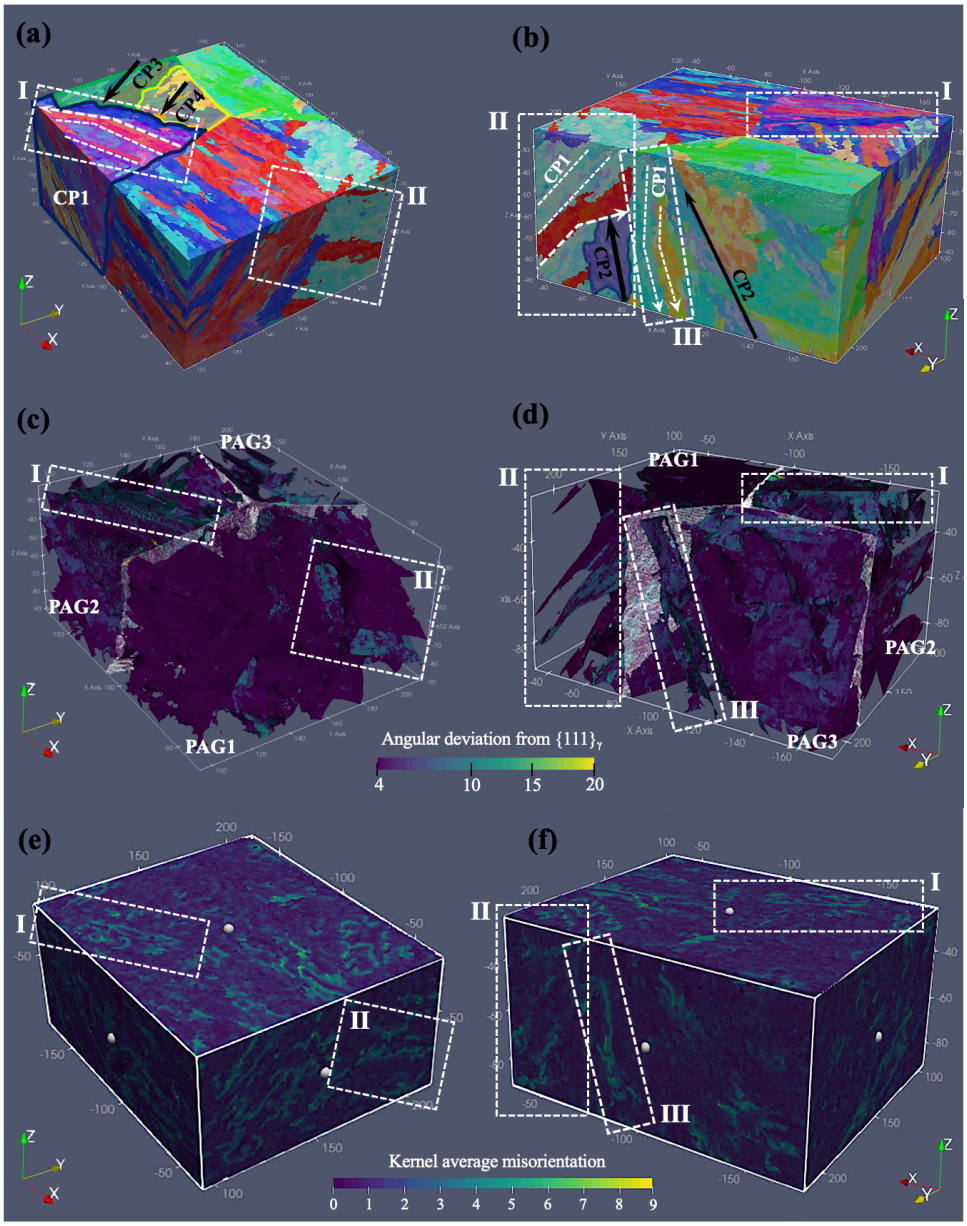

Figure 3.7: Two different views of the 3D microstructure: **(a, b)** IPF-Z maps highlighting block morphology within regions I, II and III, **(c, d)** 3D high-angle BB network, color-coded by the angular difference between the local HP and the theoretical K-S HP $\{111\}_{\gamma}$, and **(e, f)** 3D kernel average misorientation (KAM) maps corresponding to the IPF-Z maps in (a, b). Note that (a, c, e) share the same 3D view, while (b, d, f) share another common 3D view.

3.4 Conclusions

This study demonstrated the application of large-volume 3D EBSD for reconstructing the 3D morphology of lath martensite and analyzing both dominant and local HPs in a lath martensitic stainless steel. The dominant HP was found to be close to {557}γ, while local HPs exhibited deviations, with some regions shifting toward {112}γ. These variations were primarily attributed to block bending caused by interactions between adjacent blocks, including spatial interference and growth competition within a single packet and hard impingement between blocks from different packets. The results align well with previous experimental and modeling studies while providing improved statistical reliability and spatial resolution. This study underscores the importance of large-scale 3D characterization in capturing habit plane variations and their underlying microstructural mechanisms, offering new insights into the complex nature of lath martensite transformation.

Acknowledgements

The authors express their gratitude to the Natural Sciences and Engineering Research Council of Canada (NSERC) and MITACS for their financial support of this project. The authors would also like to thank the staff of the Canadian Centre for Electron Microscopy (CCEM) for their technical assistance.

References

[1] H. Beladi, N.T. Nuhfer, G.S. Rohrer, The five-parameter grain boundary character and energy distributions of a fully austenitic high-manganese steel using three dimensional data, Acta Mater 70 (2014) 281–289. https://doi.org/10.1016/j.actamat.2014.02.038.

[2] T. Hayashi, S. Morito, T. Ohba, Lath and butterfly composite martensite microstructure of a medium-carbon steel and its quantitative evaluation, ISIJ International 58 (2018) 1524–1531. https://doi.org/10.2355/isijinternational.ISIJINT-2018-152.

[3] H. Beladi, G.S. Rohrer, A.D. Rollett, V. Tari, P.D. Hodgson, The distribution of intervariant crystallographic planes in a lath martensite using five macroscopic parameters, Acta Mater 63 (2014) 86–98. https://doi.org/10.1016/j.actamat.2013.10.010.
[4] S. Morito, X. Huang, T. Furuhara, T. Maki, N. Hansen, The morphology and crystallography of lath martensite in alloy steels, Acta Mater 54 (2006) 5323–5331. https://doi.org/10.1016/j.actamat.2006.07.009.
[5] A. Trudel, M. Lévesque, M. Brochu, Microstructural effects on the fatigue crack growth resistance of a stainless steel CA6NM weld, Eng Fract Mech 115 (2014) 60–72. https://doi.org/10.1016/j.engfracmech.2013.11.013.
[6] H. Kitahara, R. Ueji, N. Tsuji, Y. Minamino, Crystallographic features of lath martensite in low-carbon steel, Acta Mater 54 (2006) 1279–1288. https://doi.org/10.1016/j.actamat.2005.11.001.
[7] A. Chakraborty, R.F. Webster, S. Primig, Lath martensite substructure evolution in low-carbon microalloyed steels, J Mater Sci 57 (2022) 10359–10378. https://doi.org/10.1007/s10853-022-07275-9.
[8] Y. Murata, Formation mechanism of lath martensite in steels, Mater Trans 59 (2018) 151–164. https://doi.org/10.2320/matertrans.M2016430.
[9] B.P.J. Sandvik, C.M. Wayman, Characteristics of Lath Martensite: Part I. Crystallographic and Substructural Features, n.d.
[10] D.S. Sarma, J.A. Whiteman, J.H. Woodhead, Habit plane and morphology of lath martensites, Metal Science 10 (1976) 391–396. https://doi.org/10.1080/03063453.1976.11683562.
[11] T. Nyyssönen, A.A. Gazder, R. Hielscher, F. Niessen, Habit plane determination from reconstructed parent phase orientation maps, Acta Mater 255 (2023). https://doi.org/10.1016/j.actamat.2023.119035.
[12] C. Cayron, A. Baur, R. Logé, A crystallographic model of the {557} habit planes in low-carbon martensitic steels, n.d.
[13] F. Ram, J.T. Lloyd, G.S. Rohrer, Habit planes of twins in a deformed Mg alloy determined from three-dimensional microstructure analysis, Mater Charact 159 (2020) 110014. https://doi.org/10.1016/j.matchar.2019.110014.
[14] M. Mosayebi, D. Paquet, P.A. Deschênes, L. Tôn-Thât, B. Huang, N. Bassim, On the correlation between the habit plane and 3D morphology of lath martensite: A direct 3D observation using serial sectioning tomography of a low-carbon stainless steel, Scr Mater 255 (2025). https://doi.org/10.1016/j.scriptamat.2024.116367.
[15] L. Wang, G. Cheng, T. Liu, J. Yang, M. Deng, H. Huang, L. Ding, Y. Ma, Y. Tan, Exploring on Stereo Morphology and Habit Plane of Martensite in Ferrous Alloy, in: IOP Conf Ser Mater Sci Eng, Institute of Physics Publishing, 2018. https://doi.org/10.1088/1757-899X/381/1/012168.
[16] S. Motomura, T. Hara, T. Omori, R. Kainuma, M. Nishida, Morphological and chemical analysis of bainite in Cu-17Al-11Mn (At.%) alloys by using orthogonal FIB-SEM and double-EDS STEM, Microscopy 65 (2016) 243–252. https://doi.org/10.1093/jmicro/dfw003.
[17] H.H. Wills, H.W. Frohlich Heitler, A.B. Greninger Alexander R Troiano, Orientation Habit of Martensite, 1935.
[18] X. Feng, J. Xie, W. Kuang, A novel approach to index site-specific grain boundary plane, Mater Charact 174 (2021). https://doi.org/10.1016/j.matchar.2021.110999.

[19] M. Sugiyama, M. Takei, S. Sekida, N. Maruyama, Characterization of hierarchical lath martensite microstructure in low carbon steels using ultra-high voltage TEM and SEM-EBSD analysis, IOP Conf Ser Mater Sci Eng 1249 (2022) 012020. https://doi.org/10.1088/1757-899x/1249/1/012020.
[20] C. Cayron, A. Baur, R. Logé, Intricate morphologies of laths and blocks in low-carbon martensitic steels, Mater Des 154 (2018) 81–95. https://doi.org/10.1016/j.matdes.2018.05.033.
[21] A. Zankel, J. Wagner, P. Poelt, Serial sectioning methods for 3D investigations in materials science, Micron 62 (2014) 66–78. https://doi.org/10.1016/j.micron.2014.03.002.
[22] M.P. Echlin, T.L. Burnett, A.T. Polonsky, T.M. Pollock, P.J. Withers, Serial sectioning in the SEM for three dimensional materials science, Curr Opin Solid State Mater Sci 24 (2020). https://doi.org/10.1016/j.cossms.2020.100817.
[23] D.J. Rowenhorst, A. Gupta, C.R. Feng, G. Spanos, 3D Crystallographic and morphological analysis of coarse martensite: Combining EBSD and serial sectioning, Scr Mater 55 (2006) 11–16. https://doi.org/10.1016/j.scriptamat.2005.12.061.
[24] T.L. Burnett, R. Kelley, B. Winiarski, L. Contreras, M. Daly, A. Gholinia, M.G. Burke, P.J. Withers, Large volume serial section tomography by Xe Plasma FIB dual beam microscopy, Ultramicroscopy 161 (2016) 119–129. https://doi.org/10.1016/j.ultramic.2015.11.001.
[25] R. DeMott, N. Haghdadi, X. Liao, S.P. Ringer, S. Primig, 3D characterization of microstructural evolution and variant selection in additively manufactured Ti-6Al-4 V, J Mater Sci 56 (2021) 14763–14782. https://doi.org/10.1007/s10853-021-06216-2.
[26] Z. Sun, S.-P. Tsai, P. Konijnenberg, J.-Y. Wang, S. Zaefferer, A large-volume 3D EBSD study on additively manufactured 316L stainless steel, Scr Mater 238 (2024) 115723. https://doi.org/10.1016/j.scriptamat.2023.115723.
[27] K. Wang, H. Feng, Y. Ling, X. Wan, S. Zhou, S. Yershov, K. Wu, Three-dimensional morphology and crystallographic characteristics of the low-temperature bainitic microstructure in high-carbon steel, Vacuum 216 (2023). https://doi.org/10.1016/j.vacuum.2023.112465.
[28] R. Wirth, Focused Ion Beam (FIB) combined with SEM and TEM: Advanced analytical tools for studies of chemical composition, microstructure and crystal structure in geomaterials on a nanometre scale, Chem Geol 261 (2009) 217–229. https://doi.org/10.1016/j.chemgeo.2008.05.019.
[29] P. Burdet, J. Vannod, A. Hessler-Wyser, M. Rappaz, M. Cantoni, Three-dimensional chemical analysis of laser-welded NiTi–stainless steel wires using a dual-beam FIB, Acta Mater 61 (2013) 3090–3098. https://doi.org/10.1016/j.actamat.2013.01.069.
[30] X. Zhong, D.J. Rowenhorst, H. Beladi, G.S. Rohrer, The five-parameter grain boundary curvature distribution in an austenitic and ferritic steel, Acta Mater 123 (2017) 136–145. https://doi.org/10.1016/j.actamat.2016.10.030.
[31] S. Morito, A.H. Pham, T. Hayashi, G. Miyamoto, T. Furuhara, Three-dimensional Characterisation of Microstructures in Low-carbon Lath Martensite, ISIJ International 62 (2022) 1972–1980. https://doi.org/10.2355/isijinternational.ISIJINT-2022-157.
[32] S. Morito, A.H. Pham, T. Ohba, T. Hayashi, T. Furuhara, G. Miyamoto, Three-dimensional observations of morphology of low-angle boundaries in ultra-low carbon lath martensite, Microscopy 66 (2017) 380–387. https://doi.org/10.1093/jmicro/dfx027.

[33] S. Morito, Y. Edamatsu, K. Ichinotani, T. Ohba, T. Hayashi, Y. Adachi, T. Furuhara, G. Miyamoto, N. Takayama, Quantitative analysis of three-dimensional morphology of martensite packets and blocks in iron-carbon-manganese steels, J Alloys Compd 577 (2013). https://doi.org/10.1016/j.jallcom.2012.02.004.
[34] S. Morito, T. Hayashi, T. Ohba, Y. Adachi, THE RELATIONSHIP BETWEEN MICROSTRUCTURAL UNITS AND THEIR BOUNDARY NATURES IN ULTRA-LOW CARBON LATH MARTENSITE, n.d.
[35] S. Morito, S. Yoshida, R. Hayamizu, T. Hayashi, T. Ohba, H. Terasaki, Y.I. Komizo, Three-dimensional approach to observing growth of blocks and packets in Fe-18Ni maraging steel, in: Materials Science Forum, Trans Tech Publications Ltd, 2014: pp. 916–919. https://doi.org/10.4028/www.scientific.net/msf.783-786.916.
[36] D. Thibault, P. Bocher, M. Thomas, J. Lanteigne, P. Hovington, P. Robichaud, Reformed austenite transformation during fatigue crack propagation of 13%Cr-4%Ni stainless steel, Materials Science and Engineering: A 528 (2011) 6519–6526. https://doi.org/10.1016/j.msea.2011.04.089.
[37] M.A. Groeber, M.A. Jackson, Groeber and Jackson Integrating Materials and Manufacturing Innovation, 2014. http://www.immijournal.com/content/3/1/5.
[38] B. Geveci, ParaView: An End-User Tool for Large Data Visualization, n.d. https://www.researchgate.net/publication/247111133.
[39] F. Niessen, T. Nyyssönen, A.A. Gazder, R. Hielscher, Parent grain reconstruction from partially or fully transformed microstructures in MTEX, J Appl Crystallogr 55 (2022) 180–194. https://doi.org/10.1107/S1600576721011560.
[40] T. Nyyssönen, A.A. Gazder, R. Hielscher, F. Niessen, Habit plane determination from reconstructed parent phase orientation maps, Acta Mater 255 (2023). https://doi.org/10.1016/j.actamat.2023.119035.
[41] H.K. Yeddu, V.I. Razumovskiy, A. Borgenstam, P.A. Korzhavyi, A. V. Ruban, J. Ågren, Multi-length scale modeling of martensitic transformations in stainless steels, Acta Mater 60 (2012) 6508–6517. https://doi.org/10.1016/j.actamat.2012.08.012.
[42] E. Galindo-Nava, On a mathematical theory for the crystallography of shear transformations in metals: Unification of mechanisms, Materialia (Oxf) 33 (2024). https://doi.org/10.1016/j.mtla.2024.102033.
[43] X.L. Wan, H.H. Wang, L. Cheng, K.M. Wu, The formation mechanisms of interlocked microstructures in low-carbon high-strength steel weld metals, Mater Charact 67 (2012) 41–51. https://doi.org/10.1016/j.matchar.2012.02.007.
[44] M.A. MANGAN, P.D. LAUREN, G.J. SHIFLET, Three-dimensional reconstruction of Widmanstätten plates in Fe–12.3Mn–0.8C, J Microsc 188 (1997) 36–41. https://doi.org/10.1046/j.1365-2818.1997.2380799.x.
[45] R. DeMott, N. Haghdadi, Z. Gandomkar, X. Liao, S. Ringer, S. Primig, Formation and 3D morphology of interconnected α microstructures in additively manufactured Ti-6Al-4V, Materialia (Oxf) 20 (2021). https://doi.org/10.1016/j.mtla.2021.101201.
[46] C. Cayron, EBSD imaging of orientation relationships and variant groupings in different martensitic alloys and Widmanstätten iron meteorites, Mater Charact 94 (2014) 93–110. https://doi.org/10.1016/j.matchar.2014.05.015.
[47] P. Thome, M. Schneider, V.A. Yardley, E.J. Payton, G. Eggeler, Crystallographic Analysis of Plate and Lath Martensite in Fe-Ni Alloys, Crystals (Basel) 12 (2022). https://doi.org/10.3390/cryst12020156.

Chapter 4

On the correlation between the habit plane and 3D morphology of lath martensite: A direct 3D observation using serial sectioning tomography of a low-carbon stainless steel

Complete Citation:

Mehdi Mosayebi, Daniel Paquet, Pierre-Antony Deschênes, Laurent Tôn-Thât, Betty Huang, and Nabil Bassim. "On the correlation between the habit plane and 3D morphology of lath martensite: A direct 3D observation using serial sectioning tomography of a low-carbon stainless steel." Scripta Materialia, 255 (2025): 116367.

On the correlation between the habit plane and 3D morphology of lath martensite: A direct 3D observation using serial sectioning tomography of a low-carbon stainless steel

Mehdi Mosayebi[1,4], Daniel Paquet[2], Pierre-Antony Deschênes[2,3], Laurent Tôn-Thât[2], Betty Huang[1,4], Nabil Bassim[1,4,]*

[1] Department of Materials Science and Engineering, McMaster University, Hamilton, ON, Canada.

[2] Hydro Quebec Research Institute (IREQ), Varennes, QC, Canada.

[3] Department of Mechanical Engineering, École de technologie supérieure, Montreal, QC, Canada.

[4] Canadian Centre for Electron Microscopy, McMaster University, Hamilton, ON, Canada.

Abstract

The crystallography and morphology of lath martensite in a low-carbon 13Cr-4Ni stainless steel were analyzed by large-volume, high-resolution serial sectioning tomography using a combination of Xe plasma focused ion beam (PFIB) and electron backscatter diffraction (EBSD) analysis. The extracted 3D EBSD results were compared with 2D observations, and potential misinterpretations arising from 2D analyses were highlighted. 3D reconstruction of the packets revealed that the volume of each prior austenite grain (PAG) is occupied with four distinct types of packets, arranged as a specific tetrahedral pattern in 3D. Through geometrical calculations, a direct link between 3D characteristics of this tetrahedral pattern and the dominant habit plane of the microstructure, {557}γ, was established. These findings, unattainable through 2D characterizations, are expected to enhance our understanding of lath martensite formation and inform recent modeling efforts aimed at accurately representing the 3D structure and mechanical properties of these alloys.

Keywords: 3D electron backscatter diffraction (3D-EBSD), martensitic steels, microstructure, focused ion beam (FIB)

4.1 Introduction

Lath martensite, a prominent microstructural constituent in low-carbon stainless steels, is of great importance as a strength-providing microstructural constituent in martensitic or multi-phase steels [1]. It is well known to exhibit a highly intricate microstructure comprising several structural units from a morphological perspective: lath, block, packet, and prior austenite grain (PAG). According to the well-known Kurdjumov–Sachs (K-S) orientation relationship (OR) [2,3], a single crystal of γ can evolve into 24 equivalent crystallographically distinct lath martensite variants (V1–V24) based on the symmetry of the cubic system. These 24 variants are grouped into four distinct crystallographic packets since γ has four close-packed (CP) {111} planes (i.e., 6 variants for each {111} plane). The 6 variants in a given packet share the same habit plane and organize themselves as variant-pairs in structures known as blocks, separated by high-angle boundaries, and low-misoriented laths [2,3].

The complex morphology of lath martensite has been the subject of extensive research due to its critical role in determining the material's strength, toughness, and ductility [4-7]. The study of lath martensite has conventionally relied on two-dimensional (2D) imaging techniques such as transmission electron microscopy (TEM) and scanning electron microscopy (SEM). While TEM techniques provide information from a limited field of view, the development of Electron Backscatter Diffraction (EBSD), as an SEM based technique, has enabled a more systematic characterization of martensitic structures, spanning from individual lath to multiple PAGs [8-10]. Despite the valuable insights these techniques have provided into both crystallography and morphology of lath martensite, they inherently lack the ability to capture the full three-dimensional (3D) nature of lath martensite. In light of this, serial sectioning has been integrated with EBSD to provide a robust methodology for 3D orientation mapping of lath martensite . For instance, Morito

et al. [11-13] combined EBSD analysis with serial mechanical polishing to analyze the lath martensite morphology in low-carbon steels. Rowenhorst et al. [14] used the same technique to investigate the 3D morphology of coarse martensite crystals in a commercial HSLA-100 steel. Few other studies [15-17] utilized focused ion beam (FIB) tomography to investigate the morphology and crystallography of single laths, block boundaries, and sub-block boundaries at higher resolutions. Note that the crystallographic features reported in most of these studies, except for those reported by Morito [11-13], all correspond to relatively small to mid-sized structural units and no large-scale 3D information is available for martensitic structures in steels.

In the modeling area there have been a number of recent reports utilizing phase field modeling to simulate the martensitic structures in 3D [18-22]. In most of these simulation studies, approximated values or informed estimates have been utilized for generating the martensitic features due to the lack of their experimentally determined magnitudes. For instance, no rules are established on how packets are oriented within a PAG or how they geometrically partition the space of the PAGs. Moreover, most of these studies have not considered the complete hierarchy of lath martensite microstructure at the scale of multiple PAGs, a consideration essential for accurate virtual mechanical testing of a digital twin of these steels [7,18,21,23].

Accordingly, the present study aims to employ a large-volume serial sectioning tomography to analyse the 3D structure of lath martensite using a combination of Xe plasma FIB (PFIB) and EBSD technique. The results of this study highlight the importance of such 3D characterizations in understanding the lath martensite morphology and crystallography, and will provide new insights into 3D architecture of lath martensite through establishing a direct link between the dominant habit plane and the spatial arrangement of the packets in 3D.

4.2 Material and Methods

The material used in this study is the CA6NM alloy [24], a low-carbon martensitic stainless-steel with an average PAG size of 158.1μm (Figure 4.1(a1)) and chemical composition of Fe-12.1Cr-3.57Ni-0.52Mn-0.26Si-0.55Mo-0.034P-0.02C-0.005S, commonly used in the hydroelectric industry. A volume of roughly 140 × 140 × 90 μm^3 was lifted out for serial sectioning using a dual-beam TFS Helios G5 Xe PFIB system. The sectioning and EBSD scans were carried out under the following conditions and controlled by the Auto-slice-and-view software. The slice thickness was set to 250 nm and EBSD were collected every other slice for a final z-resolution of 500 nm. A current of 0.2 μA was used for slicing the block, and a 5° rocking mill was used in order to prevent curtaining effects. 2D EBSD maps were collected at 20 keV with a current of 13 nA using an Oxford Symmetry detector and the Aztec control software. Each EBSD map covered the entire sample face with indexing at 500 nm step size in order to provide approximately cubic voxels for the 3D reconstructions. In total, 180 individual slices were collected on a sequence of X-Y planes. Although this resolution is not sufficient to resolve the martensitic laths, larger microstructural units such as sub-blocks, blocks, packets, and PAGs can be readily identified within the acquired dataset. Reconstruction steps including importation of the raw data, thresholding, alignment, clean-up, and segmentation were all carried out in DREAM.3D software [25], using a grain boundary misorientation threshold angle of 2°. The PAG identification and variant analysis were carried out using a MATLAB code with the help of MTEX toolbox, originally developed by Niessen et al. [26] (see Supplementary Materials Fig.S1). Following reconstruction and segmentation, the final 3D dataset was visualised using ParaView software.

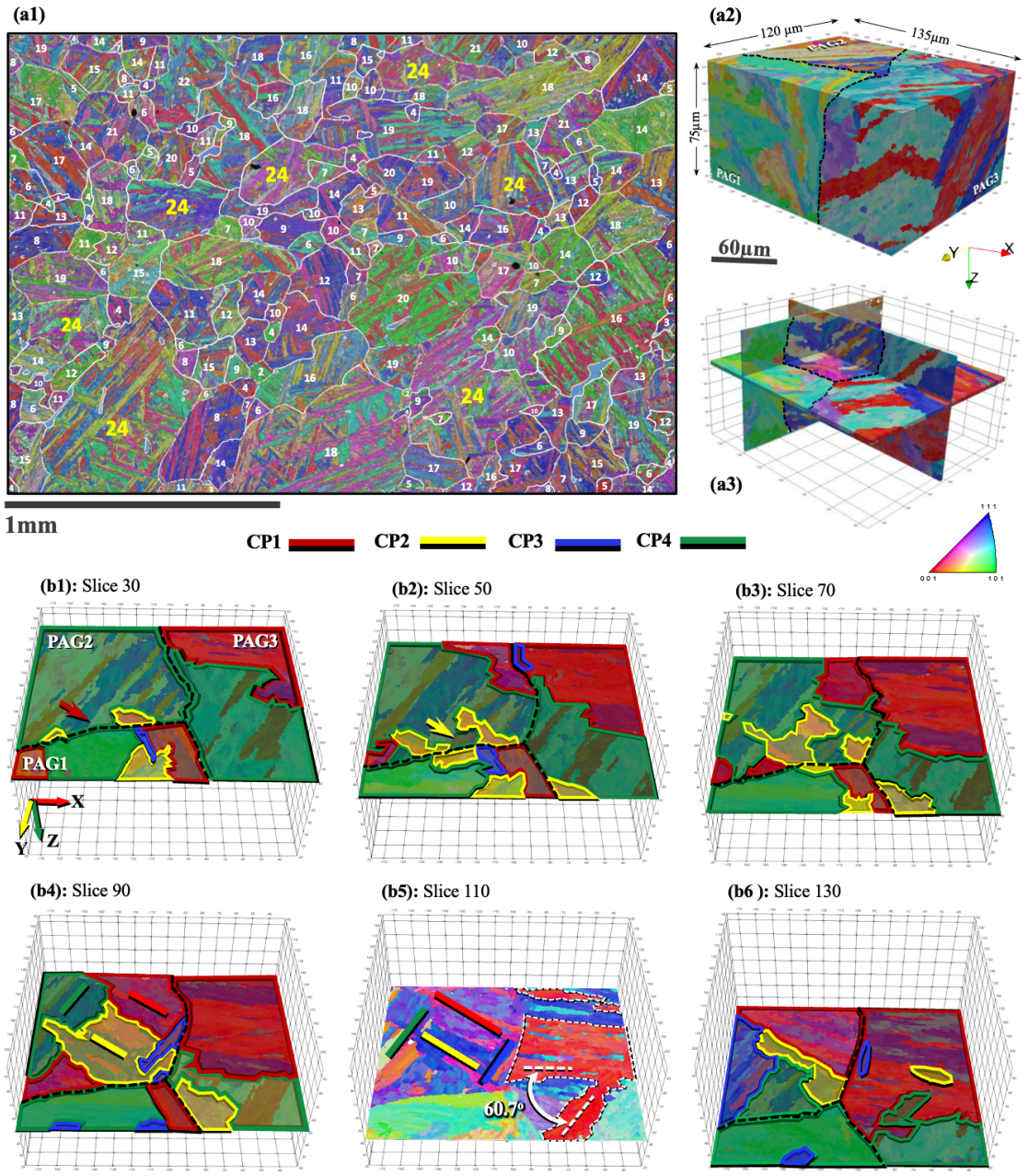

Figure 4.1: (a1) A large-area 2D inverse pole figure (IPF) map of the microstructure showing 189 PAGs along with the number of K-S variants identified within each PAG; **(a2)** The reconstructed 3D volume view and **(a3)** the orthogonal slice view of the martensitic structure after cropping the 3D EBSD dataset to a neat rectangular prism of 135 × 120 × 75 µm^3 (the black dashed lines showing the PAG boundaries); **(b1-b6)** 2D EBSD maps correspond to slices 30, 50, 70, 90, 110, and 130, respectively. Martensitic packets within each PAG are highlighted based on their corresponding CP groups using four distinct colors (CP1(red), CP2 (yellow), CP3 (blue), and CP4 (green), correspond to (111), (1−11), (−111), and (11−1) close packed planes, respectively, in the K-S relationships [3].) (All the 2D and 3D orientation maps are color coded based on IPF-Z while Z//slicing direction).

4.3 Results and discussion

Figure 4.1(a2 and a3) display the reconstructed 3D volume view and the orthogonal slice view of the martensitic microstructure. Three distinct PAGs (PAG1-PAG3), exhibiting a typical lath martensite structure, are partially located in the collected dataset as indicated by the black dashed lines delineating the PAG boundaries. A slice-by-slice observation of the microstructure is also provided in Fig.4.1(b1-b6), revealing the internal structure of PAGs. Within each PAG, all the martensitic packets were identified using the K-S orientation relationship and then color coded based on their corresponding close-packed (CP) $\{111\}_\gamma // \{110\}_\alpha$ planes. Here the CP group (CP1-CP4) and K-S variant (V1-V24) numbering/indexing follows the notations described by Takayama et al. [3]. Despite the relatively small distance between the adjacent 2D EBSD maps (approximately 10 μm), the apparent morphology of the packets, such as their shape, size, and distribution, varies significantly across the sectioning locations, illustrating a complex 3D structure within the PAGs. 3D reconstructions of PAG1-PAG3, while packets correspond to CP1-CP4 are rendered in four unique colors to provide a better sense of their shape, orientation, and distribution, are therefore presented in Figure 4.2(a1-a3). Moreover, for a closer examination of the packet's morphology and crystallography, the volume of PAG2 was further decomposed into its corresponding packets, as demonstrated in Figure 4.2(b1-b4). As evident, packets are anisotropic in shape and composed of three parallel plate-like blocks in 3D. Such morphology makes 2D analysis of the martensitic features being highly dependent on their spatial orientation and location. For instance, a monolithic feature in 3D, like the only packet corresponds to CP2 in Figure 4.2(b2), can present itself as a number of smaller separated packets with irregular shapes and various sizes on 2D EBSD maps (yellow areas in PAG2 in Figure 4.1(b1-b6)). In contrast, multiple separated packets, such as the 5 martensitic packets associated with CP1 in Figure 4.2(b1), can be easily

overlooked if only single 2D-EBSD maps are analyzed (e.g. red areas in PAG2 in Figure 4.1(b1 and b6)).

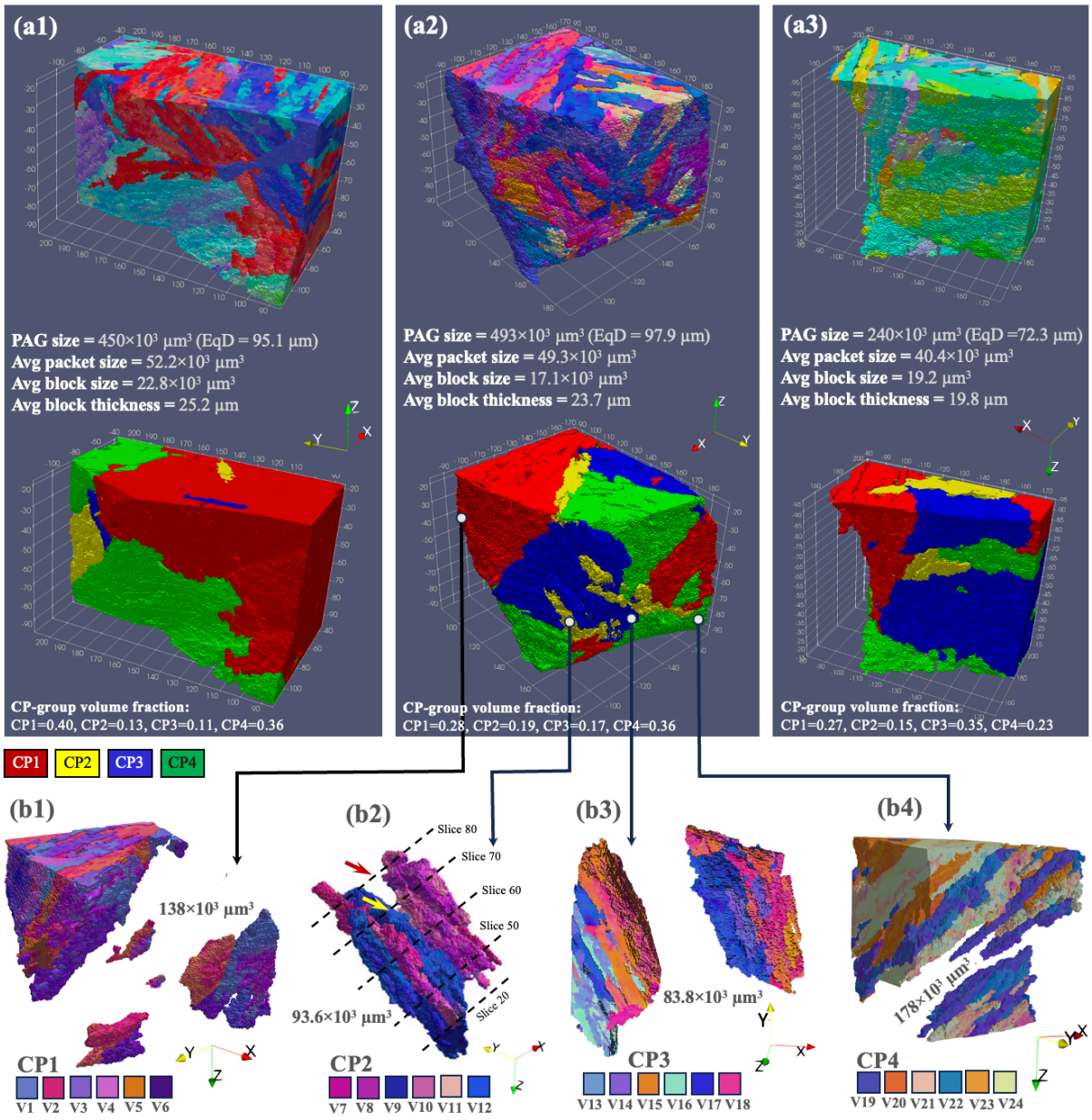

Figure 4.2: (a1-a3) 3D reconstructions of PAG1-PAG3, respectively, in forms of IPF-Z and CP maps (packets in CP maps are rendered in same colors as Fig.1. The average PAG size in forms of total volume (µm^3) and equivalent diameter (EqD), as well as packet and block sizes are presented in **(a1-a3)**); **(b1-b4)** Decomposition of the 3D volume of PAG2 into its four CP groups (CP1-CP4) and their corresponding packets and K-S variants. (Orientation maps and all the 24 K-S variants are color coded based on IPF-Z while Z//slicing direction. Black dashed lines and the 2 arrow in (b2) show the locations of the 2D slices mentioned in Fig.(b1-b6)).

Given this notable heterogeneity, it is logical to expect that the accuracy of 2D variant/crystallographic analyses may also be impacted. For instance, 2D orientation maps in Figure 4.1(b1-b6) were only able to capture a maximum of 11-19 K-S variants within PAG2. Although this observation can be due to the incomplete picture of the PAGs in these 2D EBSD maps, orientation analysis on a large-area 2D EBSD map provided in Figure 4.1(a1), illustrated that among 187 PAGs only 7 PAGs had the chance to capture all the 24 K-S variants. In other words, even with a large-area and complete view of the PAG, it still seems unlikely to picture all the 24 K-S variants on a single 2D cross-section of the PAG. This is while, 3D orientation maps extracted from a portion of PAG2 in Figure 4.2(b1-b4), revealed that all the CP1-CP4, regardless of their considerable size difference, consist of six distinct K-S variants, indicating that all the 24 K-S variants can be observed within this volume of PAG2.

As another important characteristic of lath martensite, it is possible to assess the spatial orientation of martensitic features, and thereby their general morphology and configurations in 3D. Taking PAG2 as an example, the provided X-Y sections (i.e., planes parallel to the sample surface) in Figure 4.1(b1-b6) demonstrate CP1-CP4 packets as either parallel (e.g., CP1 $\parallel$ CP2 and CP3 $\parallel$ CP4) or orthogonal (e.g., CP2 $\perp$ CP3) to each other, as indicated by the straight lines in Figure 4.1(b4 and b6). 3D perspectives shown in Figure 4.3(a1-a3), however, reveal that they are orientated at $84.4^{o} \pm 3.1^{o}$, $83.5^{o} \pm 2.8^{o}$, and $60.7^{o} \pm 2.6^{o}$ relative to each other in space (see Supplementary Materials for more details). Through 3D examination of the packets in two other PAGs, same spatial orientations were identified in both PAG1 and PAG3. Figure 4.3(b1) represents a 3D visualization of the blocks marked by the white dashed lines in Figure 4.1(b5), corresponding to CP1 and CP4 packets in PAG3. 2D sections through these platelets in PAG3 (Figure 4.3(b2 and b3)), revealed almost the same connection angles of 86.4^{o} and 60.7^{o} (as also

schematically presented in Figure 4.3(c1-c3)), indicating that 3D configuration of the packets follows a definite pattern within the microstructure.

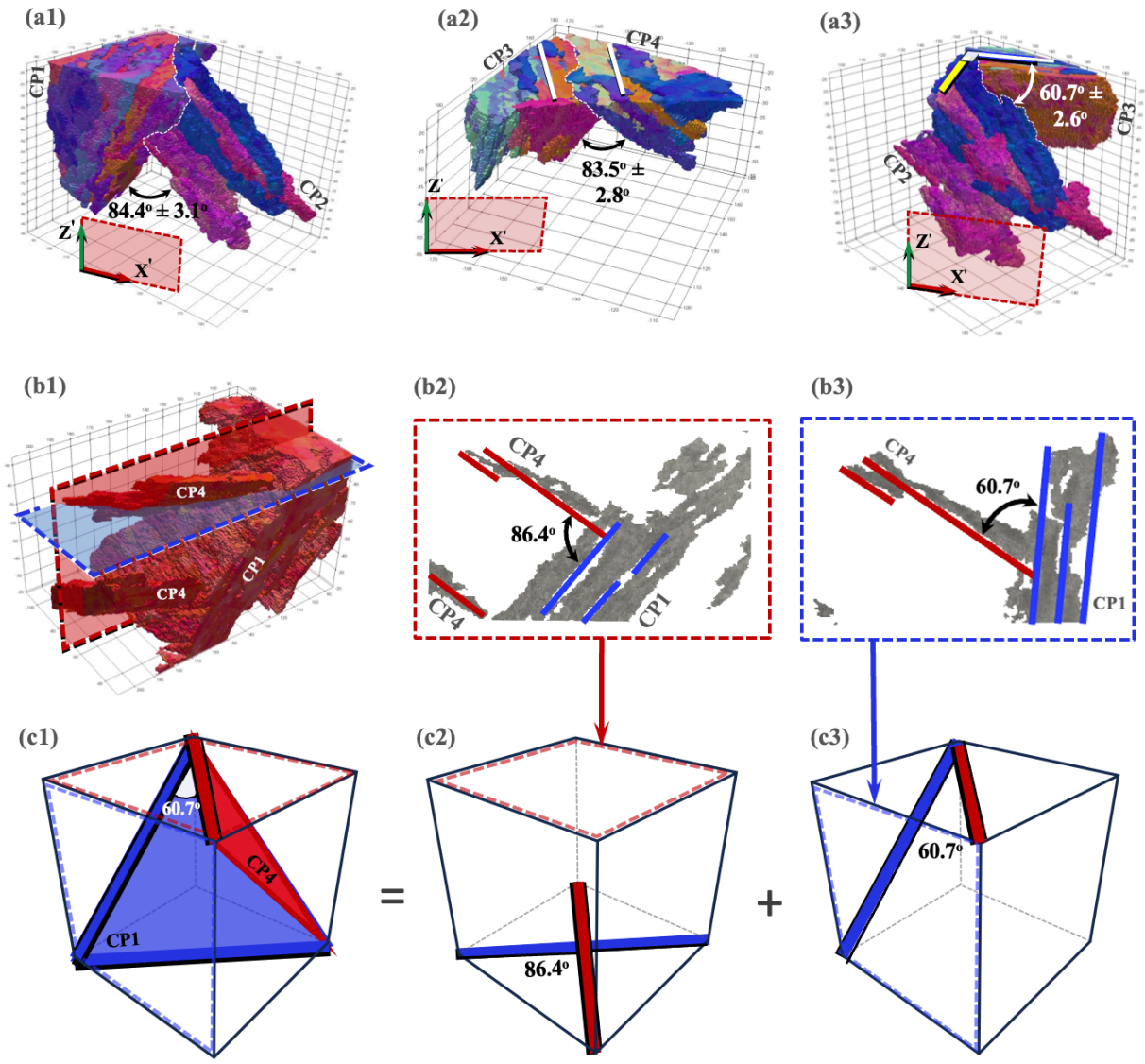

Figure 4.3: 3D perspectives of the packets in PAG2: **(a1)** spatial orientation between CP1 and CP2, **(a2)** spatial orientation between CP3 and CP4, and **(a3)** spatial orientation between CP2 and CP3; **(b1)** 3D perspective of the blocks marked with white dashed lines in Fig.1(b5) correspond to CP1 and CP4 in PAG3; **(b2 and b3)** 2D sections parallel to the red and blue planes shown in **(b1); (c1-c3)** schematic representation of the spatial orientations/angles between CP1 and CP4, observed from two different views (normal to the red and blue planes in (b1-b3)).

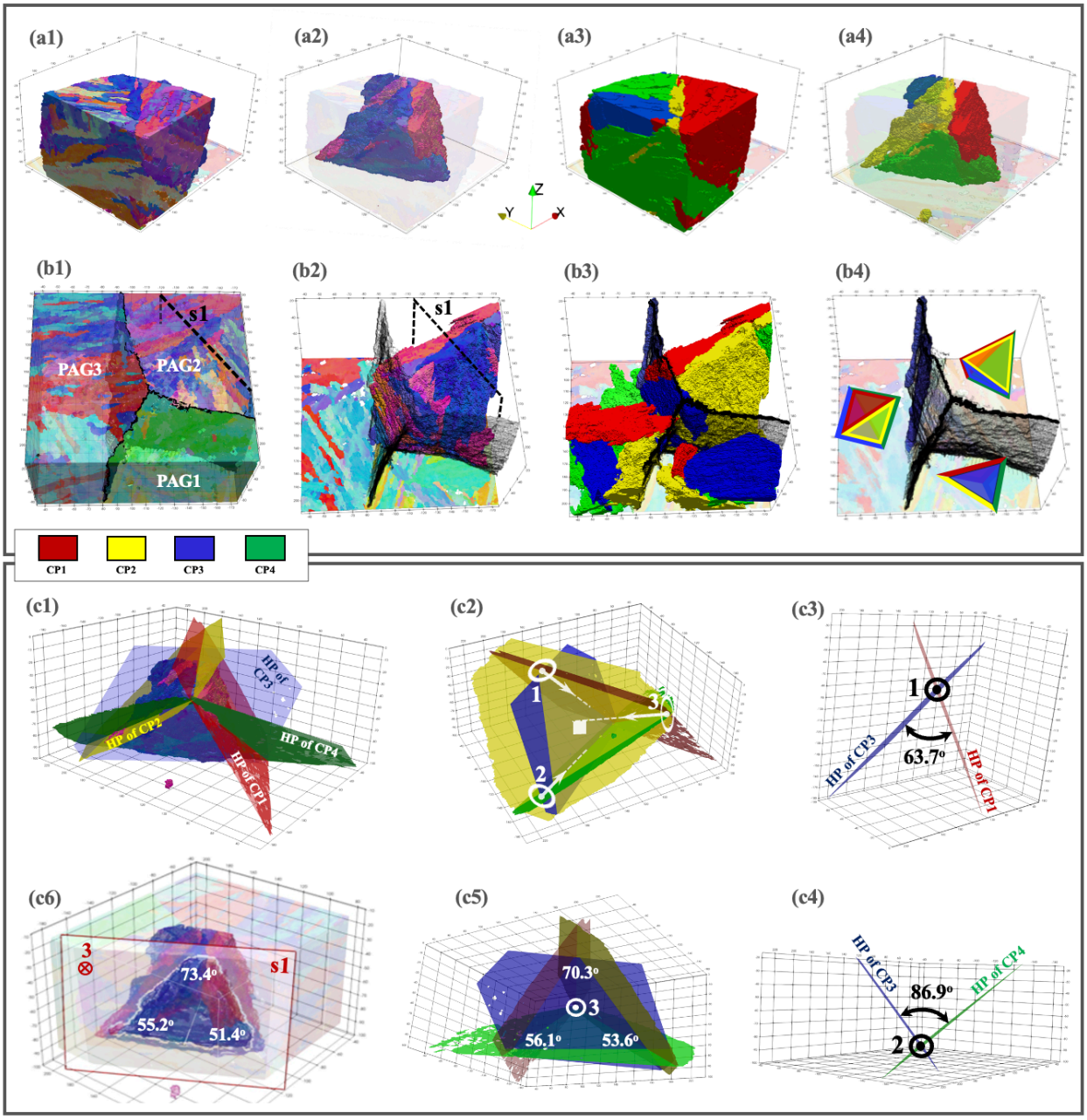

Figure 4.4: (a1 and a3) 3D view of PAG2 in forms of IPF-Z and CP maps, respectively (packets in CP maps are rendered in same colors as Fig.1and 2); **(a2 and a4)** Internal structure of the PAG2 showing a tetrahedron formed by the largest blocks of each CP group; **(b1-b4)** 3D views of the entire volume of the dataset while **(b1)** shows PAG1-PAG3 and their boundaries reconstructed in 3D, **(b2)** shows another view of the (a2) and (a4), and **(b3 and b4)** represent the tetrahedral morphology and their overall 3D orientations observed within each of the PAG1-PAG3; **(c1 and c2)** 3D habit plane traces of CP1-CP4 shown with four transparent planes manually fitted to the blocks presented in (a2); **(c3 and c4)** 3D habit planes viewed along the white arrows 1 and 2 in (c2); **(c5 and c6)** 3D habit planes and the tetrahedral morphology in (a2), viewed along the white arrow 3 in (c2). (arrows 1 and 2: parallel to the tetrahedron's edges, and arrow 3: normal to the tetrahedron's faces).

To further clarify this pattern, Figure 4.4(a1-a4) illustrate 3D views of PAG2 in forms of IPF and CP maps. Displaying the largest blocks from each of the packets in Figure 4.4(a2 and a4), revealed a tetrahedral pattern formed by CP1-CP4 within the volume of PAG2. To check if this tetrahedral configuration is the dominant case for the entire microstructure, Figure 4.4(b1-b4) provide an overview of the dataset presenting all the PAGs along with their grain boundaries in 3D. Even though none of the PAGs represent the full volume of a grain, it seems that the large-volume 3D EBSD dataset had the chance to capture all the 4 possible CP groups and most of their corresponding blocks in all the three PAGs (Figure 4.4(b3)). As depicted in Figure 4.4(b3), 3D space of all PAG1-PAG3 are occupied by a similar tetrahedral configuration, suggesting that the formation of packets on CP1-CP4 has built up a regular space structure within all PAGs.

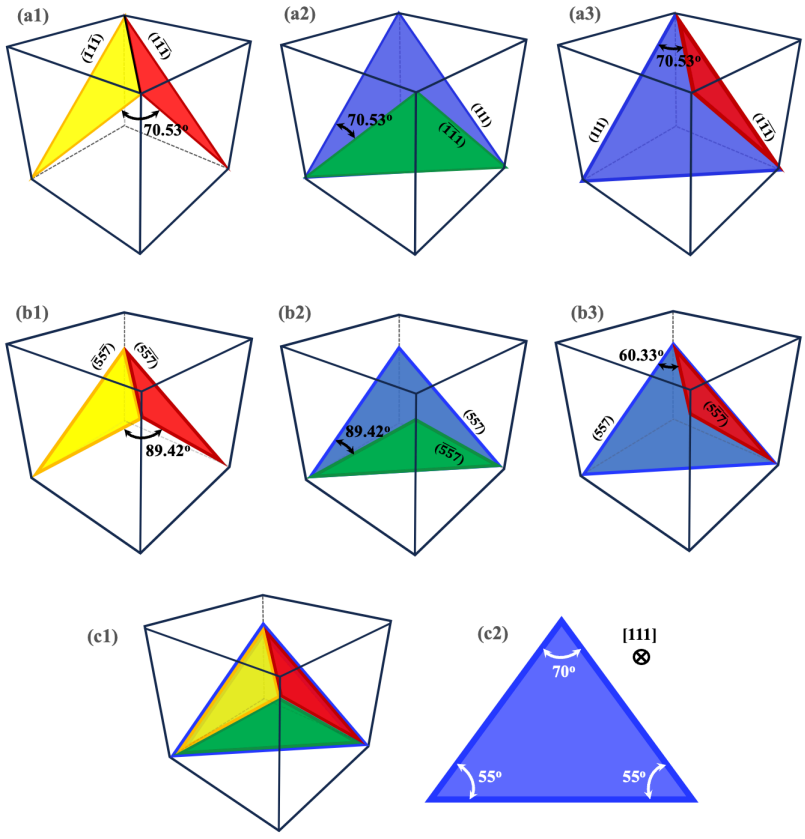

Figure 4.5: Geometric patterns of **(a1-a3)**{111}γ and **(b1-b3)**{557}γ habit planes in a fixed reference frame; **(c1)** 3D and **(c2)** 2D views of the tetrahedral/triangular pattern formed by{557}γ habit planes along [111] axis.

Formation of 3D patterns, such as V-shaped or hollow pyramids, has been reported in Ti and NiTi shape memory alloys, occurring in the form of clusters of specific martensitic variants [27,28]. In steels, different morphologies, including diamond, triangular, and butterfly, have also been reported through various 2D observations [2,9]. While these morphologies have been explained only through the self-accommodation phenomenon [29], and no direct observation has yet revealed their 3D structures, a comprehensive 3D investigation of the tetrahedral relief observed in all PAG1-PAG3, revealed a direct correlation between the geometric characteristics of this morphology and the dominant habit plane (HP) of the microstructure. Figure 4.4 and Figure 4.5, demonstrate this correlation through a geometric comparison between the 3D HP traces of CP1-CP4 (depicted with four transparent planes manually fitted (see Supplementary Materials Figure S2) to the blocks shown in Figure 4.4(c1 and c2)) and the most common HPs of lath martensite reported in the literature (Figure 4.5). Marder and Krauss [30] reported habit planes of approximately $\{557\}\gamma$ for packets of martensite laths containing 0.2 and 0.6%C. Using trace fitting techniques, Sandvik and Wayman [31] showed that the habit plane of martensite in Fe-Ni alloys is only a few degrees away from $\{111\}_{\gamma}$. Morito et al. [13] also reported that the habit plane of lath martensite in low-carbon steels deviates from the common $\{111\}\gamma$ plane to be actually close to $\{557\}\gamma$. Accordingly, planes associated with these two families of habit planes were plotted in a fixed reference frame in Figure 4.5. As can be seen in Figure 4.5(a1-a3), $\{111\}_{\gamma}$ HPs can be expected to display an equilateral tetrahedron with packets/blocks oriented at 70.5° relative to each other. This is while for $\{557\}_{\gamma}$ HPs a tetrahedron with spatial orientations/angles of 89.4° and 60.3° can be predicted (Figure 4.5(b1-b3)). By comparing the geometric characteristics (i.e., spatial orientations) obtained from the experimental HP traces in Figure 4.4(c1-c6), and the theoretical calculations in Figure 4.5, it is suggested that the dominant habit plane of the microstructure is

much closer to $\{557\}_\gamma$. As can be seen, the tetrahedral pattern formed by the experimental HP traces in Figure 4.4(c3 and c4), illustrates 63.7° and 86.9° connection angles (when viewed along the tetrahedron's edges), closely matching the spatial orientations calculated for $\{557\}\gamma$ HPs in Figure 4.5(b1-b3). Moreover, by viewing this tetrahedral pattern normal to the tetrahedron's faces, both theoretical (Figure 4.5(c1 and c2)) and experimental (Figure 4.4(c5 and c6)) measurements demonstrate an isosceles triangle with angles of ~70° , ~55° and ~55°, further indicating the role of $\{557\}_\gamma$ HPs in shaping the 3D architecture of the microstructure. These findings are noteworthy because the effect of dominant HP has never been observed at this microstructural scale and, more importantly, directly in three dimensions. While TEM and EBSD investigations have shown the dominance of $\{557\}\gamma$ HPs at the scale of laths and blocks in low- and ultra-low-carbon steels [2,31], it appears here that this HP governs the 3D morphology of the microstructure, even at the scale of a few PAGs. Through future works, this effect could potentially be explained based on the unique properties of $\{557\}\gamma$ HP, including its good angular compatibility, minimal transformation strain misfit, and more importantly minimal long-range stresses during the lath/block propagation [2,20,32].

4.4 Summary

In summary, the present study highlights the importance of utilizing 3D techniques to investigate the complex and heterogeneous nature of lath martensite. The results of the 3D EBSD investigations offered a comprehensive picture of the hierarchical morphology of lath martensite by providing detailed 3D information regarding the crystallography, morphology, and geometry of the packets. Consequently, a specific tetrahedral morphology formed by 3D configuration of the packets within each PAG, was identified and then examined in detail. Through geometrical calculations, 3D characteristics of this tetrahedral pattern were correlated to the dominant habit

plane (HP) of the microstructure, {557}γ. These findings, which are inaccessible through 2D characterizations alone, can be applicable to future studies aiming to understand or model the mechanisms responsible for lath martensite formation, variant pairing tendencies, and the filling process of PAGs, all key aspects of martensitic transformation.

4.5 Supplementary Materials

- **PAG reconstruction and variant analysis procedure:**

To identify the PAGs, as well as the CP packets and variants, we employed a MATLAB code with the assistance of the MTEX toolbox, originally developed by Niessen et al. [26]. This code utilizes the crystallographic information from 2D EBSD maps, e.g. Euler angles, to reconstruct the PAGs, their corresponding close packed planes (CPs), and the distribution of K-S variants (V1-V24) within each packet using the K-S OR. This code was employed to generate 2D PAG maps, CP maps, and K-S variant maps from various depths of the dataset (as shown in Figure S1), to use as a reference for the definition and segmentation of PAGs, packets, and blocks.

- **3D habit plane trace determination procedure:**

The best habit plane trace for each CP group/packet was determined by manually fitting planes parallel to the surfaces of the blocks or the interfaces between the blocks or sub-blocks in 3D and using the ParaView software (Figure S2).

- **Details of gematrical calculations used in Figure 4.3(a1-a3):**

Given that the packet boundary planes change across the boundary surface in 3D (due to the inhomogeneity of the packet boundaries), we measured the angles between pairs of packets (e.g., between CP1 and CP2 in Figure 3.3(a1)) on several 2D sections across the packet boundary (e.g.,

S1-S9 in Figure S3 and Figure S4). These 2D sections were aligned orthogonal to the local plane of the boundary (e.g. the transparent red, blue, and green planes in Figure S3 and Figure S5), thereby accounting for the 3D shape of the packet boundary in our measurements. This procedure was applied to all the packets in PAG2, and the average values obtained from these 2D sections were considered as the angles between CPs in Figure 3.3(a1-a3).

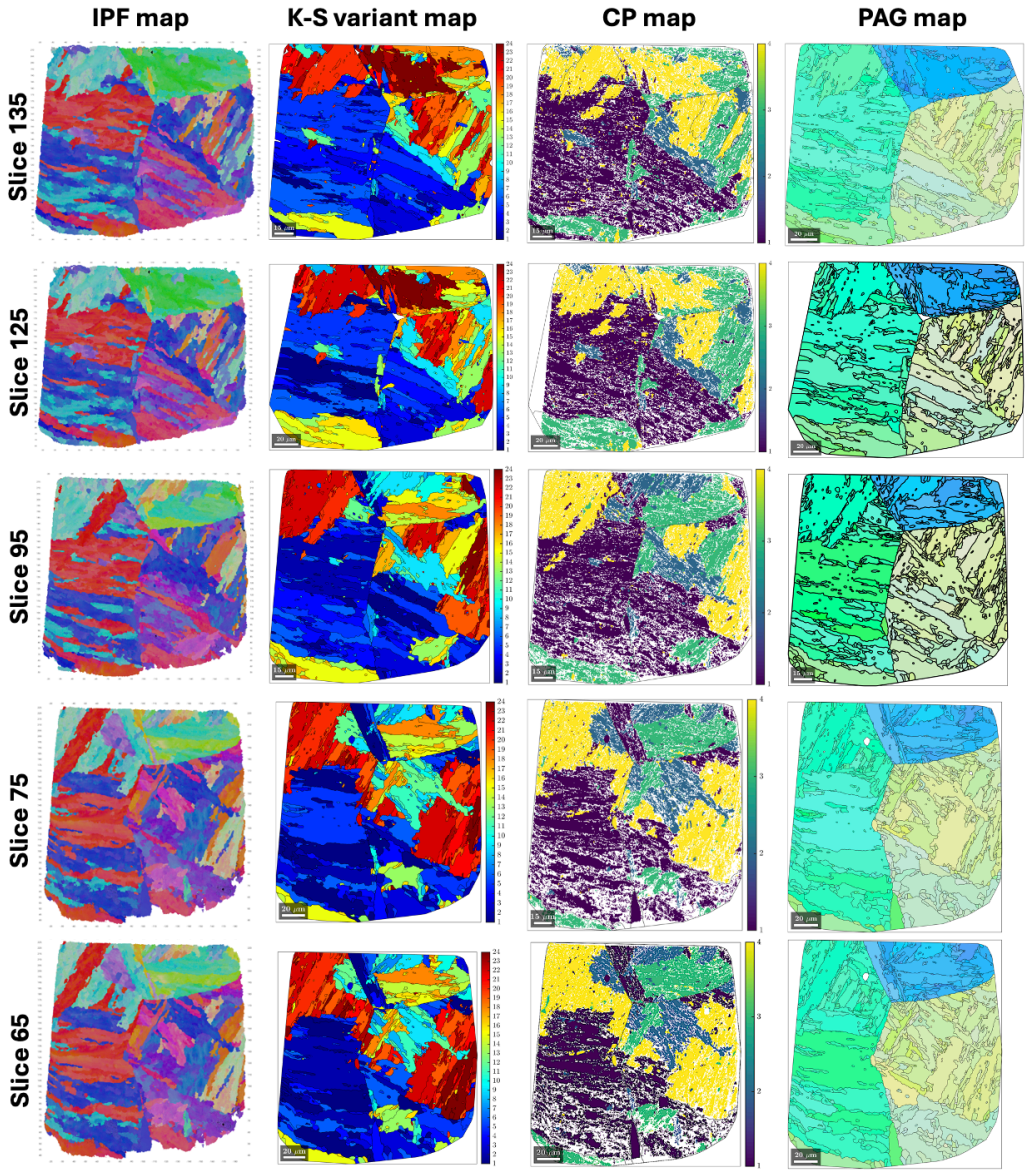

Figure S1: 2D IPF maps, K-S variant maps, CP maps, and PAG maps, extracted from various depths of the dataset using MTEX toolbox.

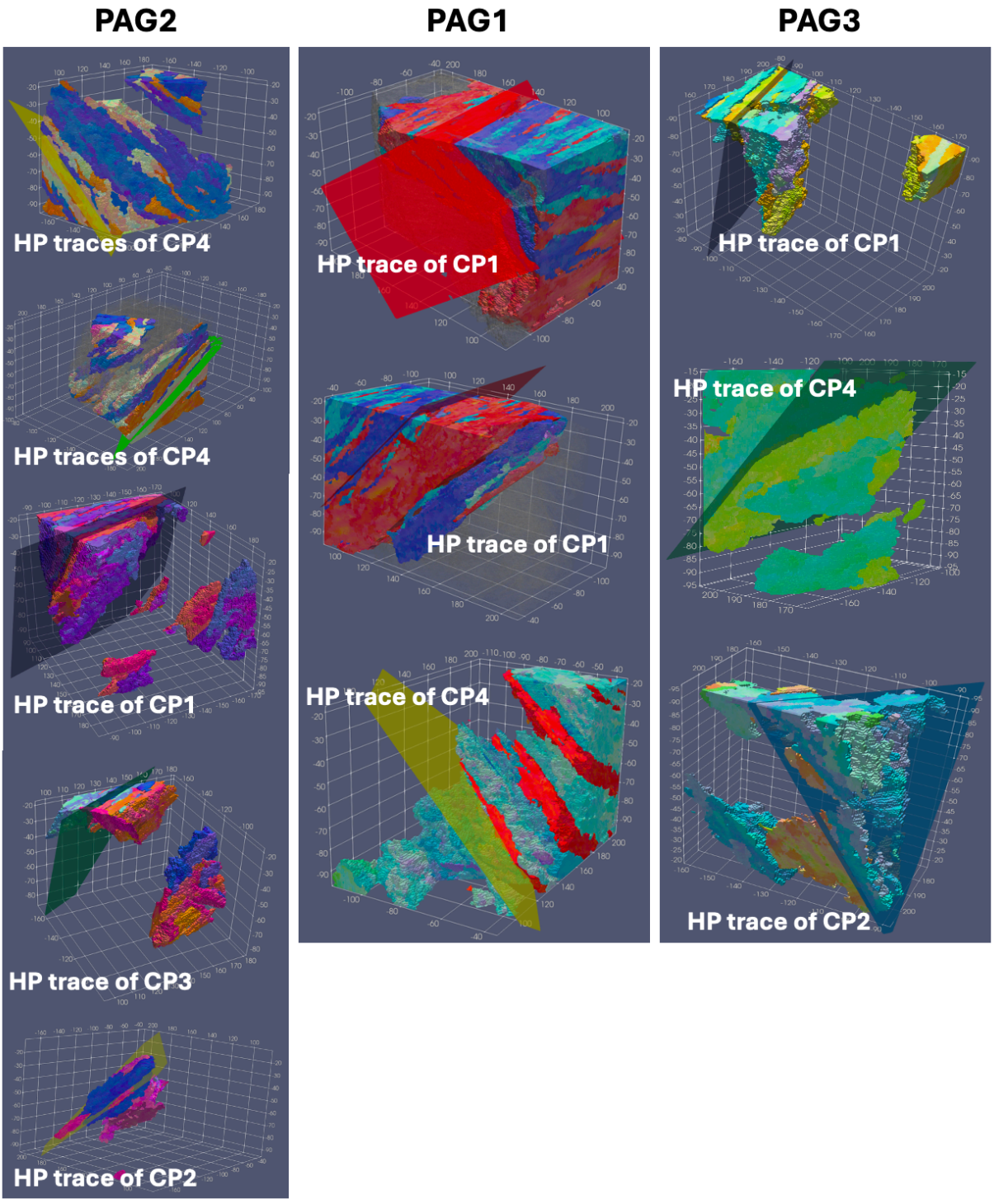

Figure S2: Examples of Habit plane trace determination for CP1-CP4 in PAG1-PAG3: the transparent planes were manually fitted to the surface of the blocks, or the interfaces between the blocks or sub-blocks, using the 3D reconstruction of CP groups/packets and their corresponding blocks in ParaView software.

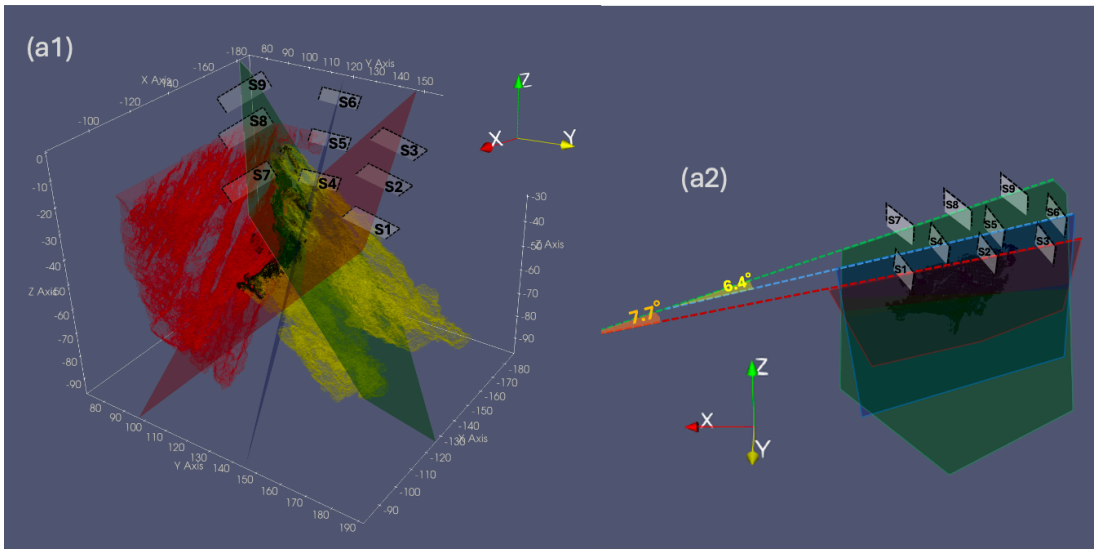

Figure S3: **(a1)** Approximate locations of 2D sections (S1-S9) positioned across CP1-CP2 boundary, and orthogonal to the boundary planes (illustrated with transparent red, blue, and green planes); **(a2)** An alternate 3D view of (a1), demonstrating how the inhomogeneity of the boundary plane can influence the angle measurements between CP1 and CP2 on 2D sections.

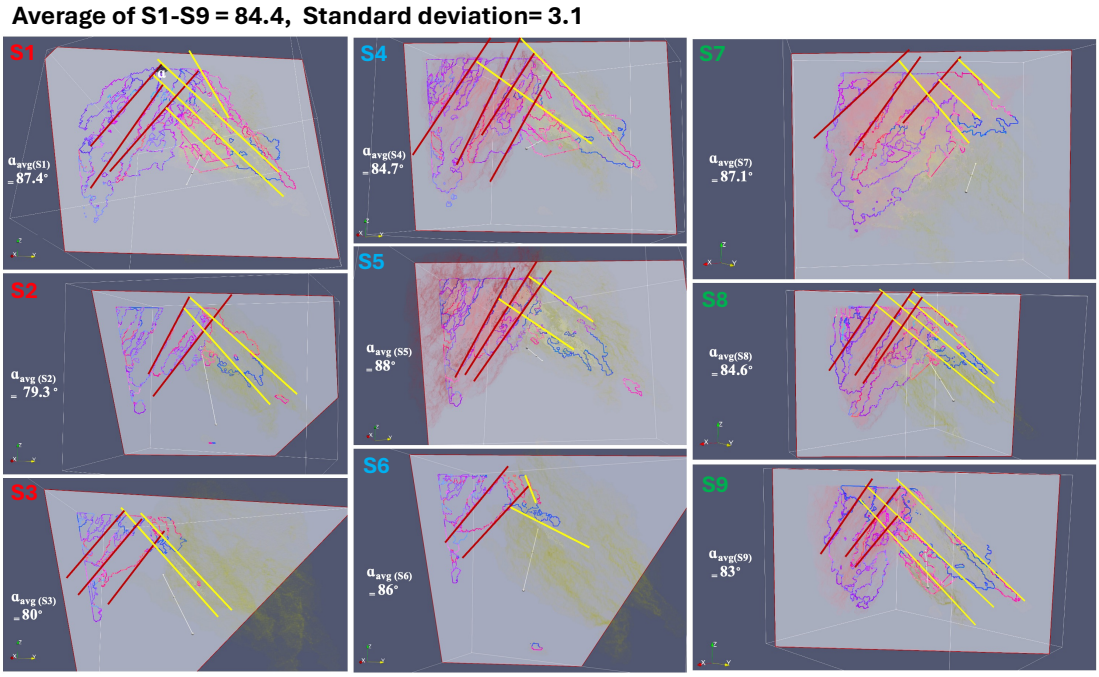

Figure S4: The process of angle measurements using the 2D sections shown in Figure S3: On each 2D section, angles, α, between blocks of CP1 and CP2 (indicated by red and yellow lines) were measured. For each section (S1-S9), the average of these angles, $\alpha_{avg(S)}$, were calculated and displayed on 2D sections in this figure. Subsequently, the overall average of $\alpha_{avg(S1)}$ through $\alpha_{avg(S9)}$ was calculated and reported in Figure 3.3(a1) of the manuscript. Same process was applied to other CPs in PAG2, with the average values reported in Figure.3.3(a2&a3) of the manuscript.

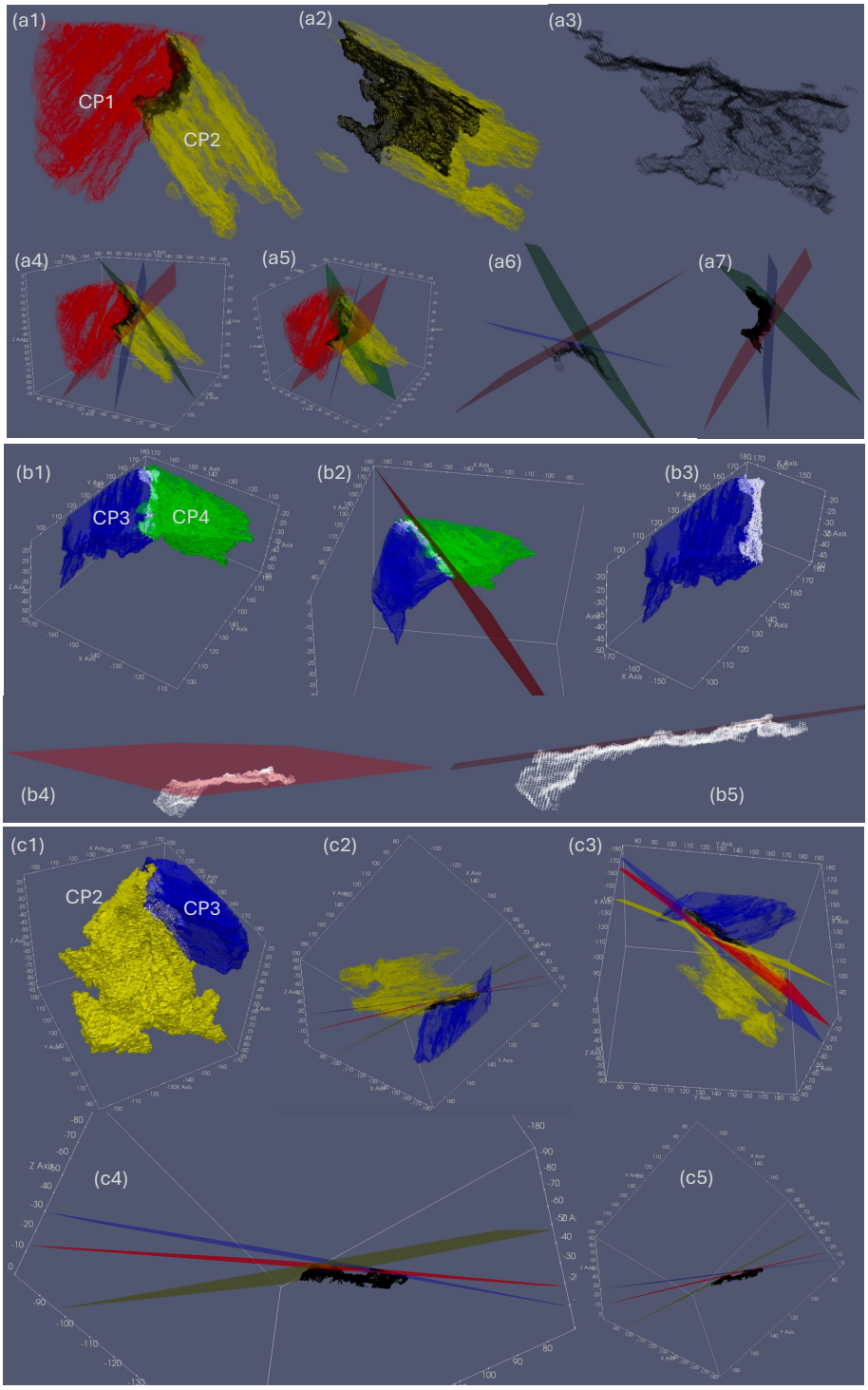

Figure S5: **(a1-a3)** 3D reconstructions of CP1, CP2, and their boundary in PAG2; **(a4-a7)** different views of packet boundary planes between CP1 and CP2; **(b1)** 3D reconstructions of CP3, CP4, and their boundary in PAG2; **(b2-b5)** different views of packet boundary planes between CP3 and CP4; **(c1)** 3D reconstructions of CP2, CP3, and their boundary in PAG2; **(c2-c5)** different views of packet boundary planes between CP2 and CP3;

References

[1] Kwak K, Mine Y, Morito S, Ohmura T, Takashima K. Correlation between strength and hardness for substructures of lath martensite in low- and medium-carbon steels. Materials Science and Engineering: A 2022;856. https://doi.org/10.1016/j.msea.2022.144007.

[2] Cayron C, Baur A, Logé R. Intricate morphologies of laths and blocks in low-carbon martensitic steels. Mater Des 2018;154:81–95. https://doi.org/10.1016/j.matdes.2018.05.033.

[3] Takayama, N., G. Miyamoto, and T. Furuhara. "Effects of transformation temperature on variant pairing of bainitic ferrite in low carbon steel." *Acta Materialia* 60, no. 5 (2012): 2387-2396. https://doi.org/10.1016/j.actamat.2011.12.018.

[4] Morsdorf L, Jeannin O, Barbier D, Mitsuhara M, Raabe D, Tasan CC. Multiple mechanisms of lath martensite plasticity. Acta Mater 2016;121:202–14. https://doi.org/10.1016/j.actamat.2016.09.006.

[5] Deschênes PA, Wheeler R, Paquet D, Lanteigne J, Serventi AM, Tôn-Thât L, et al. Micromechanical properties of low-carbon martensitic stainless steel by microtensile experiments. Materials Science and Engineering: A 2022;858. https://doi.org/10.1016/j.msea.2022.144030.

[6] Kwak K, Mayama T, Mine Y, Takashima K. Anisotropy of strength and plasticity in lath martensite steel. Materials Science and Engineering: A 2016;674:104–16. https://doi.org/10.1016/j.msea.2016.07.047.

[7] Fischer T, Zhou T, Dahlberg CFO, Hedström P. Relating stress/strain heterogeneity to lath martensite strength by experiments and dislocation density-based crystal plasticity. Int J Plast 2024;174. https://doi.org/10.1016/j.ijplas.2024.103917.

[8] Liu W bo, Song P cheng, Zhang C, Yun D, Yao C fa, Yang Z gang. Crystallographic analysis of lath martensite in a 13Cr-5Ni steel by electron backscattering diffraction. Journal of Iron and Steel Research International 2018;25:213–20. https://doi.org/10.1007/s42243-018-0023-5.

[9] Sato H, Zaefferer S. A study on the formation mechanisms of butterfly-type martensite in Fe-30% Ni alloy using EBSD-based orientation microscopy. Acta Mater 2009;57:1931–7. https://doi.org/10.1016/j.actamat.2008.12.035.

[10] Sugiyama M, Takei M, Sekida S, Maruyama N. Characterization of hierarchical lath martensite microstructure in low carbon steels using ultra-high voltage TEM and SEM-EBSD analysis. IOP Conf Ser Mater Sci Eng 2022;1249:012020. https://doi.org/10.1088/1757-899x/1249/1/012020.

[11] Morito S, Edamatsu Y, Ichinotani K, Ohba T, Hayashi T, Adachi Y, et al. Quantitative analysis of three-dimensional morphology of martensite packets and blocks in iron-carbon-manganese steels. J Alloys Compd 2013;577. https://doi.org/10.1016/j.jallcom.2012.02.004.

[12] Morito S, Yoshida S, Hayamizu R, Hayashi T, Ohba T, Terasaki H, et al. Three-dimensional approach to observing growth of blocks and packets in Fe-18Ni maraging steel. Materials Science Forum, vol. 783–786, Trans Tech Publications Ltd; 2014, p. 916–9. https://doi.org/10.4028/www.scientific.net/msf.783-786.916.

[13] Morito S, Pham AH, Hayashi T, Miyamoto G, Furuhara T. Three-dimensional Characterisation of Microstructures in Low-carbon Lath Martensite. ISIJ International 2022;62:1972–80. https://doi.org/10.2355/isijinternational.ISIJINT-2022-157.

[14] Rowenhorst DJ, Gupta A, Feng CR, Spanos G. 3D Crystallographic and morphological analysis of coarse martensite: Combining EBSD and serial sectioning. Scr Mater 2006;55:11–6. https://doi.org/10.1016/j.scriptamat.2005.12.061.
[15] Morsdorf L, Tasan CC, Ponge D, Raabe D. 3D structural and atomic-scale analysis of lath martensite: Effect of the transformation sequence. Acta Mater 2015;95:366–77. https://doi.org/10.1016/j.actamat.2015.05.023.
[16] Shibata A, Miyamoto G, Morito S, Nakamura A, Moronaga T, Kitano H, et al. Substructure and crystallography of lath martensite in as-quenched interstitial-free steel and low-carbon steel. Acta Mater 2023;246. https://doi.org/10.1016/j.actamat.2023.118675.
[17] Shibata A, Gutierrez-Urrutia I, Nakamura A, Miyamoto G, Madi Y, Besson J, et al. Multi-scale three-dimensional analysis on local arrestability of intergranular crack in high-strength martensitic steel. Acta Mater 2022;234. https://doi.org/10.1016/j.actamat.2022.118053.
[18] Schäfer BJ, Song X, Sonnweber-Ribic P, Hassan HU, Hartmaier A. Micromechanical modelling of the cyclic deformation behavior of martensitic sae 4150-a comparison of different kinematic hardening models. Metals (Basel) 2019;9. https://doi.org/10.3390/met9030368.
[19] Shchyglo O, Du G, Engels JK, Steinbach I. Phase-field simulation of martensite microstructure in low-carbon steel. Acta Mater 2019;175:415–25. https://doi.org/10.1016/j.actamat.2019.06.036.
[20] Kundin J, Raabe D, Emmerich H. A phase-field model for incoherent martensitic transformations including plastic accommodation processes in the austenite. J Mech Phys Solids 2011;59:2082–102. https://doi.org/10.1016/j.jmps.2011.07.001.
[21] Gallardo-Basile FJ, Naunheim Y, Roters F, Diehl M. Lath martensite microstructure modeling: A high-resolution crystal plasticity simulation study. Materials 2021;14:1–20. https://doi.org/10.3390/ma14030691.
[22] Yeddu HK, Malik A, Gren J, Amberg G, Borgenstam A. Three-dimensional phase-field modeling of martensitic microstructure evolution in steels. Acta Mater 2012;60:1538–47. https://doi.org/10.1016/j.actamat.2011.11.039.
[23] Shanthraj P, Zikry MA. The effects of microstructure and morphology on fracture nucleation and propagation in martensitic steel alloys. Mechanics of Materials 2013;58:110–22. https://doi.org/10.1016/j.mechmat.2012.11.010.
[24] Thibault D, Bocher P, Thomas M, Lanteigne J, Hovington P, Robichaud P. Reformed austenite transformation during fatigue crack propagation of 13%Cr-4%Ni stainless steel. Materials Science and Engineering: A 2011;528:6519–26. https://doi.org/10.1016/j.msea.2011.04.089.
[25] Groeber MA, Jackson MA. Groeber and Jackson Integrating Materials and Manufacturing Innovation. vol. 3. 2014.
[26] Niessen, Frank, Tuomo Nyyssönen, Azdiar A. Gazder, and Ralf Hielscher. Parent grain reconstruction from partially or fully transformed microstructures in MTEX. Journal of applied crystallography 2022; 180-194. https://doi.org/10.1107/S1600576721011560.
[27] Gao Y, Zhou N, Wang D, Wang Y. Pattern formation during cubic to orthorhombic martensitic transformations in shape memory alloys. Acta Mater 2014;68:93–105. https://doi.org/10.1016/j.actamat.2014.01.012.

[28] Zhong HZ, Liu Z, Gu JF. The vertical and triangular morphology in the as-deposited Ti-6Al-4V. Mater Charact 2017;131:91–7. https://doi.org/10.1016/j.matchar.2017.07.012.
[29] Gu N, Song X, Zhang J, Wang R. Effects of Self-Accommodation and Plastic Accommodation in Martensitic Transformations and Morphology of Martensite. Metallurgical and Materials Transactions A, 26, pp.1979-1985.
[30] A.R. Marder, Krauss G, Formation of low carbon martensite in Fe-C alloys, Trans. ASM 62 (1969) 957–964.
[31] Sandvik B.P.J, Wayman C.M, Characteristics of lath martensite: Part I. Crystallographic and substructural features, Metall. Trans. A 14 (4) (1983) 809–822, http://dx.doi.org/10.1007/BF02644284.
[32] Zisman AA. Unique properties of habit plane (557) in origination of lath martensite. Mater Lett 2020;275. https://doi.org/10.1016/j.matlet.2020.128140.

Chapter 5

Summary and Conclusions

5.1 Summary and conclusive remarks

This thesis presents a comprehensive three-dimensional (3D) characterization of the morphology and crystallography of lath martensite in low-carbon 13Cr-4Ni martensitic stainless steel (CA6NM). Leveraging large-volume plasma-focused ion beam (PFIB) serial sectioning tomography in conjunction with electron backscatter diffraction (EBSD), this study addresses the critical need for a deeper understanding of the hierarchical microstructure, internal boundary networks, habit planes, and microstructural heterogeneities in CA6NM steel. Such insights are essential for understanding the material's mechanical behavior, predicting performance in service environments, and developing more reliable computational models for hydro-turbine steels. The findings provide novel insights that bridge gaps in existing literature and hold significant implications for both fundamental materials science and engineering applications, particularly in hydro-turbine alloys.

The 3D EBSD results reveal that the hierarchical subdivision of lath martensite follows a well-defined structure, comprising prior austenite grains (PAGs), packets, blocks, and sub-blocks. The Kurdjumov-Sachs (K-S) orientation relationship is validated as the dominant transformation mechanism, enabling a systematic classification and quantification of internal crystallographic features and their interfaces.

One of the most significant findings of this research is the direct correlation between the habit plane (HP) and the 3D morphology of lath martensite. The study demonstrates that the dominant HP of the microstructure lies between {111}γ and {557}γ, with a pronounced tendency toward {557}γ. Local HP variations, analyzed at the level of individual block boundaries, exhibit deviations of up to ~18.5°, shifting towards {112}γ. This habit plane orientation, previously suggested in theoretical studies but not widely observed experimentally, is linked to block bending and impingement mechanisms. Specifically, spatial interference and growth competition within a single packet and hard impingement between blocks from different packets influence the final HP orientation. These observations refine existing models of lath martensitic transformation by incorporating the effects of localized deformation and interfacial interactions.

The detailed 3D investigation of packet morphology and crystallographic orientation led to the identification of a unique tetrahedral configuration in the spatial arrangement of martensitic packets within PAGs. The formation of this tetrahedral pattern, consistently observed across multiple grains, provides a geometric basis for understanding the spatial organization of packets in 3D. By comparing the experimentally measured packet orientations with theoretical calculations, the study demonstrates that this tetrahedral morphology is strongly linked to the {557}γ habit plane, providing direct experimental validation of prior modeling efforts. This discovery represents a significant advancement in understanding how habit planes influence the large-scale arrangement of martensitic structures in steel alloys.

Beyond the martensitic matrix, this research also explores microstructural heterogeneities such as δ-ferrite, non-metallic inclusions, and casting defects, which critically impact the performance of hydro-turbine steels. Delta-ferrite particles, primarily located at PAG boundaries, exhibit distinct elongated and spherical morphologies, suggesting a formation mechanism

governed by solidification conditions and elemental segregation. Additionally, micropores and non-metallic inclusions were mapped in 3D to assess their spatial distribution and potential effects on fatigue performance and crack initiation.

Furthermore, this study provides a comprehensive analysis of the 3D boundary network, classified based on the Kurdjumov-Sachs (K-S) orientation relationship and its associated intervariant misorientations. Three principal types of block interactions were identified: (i) hard impingement of blocks from distinct packets, (ii) mutual intersection of blocks from different packets, and (iii) interpenetration of sub-blocks/blocks within a single packet. These interactions contribute to the formation of an interlocked martensitic microstructure, resulting in an inhomogeneous boundary network with distinct morphological and crystallographic complexities.

Overall, this research presents new quantitative insights into the 3D morphology, crystallography, and habit plane characteristics of lath martensite in low-carbon stainless steel, establishing a new benchmark for investigating hierarchical microstructures and their influence on material properties. The application of large-volume 3D EBSD proves to be a powerful approach for revealing complex microstructural interactions previously inaccessible through 2D analysis. From an engineering perspective, this study provides valuable 3D microstructural data that can significantly enhance predictive modeling, virtual mechanical testing, and digital twin development for CA6NM and other hydro-turbine steels. The ability to quantify boundary networks, packet orientations, and habit plane distributions facilitates the development of more accurate microstructure-property models, ultimately leading to improved material design, enhanced damage assessment methodologies, and optimized maintenance strategies for hydro-turbine applications.

5.2 Limitations and future work

This study provides novel insights into the three-dimensional (3D) morphology, crystallography, and habit plane characteristics of lath martensite in CA6NM steel. However, several limitations remain, emphasizing the need for further exploration in the following areas:

- **Automated microstructure segmentation**: The misorientation-based segmentation effectively classified the main microstructural features; however, manual segmentation may introduce bias. Implementing machine learning algorithms can enhance segmentation accuracy, enabling more precise and objective hierarchical feature classification.
- **Full-grain analysis and statistical limitations**: Due to the large size of prior austenite grains (PAGs) in CA6NM, full grains could not be reconstructed within the analyzed volume, affecting the statistical study of variant distributions. Future work should use targeted sample preparation and large-volume 3D EBSD to capture entire PAGs.
- **Effect of inclusions and delta ferrite on martensite transformation and 3D morphology**: The 3D analyses revealed that the spatial configuration of blocks and packets appears to be influenced by the presence of delta ferrite particles (not presented in this thesis). However, the extent to which inclusions and ferrite particles affect martensitic transformation, variant selection, and 3D morphology remains unclear. Future work should combine experimental 3D EBSD analysis with computational modeling, such as phase-field simulations, to better understand the role of second-phase particles in martensitic microstructure evolution.
- **Linking 3D characterization with computational models**: Current simulations often simplify grain structures using idealized shapes, such as spheres, cubes, or polyhedral, which fail to capture the true morphology of martensitic structures. Developing a robust

framework for digitizing 3D microstructures will allow for more accurate computational modeling of material behavior.

- **Fatigue crack initiation and short crack growth**: Fatigue life in hydro-turbine steels is dominated by microstructurally short fatigue cracks (SFCs), yet most studies focus on long cracks using linear elastic fracture mechanics. Since SFCs interact strongly with the microstructure and show fluctuating growth rates, future work should focus on characterizing initiation sites and early propagation mechanisms to improve fatigue life predictions.